FAULT IMAGING ENHANCEMENT IN TARANAKI BASIN, NEW ZEALAND AND ROCK PHYSICS AND INVERSION BASED RESERVOIR CHARACTERIZATION IN THE CENTRAL GULF COAST REGION OF TEXAS

by

TIANZE ZHANG

A DISSERTATION

Presented to the Faculty of the Graduate School of the

MISSOURI UNIVERSITY OF SCIENCE AND TECHNOLOGY

In Partial Fulfillment of the Requirements for the Degree

DOCTOR OF PHILOSOPHY

in

GEOLOGY AND GEOPHYSICS

2019

Approved by:

Kelly Hong Liu, Advisor
Stephen Shangxing Gao, Co-Advisor
Jonathan Obrist Farner
Abdulmohsin Imqam
Tingting Li

PUBLICATION DISSERTATION OPTION

This dissertation consists of the following four articles, formatted in the style used by the Missouri University of Science and Technology:

Paper I: Pages 33-44 have been published by SEG Technical Program.

Paper II: Pages 45-58 have been published by SEG Technical Program.

Paper III: Pages 59-71 have been published by SEG Technical Program.

Paper IV: Pages 72-101 are submitted to Interpretation Journal – Society of Exploration Geophysics (SEG).

ABSTRACT

Fault imaging technique and reservoir characterization based on rock physics analysis and pre-stack inversion has been widely used hydrocarbon exploration. For the fault imaging technique, the ant tracking has been widely used in fault interpretation. However, the reliability of the results is highly dependent on appropriately choosing a signal processing method and volume attributes. In our study area, which lies in the southern Taranaki Basin, we applied Graphic Equalizer as the processing tool and the Chaos attribute before running the ant tracking algorithm. Results show that the procedure provides a better result and can map both the major and minor faults more efficiently than the conventional fault interpretation procedure. For the reservoir characterization study, we use the Lower Wilcox strata which has been proven to be a good quality reservoir along the Central Gulf Coast of Texas. While the complexity of its sedimentary environment makes it hard to locate the isolated productive sand accurately. We carry out the rock physics analyses to provide a better understanding of the reservoir properties. Bulk density, P-wave velocity, and elastic moduli are extracted from four wells for analyzing the depth and temperature effects on compaction. A combination of three effective medium models is used for cement volume diagnostics. For the further reservoir characterization, we conduct the pre-stack seismic inversion with seven wells constrained. Our inversion results show a successful delineation of the reservoir using the Vp/Vs and S-Impedance values.

ACKNOWLEDGMENTS

At first, I want to greatly thank my advisor Dr. Liu and co-advisor Dr. Gao. Thanks to all my Ph.D. committee members, Dr. Farner, Dr. Imqam, and Dr. Li for their great help and advice on my research.

I also want to send my gratitude to an alumni for generously providing the comprehensive dataset for the reservoir characterization study, and to the New Zealand Government for providing the dataset for the fault attribute study. I also appreciate Schlumberger for supplying Missouri S&T with licenses for Petrel, Compagnie Générale de Géophysique for offering us licenses for Hampson-Russell software, and Information Handling Services Markit for providing licenses for Kingdom all these years.

I thank all the colleagues in the Geosciences and Geological and Petroleum Engineering Department, especially my workmates and friends in McNutt B16/B40. I feel so grateful to work in such friendly and amicable environment, where everybody shares knowledge without reservation. They motivated and guided me whenever I feel confused.

My great appreciation goes to my parents in China who provide unconditional support to me throughout my fantastic journey in the US.

At last, my special appreciation goes to my lovely wife Yani Lin. I feel so lucky to meet her and marry her. She is the perfect soul mate and partner, and always there for me no matter where and when.

TABLE OF CONTENTS

LIST OF ILLUSTRATIONS

SECTION Page

LIST OF TABLES

SECTION Page

NOMENCLATURE

Symbol	Description
3D	Angle of Attack
AI	Acoustic Impedance
AGC	Automatic Gain Control
RPT	Rock Physics Template
MMBO	Million Barrels of Oil
BCFG	Billion Cube Feet Gas
TIFF	Tagged Image File Format
AVO	Amplitude Versus Offset
hc	Hydrocarbon
Vp	P-wave Velocity
Vs	S-wave Velocity
GR	Gamma Ray
SP	Spontaneous
Rt	Resistivity
SSP	Maximum Spontaneous Value

SECTION

1. INTRODUCTION

Making correct fault interpretation is a crucial step for understanding fault development in a region, as fault movements have great impacts on oil migration and trap formation (Roncaglia and Lucia, 2006). Ant tracking is an innovative technology utilized in fault identification and interpretation. It can capture and track fractures continuously on fracture-sensitive attributes and highlight the faulting areas effectively (Basir et al., 2013). The ant tracking technique includes three steps, including data conditioning, edge detection, and running the ant tracking algorithm (Henery et al., 2011). The typical data conditioning procedure uses Automatic Gain Control (AGC) or Structural Smoothing, which is suitable at displaying large-scaled faults. However, it lacks the ability for reserving small fracture features, as demonstrated in this study.

In our study area, faults are developed in various scales. The traditional processing procedure is insufficient for processing the data with variable fault scales and providing reliable data for ant tracking. To distinguish the discontinuity for weak events, we first use the Graphic Equalizer processing to manually adjust the frequency component of the input signal by following the local geological context. The ant tracking technique is applied on edge enhanced attributes derived from the processed data set. The results show a much detailed ant tracking map, which contains not only the main faults but also minor fractures which are unable to be identified using the typical ant tracking workflow.

Rock physics analysis and seismic inversion play essential roles in understanding sedimentary basins and reservoir characteristics by linking the reservoir properties such as density and porosity with seismic properties (Avseth, 2015). Integration of rock physics and the seismic inversion has been proven a successful method for hydrocarbon exploration and production in geologically complex areas worldwide (Francis et al., 2015; Jensen et al., 2016; Alvarez et al., 2017).

Our study focuses on the sand-rich Lower Wilcox strata in southern Texas, which was deposited during the early Eocene when the frequent sea-level fluctuation stacks the regression sandstone with transgression shales (Fisher and McGowen, 1967; Xue and Galloway, 1993; Galloway et al., 2000; Hargis, 2009; Olariu, 2018). This geologic process develops a considerable amount of structural and stratigraphic traps (Kinsland et al., 2016). The area has been investigated extensively by using wells and 3D seismic data for depicting the depositional system and recognizing the pay sand in relatively large scale (Berg, 1979; Allen and Howell, 1987; Cornish and Parker, 2007; Mackey et al., 2012; Zeng et al., 2016). However, reservoir sands in smaller scales with exploration value have not been discovered. Our study intends to build the relationship between the seismic data and rock properties to delineate the thin and isolated reservoir sand in smaller scales with the aid of 3D pre-stack seismic data.

The quantitative interpretation that uses well logs and pre-stack seismic to quantify the reservoir properties has high resolution and sensitive to fluid (Avseth, 2010). For rock physics analysis, a combination of friable-sand model, contact cement model, and constant cement model from the four exploration well logs are utilized to investigate the physical properties of the Lower Wilcox strata. Key parameters from the models are

utilized to the development of the Rock Physics Template, which further infers the fluid and mineralogical content from a crossplot of Vp/Vs value against acoustic impedance (Odegaard and Avseth, 2003). Then, we conduct the simultaneous inversion to quantify the reservoir and isolate the hydrocarbon area by deriving the impedance for both P-wave and S-wave using pre-stack seismic data (Connolly, 1999; Whitcombe, 2002).

In the study, the transition zone location and the rock physical behavior of the reservoir rock are identified by mapping the compaction trend and building the elastic models. A Vp/Vs ratio map resulted from pre-stack simultaneous inversion is generated, which can be used to isolates the hydrocarbon-bearing sand, and prove its feasibility in the study area. The results can build a solid foundation to carry on further rock physics diagnostics and amplitude versus offset study for better analyses of the reservoir strata.

1.1. AREA OF STUDY

Two areas are contained in this study, Taranaki Basin in New Zealand and Texas Gulf Coast Plain in the United States.

1.1.1. Taranaki Basin. The study area of the Fault Imaging Enhancement project locates in the Taranaki Basin which lies on the west of New Zealand's North Island (Figure 1.1). As the first explored sedimentary bain in western New Zealand, the Taranaki Basin is rich in hydrocarbon resources. The Taranaki Basin is a Cretaceous foreland basin which covers an area over 300,000 Km2 with mostly offshore (Higgs et al., 2010). It was formed in 118 Ma when the basin parted from the Caledonian Basin (King et al., 2010). The Taranaki Thrust Fault and Waimea-Flaxmore faults control the basin on the north-east side and south-east side. Fault systems are highly developed in the Taranaki Basin (Figure 1.1), they act as the migration path that transports the

hydrocarbon from source to the reservoir and often relate with hydrocarbon indicators like gas chimneys (Sykes, 2012).

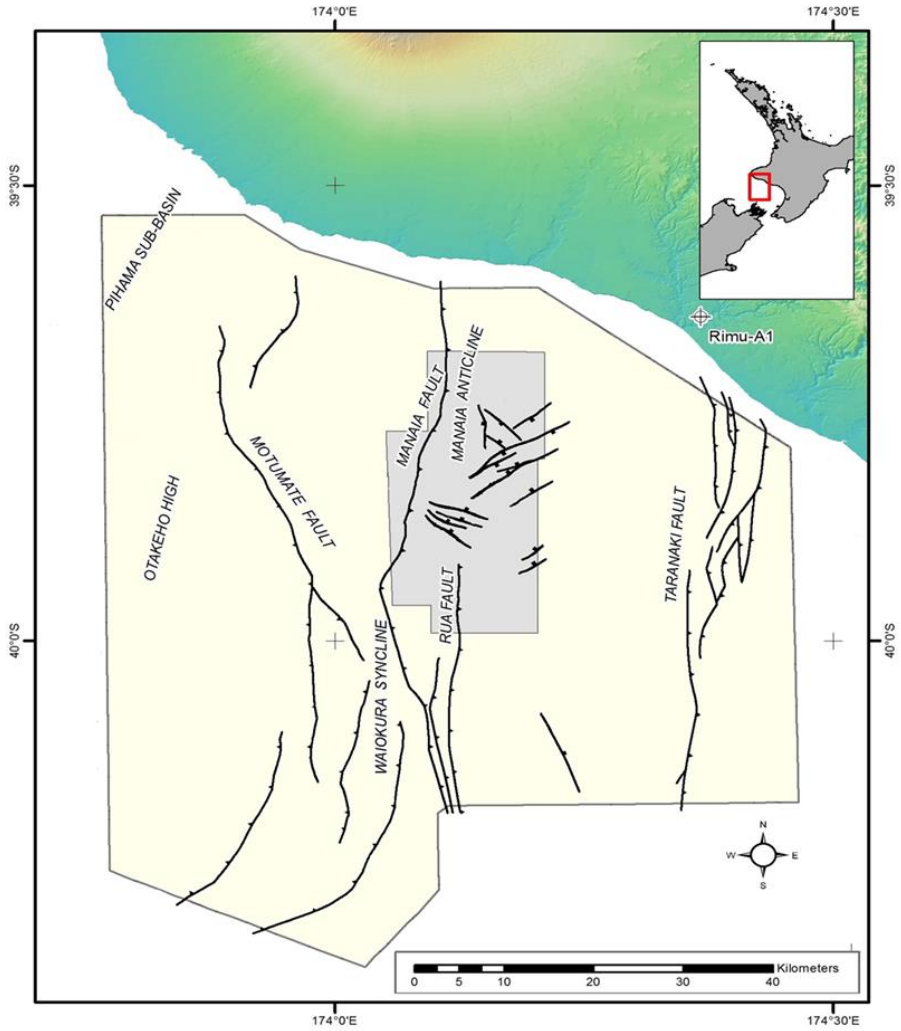

Figure 1.1. Study area location showing the survey area extent and highly developed fault system (Fohrman et al., 2012).

1.1.2. Texas Gulf Coast Plain. The survey area locates at the middle of the Texas Gulf Coastal plain that belongs to the northern Gulf of Mexico basin. The Gulf area was extensively studied and explored due to its high volume of oil and gas accumulation. The

high rate of Tertiary sedimentary source influx and repeatedly transgression and regression result in numerous reservoir and ideal trap. Our study focused on one of the highly productive sequences named Lower Wilcox group. The Lower Wilcox group is overlain by marine or lagoonal muds of middle Wilcox group.

Moreover, it is underlain strata is characterized as marine muds and clays of Midway Group. Fisher & McGowen (1967) associated the hydrocarbon discovery with regional deposition system includes delta trend, strand plain trend, barrier bar trend, shelf trend, shelf-edge trend, and a possible submarine fan trend. In our study area, the incised valley system was generated during regression and fulfilled after transgression plays an essential role in hydrocarbon reservoir accumulation and reservation. Six analog fields and over dozens of prospects had been identified within the 85 square miles 3D survey. Work to date, the survey has offered initial estimated un-risked reserves of 20 MMBO (Million Barrels of Oil) and 100 BCFG (Billion Cube Feet Gas).

1.2. REGIONAL GEOLOGY OF TEXAS GULF COAST PLAIN

The regional geology will be introduced from tectonic setting to regional depositional setting.

1.2.1. Tectonic Setting. During the Middle to Late Jurassic, North America separated from the supercontinent Pangea and caused the initiation of the Gulf of Mexico basin with the force of crustal attenuation (Pindell, 1994). After that, five main episodes were recorded from Late Triassic to Late Cretaceous. In the latest event, the Gulf of Mexico basin took in the sediments from west to north, as the result of the shifting alluvial source (Galloway et al., 2011). Our target, the Wilcox Group, was one of the classic sedimentation deposited during Cenozoic. The whole Wilcox group can be

divided into three subgroups according to the sedimentation rate. The initiation of deposition at the northern Gulf of Mexico started with a sedimentation starvation that lasts over three million years. This phase related to marine shale unit named Midway that discovered across outcrop and subsurface. Then the sedimentation rate suddenly increased after the starvation period and formed the Late Paleocene Lower Wilcox formation. The following deposition from Late Paleocene to Middle Eocene gradually decreased, caused the sedimentation rate in the Middle Wilcox group is only one half of those in Lower Wilcox. At last, the whole Wilcox sedimentation period ended with Upper Wilcox deposode (Galloway et al., 2011).

1.2.2. Regional Depositional Setting. The Paleogene Wilcox in Texas is a thick sequence consists of terrigenous clastic sediments deposits in the marine and terrestrial environment. For the lower Wilcox group, Fisher and McGOWEN (1967) identified seven major depositional systems in Southeastern Texas (Figure 1.2). The dominant system among seven is the Rockdale Delta System, where our study area locates. It comprises of large amount wedges of mud, sand, and lignites. The maximum thickness is up to 5000 feet in the center of system axis, gradually thins with a depositional slope up to the erosional edge. Most of the sediments come from the fluvial system which occurs up structural dip of the Rockdale depositional system. Haq et al. (1987) established a eustatic sea-level curve, suggested that the lower Wilcox group deposited during a gradual sea level rise (Figure 1.3). Incised valley system was initiated when the sea-level lowering, then refilled by estuarine muds in transgression during that period. In northwestern Lavaca county of Texas, Chuber (1979) first identified two valley-filled sequences. The upper one is named Lavaca Channel, and the lower one is Smothers

Channel. Furthermore, Berg (1979) and Chuber (1982) extended the interpretation of both channels and covered most area of northern and northeastern Lavaca County. Devine and Wheeler (1989) refined the results using the time-equivalence technique, and discoverer four significant valleys named C, D, E, and F valley systems (Figure 1.4).

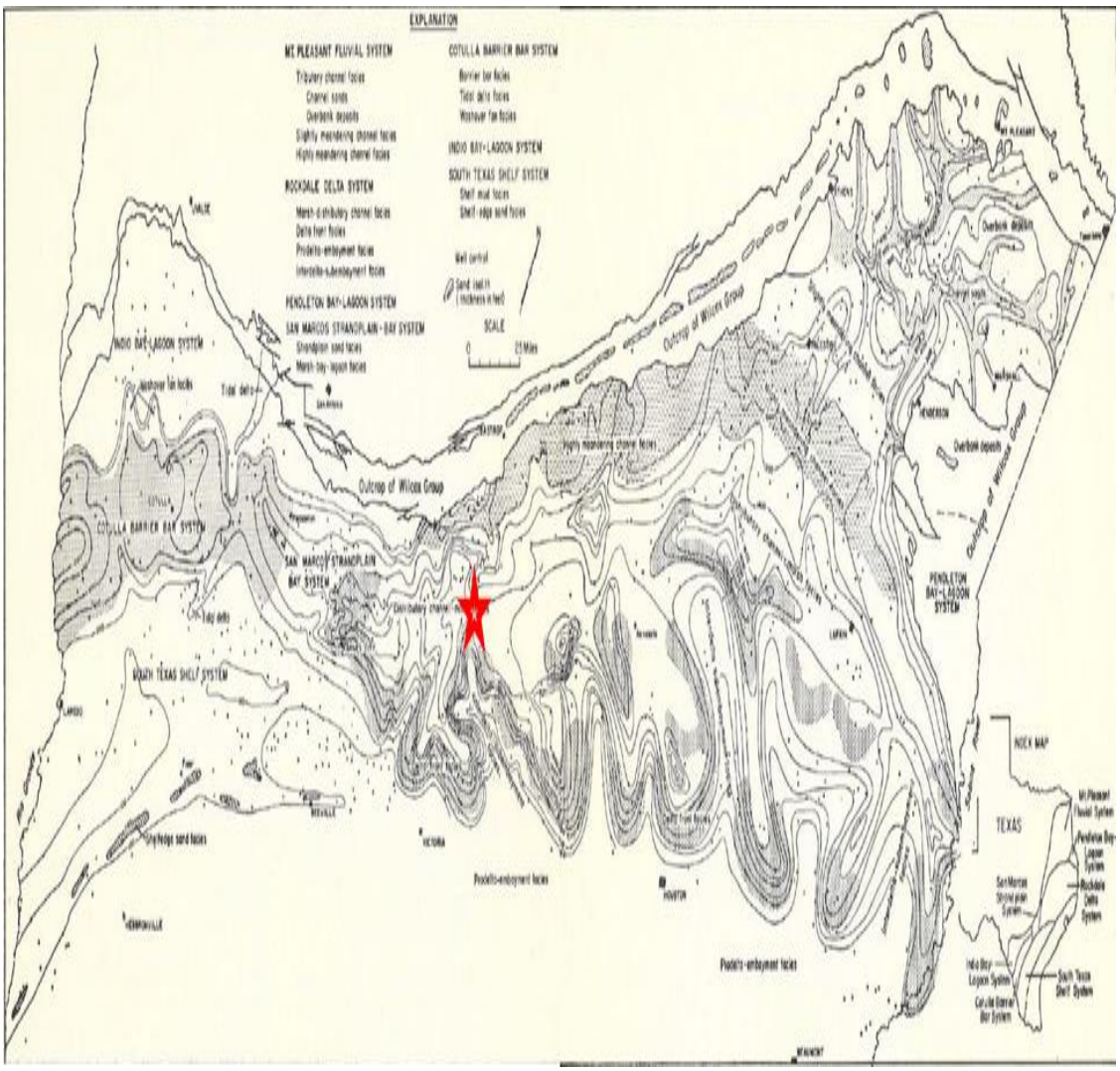

Figure 1.2. Seven major depositional systems in the lower Wilcox group. The red star represents the location of study area. The area is part of the Rockdale Delta system [Fisher & McGowen, 1967].

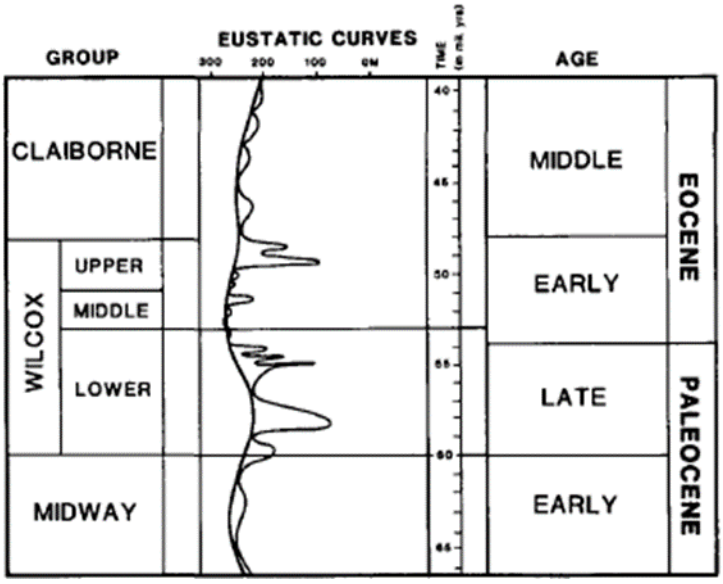

Figure 1.3. The Eustatic sea-level variation combined with stratigraphic sequence [Modified from Haq et al., 1987]. The Late Paleocene-Early Eocene lower Wilcox group was deposited during a gradually sea-level rise, several transgression and regression cycle can be observed during that period.

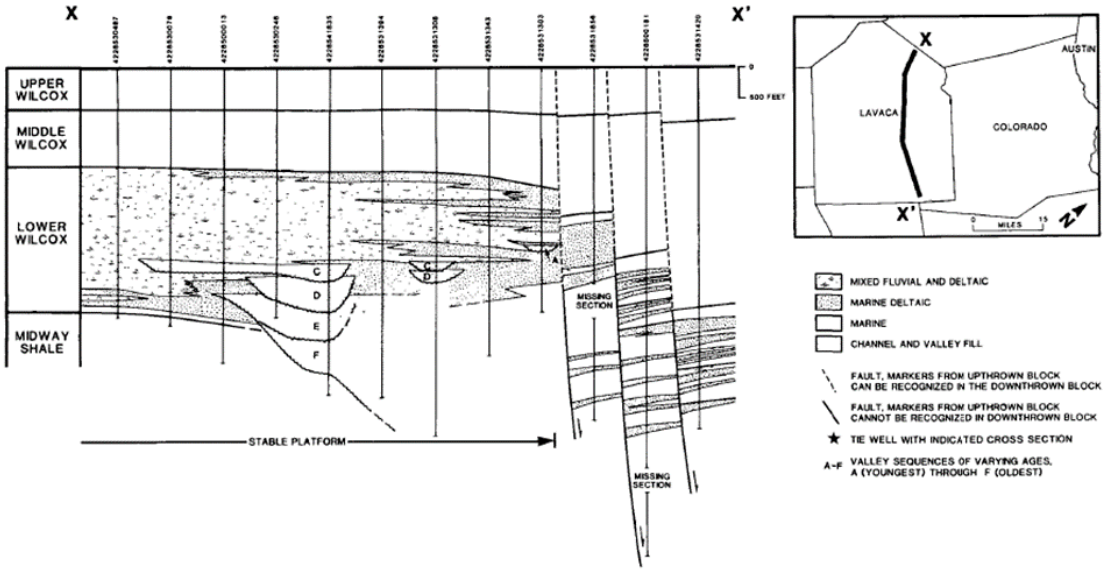

Figure 1.4. The superposition valley system of C, D, E and F. The lower Wilcox formation primarily composed of deltaic and sand-rich fluvial deposits. Some of the tops of the valley-fill sequence has been truncated by younger valley during the sequent regressive cycle. [Modified from Devine & Wheeler, 1987]

1.2.3. Petroleum System. The petroleum system consists all the elements and petroleum geology processes. The most important elements in the petroleum system like reservoir rock and source rock are discussed in detail here. Moreover, the related traps and trapping mechnisms will also be introduced. Abundant sediments sources coming from the upper fluvial system and impermeable shale-filled erosional valley system provide excellent reservoir and seals. Both structural and stratigraphy traps exist in the study area. Within the area of 3D survey, three main trap types are observed in the Lower Wilcox section. Type 1 trap is erosional truncation, where sands are erosionally truncated against the edge of a shale filled submarine canyon or entrenched shoreline valley (Figure 1.5). Type 2 trap is also called erosional remnant (Figure 1.6). The erosional shale filled channels in both NW-SE or N-S dipping direction beneath the lowest most erosional event creates the trapping mechanism.. The third trapping type is called inter-channel erosional remnant (Figure 1.7). The middle erosional event diverged from the lower erosional event, left erosional remnant sand between two shale filled events. The remnant sand was accumulated during the transgressive cycle with lower erosional event act as lowstand deposits. Due to the significant loss of data on the south edge from crossline 1100 to 1212, a seismic example of the type 3 trap cannot be provided.

1.3. DATA SET

Two sets of data are used in this study, one is from Taranaki Basin that provided by the New Zealand Petroleum and Minerals, the other is donated by a generous company.

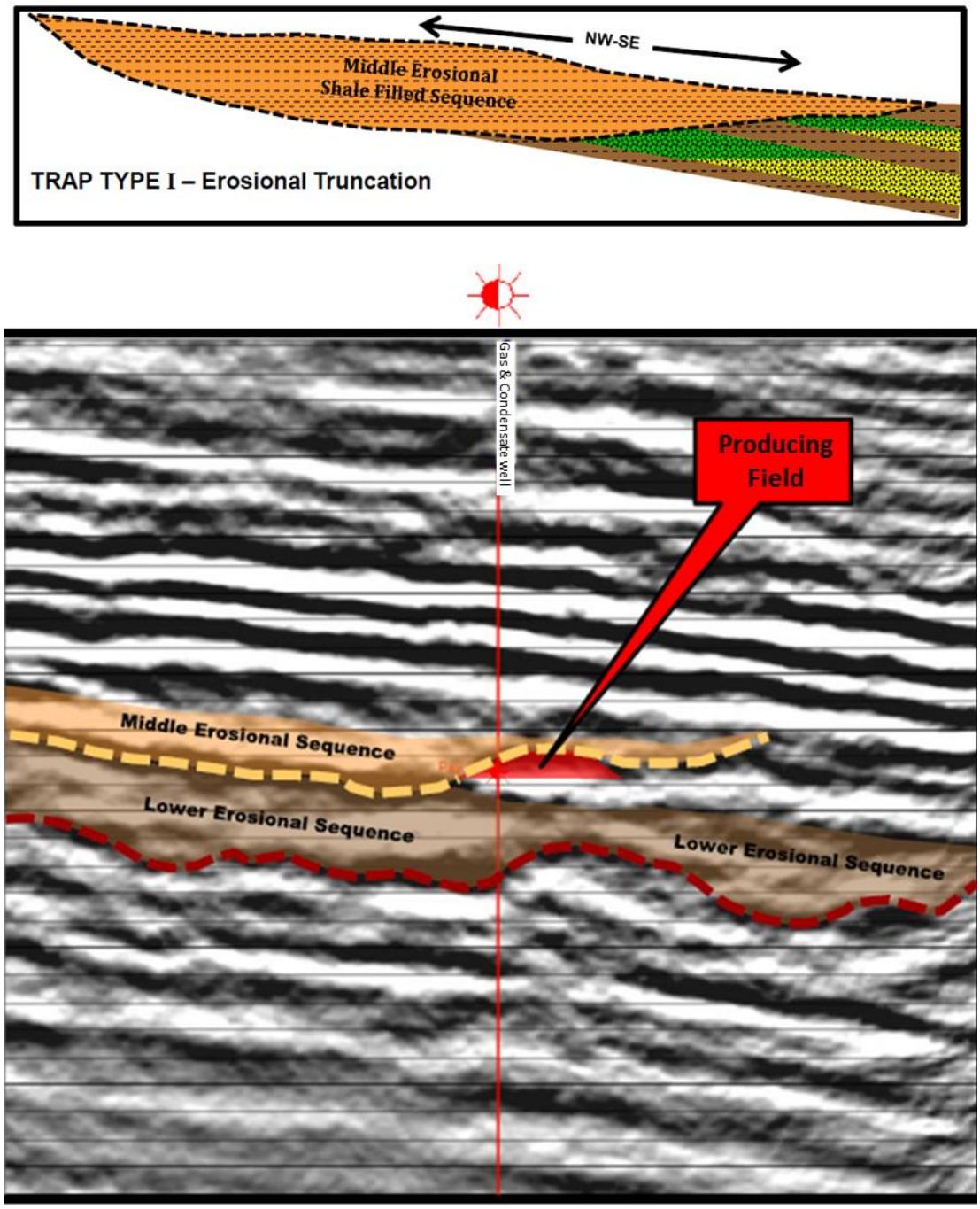

Figure 1.5. (a) The Type 1 trap mechanism. This type of trap was created by meander bends and structural noses forming traps against a shall filled sequence. (b) An example of type 1 trapping mechanism from an inline crossed this acting field. The producing sand is trapped by the middle erosional sequence.

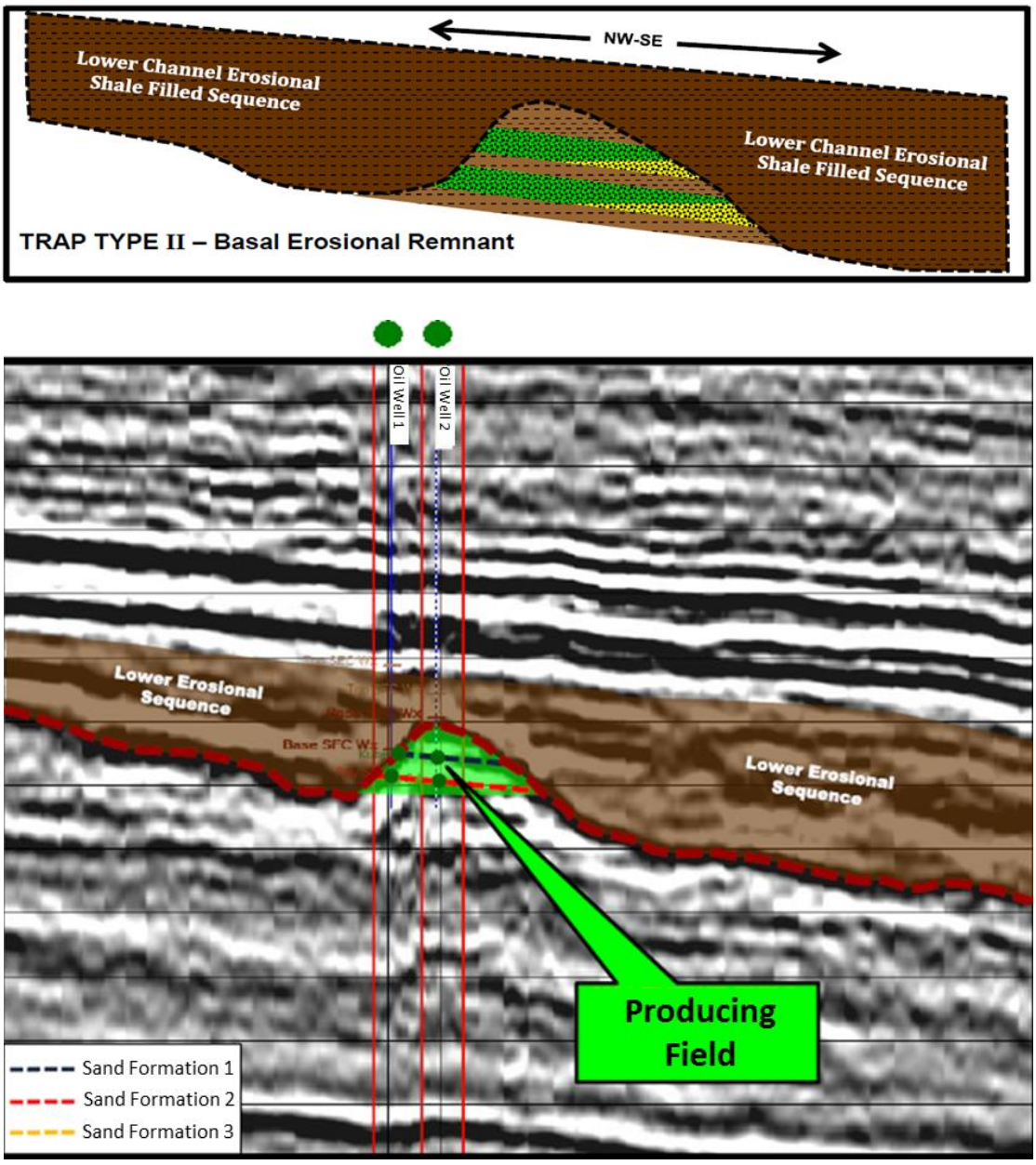

Figure 1.6. (a) The Type 2 trapping mechanism. This type of stratigraphy trap is created by erosional channels in the lower erosional sequence. The remnants were created during regressive cycle that erosional channel eroded into the previous transgressive fluvial-deltaic deposition. (b) An example of type 2 trapping mechanism from an arbitrary line crossed this producing field. The producing sand formation is the remnants and later be covered by shale filled erosional sequence.

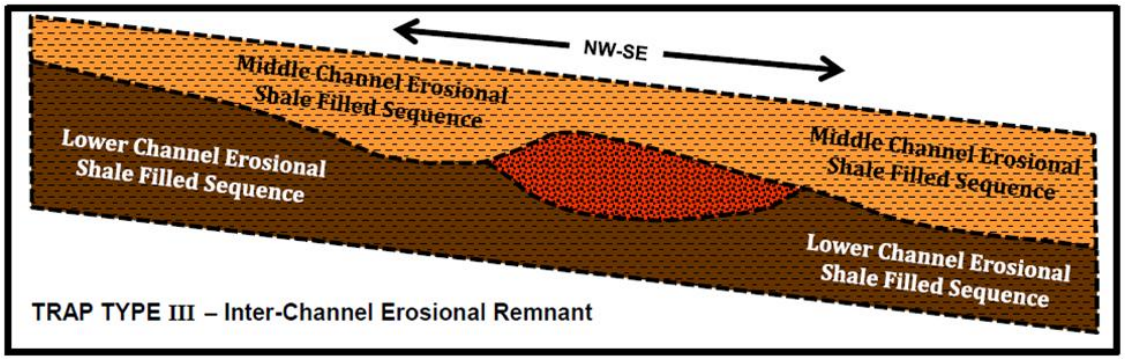

Figure 1.7. The Type 3 Trapping mechanism. The submarine low stand deposits are high quality reservoir that entirely encased in lower and middle shale filled sequence.

1.3.1. Seismic Data in Taranaki Basin. The post-stack Kerry 3D seismic data is one of the 33 surveys conducted in the Taranaki Basin. The New Zealand Petroleum & Minerals (NZP&M) provides all the surveys to the public to seek improvement in the level of petroleum related activity. The Kerry 3D data uses standard SEGY format and coordinates on a standard projection. The survey covers an area of about 442 Km2, including 287 inlines and 735 crosslines (Figure 1.8). It has five seconds of recording length with a sample interval of 0.004 seconds.

The survey uses NZGD49 project coordinate system. Some commercial seismic interpretation software requires the world coordinate of several points to load the data.

Table 1.1 World coordinates for Kerry 3D survey.

	Line	Trace	X Coordinate	Y Coordinate
1	510	58	1703638.0000	5571677.0000
2	510	792	1704135.0000	5608346.0000
3	796	792	1689838.0000	5608539.0000

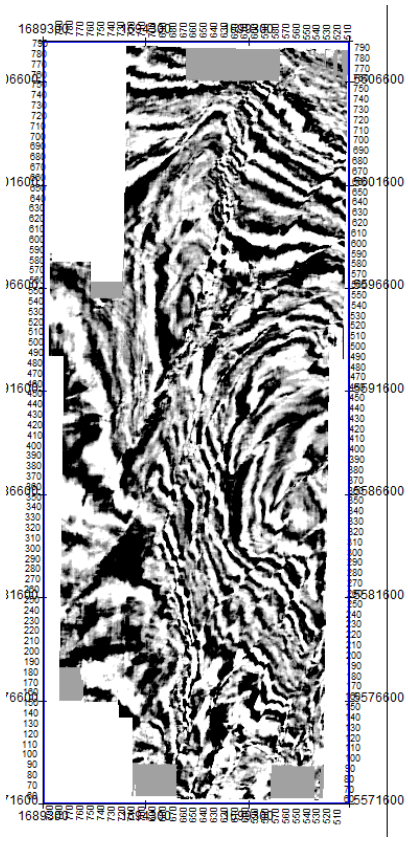

Figure 1.8 An slice example at 0.724s of Kerry 3D.

The coordinates of the survey boundary are included in Table 1.1. Also, the key parameters required for importing the dataset is introduced in Table 1.2.

Table 1.2 Key parameters in the trace header.

	Location
Inline	BYTES 13-16
Crossline	BYTES 17-20
CDP	BYTES 21-24
X Coordinate Metre	BYTES 73-76
Y Coordinate Metre	BYTES 77-80
CDP Elevation	BYTES 81-84

1.3.2. Seismic and Well Data in Central Gulf Coast of Texas. The private-owned data pack was donated by a generous alumni to the Geology, Geophysics, and Petroleum Engineering department. The precise location of the survey remains confidential since the field is still active. The 3D project covers an area of 85 square miles. Both pre- and post-stack data are included. The range for inline is from 154 to 740, for crossline is from 311 to 1212. Total trace length is six seconds. The final pre-stack time migration stack has a sampling rate of 4 milliseconds, and 1501 samples per trace. The wells that used are introduced in Table 1.3.

Table 1.3 Well log data used in this study.

Wells	Status	GR	SP	ILD	RHOB	Vp	Vs
Well-1/T-2	Gas	√	√	√	√	√	
Well-2	Dry	√	√	√	√	√	
Well-3/T-3	Dry	√	√	√	√	√	√
Well-4	Dry	√	√	√	√	√	
#1	Dry	√	√	√			
#2	Dry	√	√	√			
#3	Gas	√	√	√			
#4	Gas	√	√	√			
#5	Gas	√	√	√			
#6	Dry	√	√	√			

1.4. METHODOLOGY

The study applys multiple seismic interpretation methods. Both qualitative and quantitative methods are included.

1.4.1. Fault Detecting Attributes. The procedure to generate the ant-tracking map consists of three steps: 1. Conditioning the seismic using Graphic Equalizer attribute to smooth the seismic trace in a certain time range. 2. Apply Edge Detection attribute such as Variance or Chaos attribute to the volume from the previous step, and generate a volume that showing the discontinuous features of seismic volume. 3. Apply Ant tracking algorithm to deploy ant agents to track the fault like features.

Following are the introduction and instruction on the previous attributes:

- Graphic Equalizer is the attribute that can smooth the seismic traces by applying high, low or band-pass filter to the input volume. An instantaneous frequency attribute should be applied first to analyze the frequency distribution of the seismic section. Then we can enhance or reduce different frequency composition to the interesting area.
- Variance attribute is a type of Edge detection attribute that normally utilized to detect local variance, which is the discontinuities in the horizon amplitude of the input volume.
- Chaos attribute is a type of Edge detection attribute which can detect the degree of the chaotic signal pattern. The lack of organization of the volume normally represents certain geological pattern, such as gas chimney or fault. Hence it is a useful tool that can be used for fault detection. The output of this

attribute is scaled from 0-1, with 0 represents the consistency of signal, and 1 represents the chaos.

- Ant tracking attribute can be used to extract fault features from volume processed by Variance attribute, Chaos attribute, or combined.

1.4.2. Rock Physics. The rock physics knowledge is highly essential in understanding the Amplitude Versus Offset effect. Rock physics deals with physical properties of rock material like P wave velocity, S wave velocity, and density. Lithology information and fluid content can be extracted from such parameters. Analysis and interpreting the parameters can be performed by correctly using the empirical relationship between these parameters.

1.4.2.1. Density modeling. The AVO effect is dependent on properties of velocity and density in a porous reservoir rock. Such rock contains three elements: the matrix material, the porosity, and the fluids that fill the pores. Density effect on a saturated rock can be modeled by the following equation:

$$\rho_{sat} = \rho_m(1 - \emptyset) + \rho_w S_w \emptyset + \rho_{hc}(1 - S_w)\emptyset \quad (1)$$

where:

ρ=density,

$\emptyset$=porosity,

S_w=water saturation,

sat, m, hc, w=saturated, matrix,

hydrocarbon, water subscripts.

1.4.2.2. Relationship between P-wave velocity and S-wave velocity. Castagna et al. (1985) derived an empirical linear relationship between Vp and Vs called the mudrock line:

$$V_p = 1.16V_s + 1360m/s \quad (2)$$

Greenberg and Castagna (1992) extended the previous mudrock line, for a more precise calculation of Vs velocity under different mineralogy circumstances.

Sandstone: $V_s = -0.856\ km/s + 0.804V_p$

Limestone: $V_s = -1.031\ km/s + 1.017V_p - 0.055{V_p}^2$

Dolomite: $V_s = -0.078\ km/s + 0.583V_p$

Shale: $V_s = -0.867\ km/s + 0.770V_p$

Greeenberg and Castagna (1992) also proposed an iterative method to calculate Vs of rock with multiple minerals and a known hydrocarbon component.

- Give an initial estimation of P-wave velocity in brine-filled rock.
- Compute the S-wave velocity from the regression.
- Estimate the moduli and density for each component. Perform Gassmann fluid substitution to compute P-wave velocity for Sw<1 case.
- Modify the brine saturated P-wave velocity based on the error between measured and computed P-wave velocity.
- Iterate until brine-filled Vp agree.

1.4.2.3. Rock physics template (RPT). Odegaard and Avseth (2003) proposed a method to estimate the fluid and mineralogical content of a reservoir, by cross plotting Vp/Vs ratio against acoustic impedance. They calculated the Kdry and mdry as a function of porosity f using Hertz-Mindlin contact theory and lower Hashin-Shtrikman bound.

In Hertz-Mindlin theory, porous rock can be modeled as a packing of identical spheres, the effective bulk and shear moduli equations are:

$$K_{eff} = [\frac{n^2(1-\emptyset_c)^2\mu_m{}^2}{18\pi^2(1-\gamma_m)^2}]^{\frac{1}{3}} \quad (3)$$

$$\mu_{eff} = \frac{5-4\gamma_m}{5(2-\gamma_m)}[\frac{3n^2(1-\emptyset_c)^2\gamma_m{}^2}{2\pi^2(1-\gamma_m)^2}P]^{\frac{1}{3}} \quad (4)$$

where:

P=confining pressure,

μ_m=mineral shear modulus,

n=contacts per grain,

γ_m=mineral Poisson's ratio,

$\emptyset_c$=high porosity end-member.

Then the lower Hashin-Shtrikman bound is used to calculate the bulk and shear moduli of dry rock as a function of porosity f:

$$K_{dry} = [\frac{\emptyset/\emptyset_c}{K_{eff}+(4/3)\mu_{eff}} + \frac{1-\emptyset/\emptyset_c}{K_m+(4/3)\mu_{eff}}]^{-1} - \frac{4}{3}\mu_{eff} \quad (5)$$

$$\mu_{eff} = [\frac{\emptyset/\emptyset_c}{\mu_{eff}+z} + \frac{1-\emptyset/\emptyset_c}{\mu_m+z}]^{-1} - \frac{4}{3}z \quad (6)$$

$$z = \frac{\mu_{eff}}{6}(\frac{9K_{eff}+8\mu_{eff}}{K_{eff}+2\mu_{eff}}) \quad (7)$$

where:

K_m=mineral bulk modulus.

1.4.3. Amplitude Versus Offset. The Amplitude Versus Offset (AVO) section contains AVO modeling, AVO attribute analysis, and AVO classification.

1.4.3.1. AVO modeling. Zoepprtiz equation described the seismic wave energy partitioning at layer boundary. When P-wave encounter the boundary between two layers,

four types of wave will be produced: 1. Reflected P-wave. 2. Reflected S-wave. 3. Transmitted P-wave. 4. Transmitted S-wave. The angle of incident and produced rays are followed the Snell's law:

$$p = \frac{sin\theta_1}{V_{p1}} = \frac{sin\theta_2}{V_{p2}} = \frac{sin\theta_{s1}}{V_{s1}} = \frac{sin\theta_{s2}}{V_{s2}} \tag{8}$$

where P is called the ray parameter, θ and θ_s are the angles of P-wave and S-wave propagation relative to the normal reflector. V_{p1} and V_{p2} represents the P-wave velocity transporting in material 1 and 2, same as V_{s1} and V_{s2}.

Zoeppritz (1919) computed the particle motion amplitude of transmitted and reflected wave using conservation of stress and displacement across the boundary, which gives four equations with four unknowns:

$$\begin{bmatrix} R_P \\ R_D \\ T_P \\ T_S \end{bmatrix} = \begin{bmatrix} -sin\theta_1 & -cos\emptyset_2 & sin\theta_2 & cos\emptyset_2 \\ cos\theta_1 & -sin\emptyset_1 & cos\theta_2 & -sin\emptyset_2 \\ sin2\theta_1 & \frac{V_{P1}}{V_{S1}}cos2\emptyset_1 & \frac{\rho_2 {V_{S2}}^2 V_{P1}}{\rho_1 {V_{S1}}^2 V_{P2}}cos2\emptyset_1 & \frac{\rho_2 V_{S2} V_{P1}}{\rho_1 {V_{S1}}^2}cos2\emptyset_2 \\ -cos2\emptyset_1 & \frac{V_{S1}}{V_{P1}}sin2\emptyset_1 & \frac{\rho_2 V_{P2}}{\rho_1 V_{P1}}cos2\emptyset_2 & \frac{\rho_2 V_{S2}}{\rho_1 V_{P1}}sin2\emptyset_2 \end{bmatrix}^{-1} \begin{bmatrix} sin\theta_1 \\ cos\theta_1 \\ sin2\theta_1 \\ cos2\emptyset_1 \end{bmatrix} \tag{9}$$

where R_P, R_S, T_P, and T_S are the reflected P, reflect S, transmitted P, and the transmitted S-wave coefficients, respectively. V_P and V_S are the P and S-wave velocity. θ and $\emptyset$ are the angle of reflected and transmitted wave. Subscripts 1 and 2 corresponding to upper material 1 and lower material 2.

The P-P reflection coefficient can be calculated:

$$R_{pp} = \frac{[\left(b\frac{cos\theta_1}{V_{p1}} - c\frac{cos\theta_2}{V_{p2}}\right)F - \left(a + d\frac{cos\theta_1 cos\emptyset_2}{V_{p1}V_{s2}}\right)Hp^2]}{D} \tag{10}$$

where

$$a = \rho_2\left(1 - 2{V_{s2}}^2 p^2\right) - \rho_1\left(1 - 2{V_{s1}}^2 p^2\right),$$

$$b = \rho_2\left(1 - 2{V_{s2}}^2 p^2\right) + 2\rho_1 {V_{s1}}^2 p^2,$$

$$c = \rho_1\left(1 - 2{V_{s1}}^2 p^2\right) - 2\rho_2 {V_{s2}}^2 p^2,$$

$$d = 2\left(\rho_2 {V_{s2}}^2 - \rho_1 {V_{s1}}^2\right),$$

$$D = EF + GHp^2,$$

$$E = b\frac{cos\theta_1}{V_{p1}} + c\frac{cos\theta_2}{V_{p2}},$$

$$F = b\frac{cos\emptyset_1}{V_{s1}} + c\frac{cos\emptyset_2}{V_{s2}},$$

$$G = a - d\frac{cos\theta_1}{V_{p1}}\frac{cos\emptyset_2}{V_{s2}},$$

$$H = a - d\frac{cos\theta_2}{V_{p2}}\frac{cos\emptyset_1}{V_{s1}}.$$

The equations give us the exact amplitude as a function of angle. However, it is hard to give an intuitive understanding of the AVO process for angles greater than zero degree. Aki and Richard's (1980) simplified the equation based on the first order linearized analysis. The approximation is:

$$R_p(\theta) = a\frac{\Delta V_p}{2V_p} + b\frac{\Delta V_s}{2V_s} + c\frac{\Delta\rho}{\rho} \tag{11}$$

where:

$$a = 1 + tan^2\theta,$$

$$b = -8(\frac{V_s}{V_p})^2 sin^2\theta,$$

$$c = 1 - 4(\frac{V_s}{V_p})^2 sin^2\theta,$$

$$\rho = \frac{\rho_2+\rho_1}{2}, \Delta\rho = \rho_2 - \rho_1,$$

$$V_p = \frac{V_{p2}+V_{p1}}{2}, \Delta V_p = V_{p2} - V_{p1},$$

$$V_s = \frac{V_{s2}+V_{s1}}{2}, \Delta V_s = V_{s2} - V_{s1},$$

1.4.3.2. AVO attribute analysis. Since the seismic trace reflects changes in impedance more than changes in velocity or density independently, the original form of Aki-Richard's equation is not enough to extract attribute information. Wiggins et al. (1983) reformulated an equivalent from the Aki-Richard's equation. The original equation is separated into three reflection terms, each term consists a weight multiplied by an elastic parameter. The equation is:

$$R_p(\theta) = A + Bsin^2\theta + Ctan^2\theta sin^2\theta \tag{12}$$

where:

$$A = R_p(0°) = \frac{1}{2}[\frac{\Delta V_p}{V_p} + \frac{\Delta \rho}{\rho}],$$

$$B = \frac{1}{2}\frac{\Delta V_p}{V_p} - 4[\frac{V_s}{V_s}]^2\frac{\Delta V_s}{V_s} - 2[\frac{V_s}{V_s}]^2\frac{\Delta \rho}{\rho},$$

$$C = \frac{1}{2}\frac{\Delta V_p}{V_p}.$$

A is called the intercept, B is the gradient, C is the curvature.

The C term is not significant when the small angle is considered. Hence, the equation can be further normalized to a two-term Aki-Richards equation, when the angle is smaller than 40 degree. The following equation is:

$$R_p(\theta) = A + Bsin^2\theta \tag{13}$$

where A and B are same to the weights in the original equation.

For generating attributes of intercept and gradient, the first step is to convert the original seismic data from offset to angle. Then fit a regression line to the amplitude picks as a function of the sin&2.

In the first step of converting, we use Ray Parameter approximation method to transfer offset to angle. The equation for this method is:

$$sin\theta = \frac{XV_{INT}}{tV_{RMS}{}^2} \tag{14}$$

where V_{INT} is the interval velocity, and t is the total traveltime.

There are several favorite AVO attributes that will be used for AVO analysis:

- AVO product: A*B
- Scaled Poisson's Ratio Change: A+B
- Shear Reflectivity: A-B
- Fluid factor

1.4.3.3. AVO classification. Rutherford and Williams (1989) classified the gas sand into three different types by using cross-plot of the reflection coefficient and offset. The classification scheme is modified later by Ross and Kinman (1995) and Castagna (1997) :

- Class 1: high-impedance sands,
- Class 2: near-zero impedance contrast sands,
- Class 2p: Same as Class 2, but change in polarity,
- Class 3: low-impedance sands, AVO increasing,
- Class 4: low-impedance sands, AVO decreasing.

Class 1: high-impedance sands

- Higher impedance than the adjacent medium.
- Shale-sand interface has significant and positive R0.
- Often found on-shore.

- Mature sands that endured moderate to high compaction.
- R0 decreases with offset.

The reflection coefficient for Class 1 sand is positive at zero-offset. The rate of the magnitude changing with offset is considerably larger than Class 2 and Class 3. Initially, the reflection coefficient decrease with the increasing offset and the polarity would change if sufficient offset range is provided.

Class 2 and 2p: near-zero impedance contrast sands.

- Nearly the same impedance with surrounding material.
- Moderately compacted and consolidated.
- Polarity may change if R0 is positive.
- Correlate with environments of offshore and onshore

Class 2 sand is hard to detect when the offset is small and its reflectivity is close to zero. While the reflection will appear at larger offset since the reflection amplitude is more significant than noise. The gradient of Class 2 sand is smaller than Class 1. The polarity can change when the reflection coefficient is positive, but it can be hardly detected, as it happens at near offset where high noise level exists.

Class 3 and 4: low-impedance sands

- Low impedance than encasing material.
- Undercompacted and unconsolidated.
- Correlate with the marine environment.
- No polarity change at all offsets.
- The AVO increases for Class 3.
- The AVO decreases for Class 4.

We cannot observe polarity change in Class 3 and 4 type of sand because the normal incidence reflection coefficient is already negative. Usually, the Class 3 sand has 'bright spot' on stack seismic data, and all offsets reflectivities are considerably large.

1.4.4. Log Estimation. Several essential logs are missing, for example the P-wave velocity and density. All are carefully estimated and quality controlled.

1.4.4.1. Vp-Resistivity relation. For sandstone formation with a handful of clay content, Faust's equation can describe the relationship between the elastic property and the electrical property with 100% water saturation (Hacikoylu et al., 2006). The original form for the Faust's equation is

$$V_P = a * (d * Rt)^{1/6}$$

where the constant a is 1948, d is depth in ft, Rt is the formation resistivity in ohm-ft, Vp is the P-wave velocity in ft/s.

Since the equation is emperically derived, the estimation would have error in the real field. Adcock (1993) derived a time average equation which can draws a better estimation in sand-shale situation. The equation is given by

$$\Delta T = \Delta T_F f_R + [\Delta T_{sh} f_{sh} + \Delta T_{sd}(1 - f_{sh})](1 - f_R), \quad (1)$$

where ΔTsh and ΔTsd are the sonic travel time for shale and sand, which are 90 and 53 μs/ft, respectively. ΔTF is the fluid travel time that varies in different depth range. The value is 189 μs/ft for Upper Wilcox Formation and 165 μs/ft for Lower Wilcox formation.

The fractional shale volume, fsh, can be calculated by the gamma ray log, the equation is given by

$$f_{sh} = \frac{0.5 * GR_{index}}{1.5 - GR_{index}}$$

where the GR_{index} is given by

$$GR_{index} = \frac{GR - GR_{ss}}{GR_{sh} - GR_{ss}}$$

The GRss is the sandstone gamma ray value, the GRsh is the shale gamma ray value.

The fractional porosity, fR, was calculated by Archie's equation assuming 100 percent water saturation, given by

$$f_R = (aRw/{S_w}^n Rt)^{1/m}, \qquad (2)$$

where the constants a, n, and mare 0.81, 2, and 1, respectively.

For the estimation of the formation water resistivity Rw, one can assume the 100% saline water has a constant resistivity of 0.045 Ω-m, or use the following steps for the calculation when have mud filtrate resistivity in the log head:

- Make correction to the resistivity of mud filtrate (Rmf) and drillling mud (Rm) to the formation temperature after determine the temperature of formation under certain depth.
- Determine the SSP which represents the maximum SP value of a formation that has a thickness larger than 50 ft.
- Use the SSP to determine the Rmf/Rwe ratio. The Equivalent resistivity (Rwe) can be calculated by dividing Rmf by the Rmf/Rwe ratio.
- Use the calcualted Rwe to correct Rw under the formation temperature.

The equation for calculating the formation temperature at certain depth is given by

$$T_f = \left(\frac{BHT - AMST}{TD} * FD\right) + AMST$$

where AMST is the annual mean surface temperature, BHT is the bottom hole temperature, TD is the total depth of the borehole, FD is the formation depth, Tf is the formation temperature.

The equation for correcting the Rmf from surface temperature to formation temperature is given by

$$R_{mf} = \frac{R_{mfsurf} * (T_{surf} + 6.77)}{T_f + 6.77}$$

where Rmf is the Rmf at formation temperature, Rmfsur is the Rmf at surface temperature, Tsurf is the Rmf at measured temperature.

To deriviate the equivalent formation water resistivity Rwe from SP and Rmf, the equation is given by

$$R_{we} = R_{mf} * 10^{SP/(61+0.133*BHT)}$$

where Rwe is the equivalent formation water resistivity, SP is the SP value for the chosen formation, BHT is the bottom hole temperature.

The equation to correct the Rw from Rwe is given by

$$R_w = \frac{R_{we} + 0.131 * 10^{\left(\frac{1}{\log(BHT/19.9)}\right)^{-2}}}{R_{we} * -0.5 + 10^{\frac{0.0426}{\log(BHT/50.8)}}}$$

1.4.4.2. Vp-Density relation. Density log is one of the most crucial part for seismic interpretation. Applications like log correlation and seismic inversion, require

density log to build reflection coefficient and impedance log. However, there are many circumstances where density log is absent, hence it needs to be estimated through other logs, normally from P-wave velocity. Gardener et al. (1974) presented a generalized equation for many rock types to describe the relation between P-wave velocity and density, the equaiton is given by

$$\rho = a * Vp^{b}$$

where a and b are 1.743 and 0.25, respectively. P is the density in g/c3, Vp is the P-wave velocity in km/s.

When multiple rock types present and accurate result is needed, a more specific equation for different litholgy situation is presented by Castagna et al. (1993). The equation is given by

$$\rho_b = aV_p{}^2 + bV_p + c$$

in which the coefficients a, b, and c are -0.0261, 0.373, 1.458 for shale, and -0.0115, 0.261, 1.515 for sandstone (Gardner et al., 1974). The units are km/s for velocity and g/cm3 for density.

1.4.5. Seismic Inversion. The simultaneous pre-stack inversion was conducted using the method proposed by Hampson et al. (2005), which was based on the Aki-Richards equation and the linear relation between the logarithm of P-impedance, S-impedance, and density. The pre-stack data were transferred into angle domain ranging from 0-45o. The angle dependent wavelets were extracted from the volume. An initial model of P-impedance, S-impedance, and density was built using both wells for the inversion iteration process. The inversion results were used to calculate various elastic parameters to identify the hydrocarbon anomalies.

1.4.5.1. Post-stack inversion. The seismic traces is the convolution of the reflectivities of underlying formations and a bandlimited seismic wavelet, the equation is shown by

$$S = W * R$$

where W is the band limited wavelet, and R is the reflectivity. The reflectivity is calculated by the acoustic impedance of each individual layer, which is shown by

$$R_n = \frac{Z_{n+1} - Z_n}{Z_{n+1} + Z_n}$$

where Rn is the reflectivity of the nth layer, Zn+1 is the acoustic impedance of the underlying layer, Zn is the acoustic impedance of the nth layer. By assuming a given seismic signal, it is possible to recover the P-impedance by inverting this equation, which is shown by

$$Z_{n+1} = Z_n[\frac{1 + R_n}{1 - R_n}]$$

Simply applying the equation to a seismic trace, we can invert the seismic reflection data to P-impedance. However, the bandlimited wavelet in the convolution model influnces the seismic trace, it wipe out the low frequency part in the seismic. Russell and Hampson (1991) solved the problem by using a low frequency model of P-impedance that extracted from well logs as an initial model to start the inversion process, then adjusting the model untill the seismic trace matches the synthetic traces.

1.4.5.2. Pre-stack simultaneous inversion. The traditional seismic processing workflow consists of stacking procedure which transform a group of CMP gathers into a stacked section. The original thought behind the stacking process is to increase the signal to noise ratio by cancelling the noise, without acknowledging the amplitude variations on

the gatheres where hydrocarbon exists. After the geophysicists make more observations on the AVO effect and classified the event, the pre-stack inversion has been paid more attention ever since for various purposes such as facies classification or direct hydrocarbon recognition.

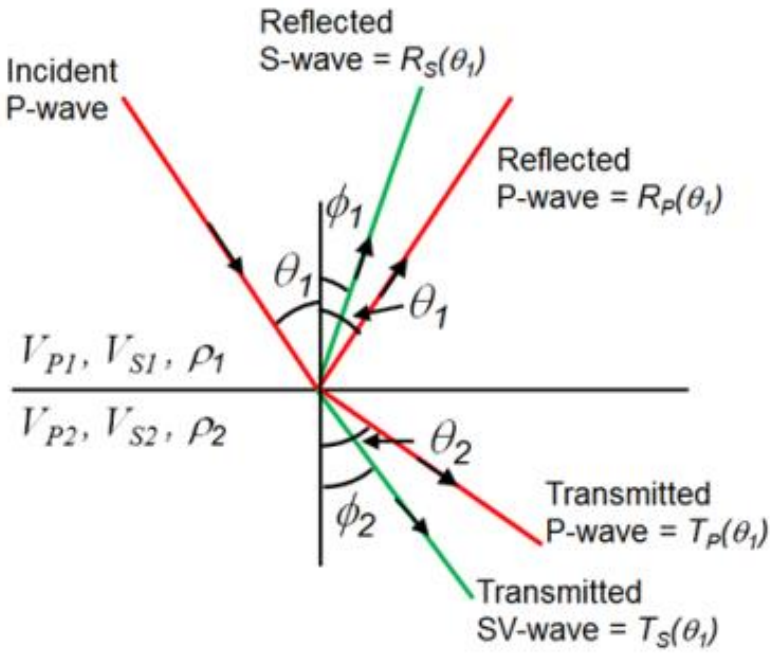

Figure 1.9. The wave conversion model of Zoeppritz equation.

The indicent P-wave can transmit into reflected P-wave and S-wave when hitting a layer. We use the Zoeppritz equation to calculate the amplitudes of reflected and transmitted waves, which is shown by

$$\begin{bmatrix} R_P(\theta_1) \\ R_S(\theta_1) \\ T_P(\theta_1) \\ T_S(\theta_1) \end{bmatrix} = \begin{bmatrix} -sin\theta_1 & -cos\phi_1 & sin\theta_2 & cos\phi_2 \\ cos\theta_1 & -sin\phi_1 & cos\theta_2 & -sin\phi_2 \\ sin2\theta_1 & \frac{V_{P1}}{V_{S1}}cos2\phi_1 & \frac{\rho_2 {V_{S2}}^2 V_{P1}}{\rho_1 {V_{S1}}^2 V_{P2}}sin2\theta_2 & \frac{\rho_2 V_{S2} V_{P1}}{\rho_1 {V_{S1}}^2}cos2\phi_2 \\ -cos2\phi_1 & \frac{V_{S1}}{V_{P1}}sin2\phi_1 & \frac{\rho_2 V_{P2}}{\rho_1 V_{P1}}cos2\phi_2 & -\frac{\rho_2 V_{S2}}{\rho_1 V_{P1}}sin2\phi_2 \end{bmatrix}^{-1} \begin{bmatrix} sin\theta_1 \\ cos\theta_1 \\ sin2\theta_1 \\ cos2\phi_1 \end{bmatrix}$$

Fatti et al. (1994) simplified the equation to make it more intuitive, the equation is shown by:

$$R_{PP}(\theta) = c_1 R_P + c_2 R_S + c_3 R_D$$

where

$$c_1 = 1 + tan^2\theta$$

$$c_2 = -8\gamma^2 tan^2\theta$$

$$c_3 = -0.5tan^2\theta + 2\gamma^2 sin^2\theta$$

$$\gamma = \frac{V_S}{V_P}$$

and R_P, R_S, R_D represents the reflectivities of P-wave, S-wave and density, respectively. The equation's inherent problem is that the inversion results of R_S and Density are unstable when incident angle is small.

The seismic traces can be considered as the convolution of bandlimited wavelet and reflectivity, which can be written as

$$T = \left(\frac{1}{2}\right) WDL_P$$

where $L_{Pn}=\ln(Z_{Pn})=\ln Z_{n+1}-\ln Z_n$.

We can extend the trace T to a certain angle trace T(ϕ) in this equation by adding the Fatti's equation into it, then the trace at a given angle is expressed as

$$T(\theta) = \left(\frac{1}{2}\right) c_1 W(\theta) DL_P + \left(\frac{1}{2}\right) c_2 W(\theta) DL_S + c_3 W(\theta) DL_D$$

where $L_S=\ln(Z_S)$ and $L_D=\ln(\rho)$, W(θ) is the wavelet of a giving angle. There is a linear relation between L_P and L_S, and L_P and L_D (Figure ?), which is

$$\ln(Z_S) = kln(Z_P) + k_c + \Delta L_S$$

$$\ln(Z_D) = mln(Z_P) + m_c + \Delta L_D$$

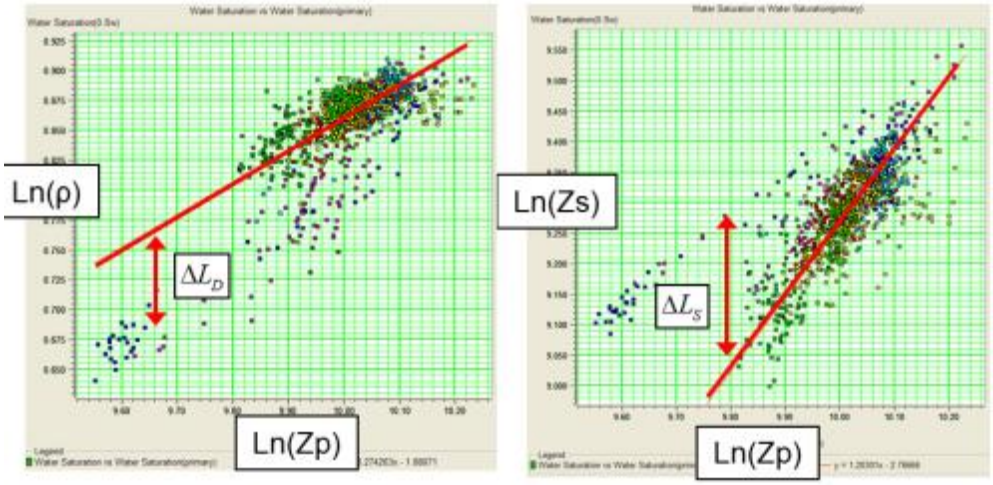

Figure 1.10 The linear relationship between L_P and L_S, and L_P and L_D.

Then the Fatti's equation can transfrom into a new form, which is shown by

$$T(\theta) = a_1 W(\theta) DL_P + a_2 W(\theta) DL_S + c_3 W(\theta) DL_D$$

where

$$a_1 = \left(\frac{1}{2}\right) c_1 + \left(\frac{1}{2}\right) k c_2 + m c_3$$

$$a_2 = (1/2) c_2$$

and D is the derivative operator.

The new equation has better performance than the original Fatti's equation because the independent variables make the system more stable.

1.4.5.3. Pre-stack simultaneous seismic inversion procedure. The simultaneous inversion procedure consists of three parts: 1. Seismic conditioning. 2. Wavelet and model prepration. 3. Inversion analysis and application. The additional steps in our study including well log estimation and conditioning (Figure 1.11).

Seismic conditioning is a procedure that using muting to remove the far offset noise to a range of pre-stack gathers, and using angle gather process to transform a group of your gathers from the offset domain into the incident angle domain.

The geological model comprises initial guess of P-impedance, S-impedance and density for the inversion process. Building such model requires the computation of elastic parameters in well logs, and the guidance of interpretted horizons.

The inversion analysis performs the inversion on well locations in the studying area, it can test a range of inversion parameters efficiently so the optimal parameters can be chosen before applying to the whole volume.

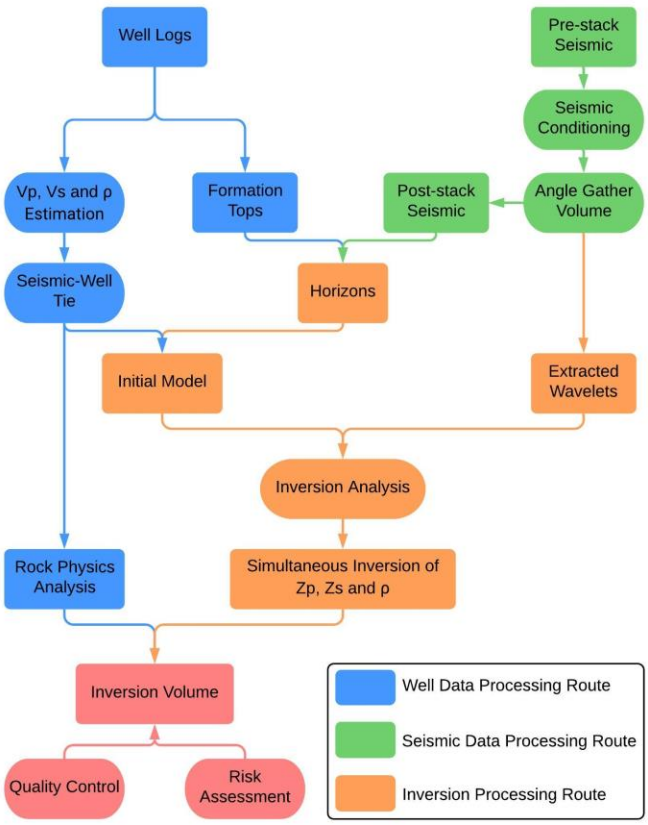

Figure 1.11. The seismic inversion procedure for our study.

PAPER

I. FAULT VISUALIZATION ENHANCEMENT USING ANT TRACKING TECHNIQUE AND ITS APPLICATION IN THE TARANAKI BASIN, NEW ZEALAND

Tianze Zhang*, Yani Lin, Kelly H. Liu, Aamer Alhakeem, and Stephen S. Gao,

Missouri University of Science and Technology

ABSTRACT

The ant tracking technique has been widely used in fault interpretation. However, the reliability of the results is highly dependent on appropriately choosing signal processing method and volume attributes. In our study area, which lies in the southern Taranaki Basin, we applied Graphic Equalizer as the processing tool and the Chaos attribute before running the ant tracking algorithm. Results show that the procedure has better quality and can map both the major and minor faults more efficiently than the conventional fault interpretation procedure.

1. INTRODUCTION

Making correct fault interpretation is a crucial step for understanding fault development in a region, as fault movements have great impacts on oil migration and trap formation (Roncaglia and Lucia, 2006). Ant tracking is an innovative technique utilized in fault identification and interpretation. It can capture and track fractures continuously

on fracture-sensitive attributes, and highlight the faulting areas effectively (Basir et al., 2013). The ant tracking technique includes three steps, including data conditioning, edge detection, and running the ant tracking algorithm (Henery et al., 2011). The typical data conditioning procedure uses Automatic Gain Control (AGC) or Structural Smoothing, which is suitable at displaying large-scaled faults. However, it lacks the ability for reserving small fracture features, as demonstrated in this study.

In our study area, faults are developed in various scales. The traditional processing procedure is insufficient for processing the data with variable fault scales and providing reliable data for ant tracking. In order to distinguish the discontinuity for weak events, we first use the Graphic Equalizer processing to manually adjust the frequency component of input signal by following the local geological context. The ant tracking technique is applied on edge enhanced attributes which derived from processed data set. The results show a much detailed ant tracking map, which not only contains the main faults, but also minor fractures which are unable to be identified using the typical ant tracking workflow.

2. DATA AND METHOD

The study area is located in the Kupe area in the south of the Taranaki Basin (Fohrmann et al., 2012). Faults are highly developed in the study area. The Manaia Fault is a significant reverse fault trending from north to south and cutting through the west boundary of the study area. The fault was a normal fault originally, but reactivated and formed the Manaia Anticline after the late Eocene (Stagpoole and Nicol, 2008). The Rua

Fault, which was once part of the Manaia Fault, is located in the south of the study area. Other regional faults in the area trend northeast-southwest (Figure 1).

The poststack data set used in the study is the Kerry 3D, which is a marine seismic survey conducted in 1996. The area is located close to the south of the coastline, and covers 407 km^2. The data set consists of 287 inlines and 735 crosslines with 50 meters line spacing.

The Graphic Equalizer allows us to enhance or reduce different frequency composition in order to adjust seismic resolution in various time ranges. As the first step in the workflow, the Instantaneous Frequency attribute is derived to observe the frequency distribution (Figure 2). The attribute indicates that the shallow section is sensitive to frequencies between 40 and 80 Hz, and the deeper part is responsive to frequencies between 10 and 40 Hz. By carefully reducing the amplitude in the frequency band between 40 and 80 Hz, the structure in the upper part is highly smoothed. As the result, irrelevant details are removed and edge information is more detectable.

The Variance attribute is normally utilized to detect the edges, and the Chaos attribute can examine the degree of organization and mark the area where organization is lacking (Randen et al., 2000). For conventional edge enhancement procedures, Variance and Chaos attributes are combined to enhance the discontinuity. However, in this study, we found that the attribute combination strongly decreases the fracture details and distorts the ant tracking results. Hence only the Chaos attribute is used in this study.

Ant tracking is an innovative technique in the modern interpretation field. The principle of ant tracking is to set “ant agents” around the data volume, and let them track the possible discontinuities of seismic reflectors within the deviation preset. Firstly, we

put one ant agent per 5 voxels to fully cover the seismic volume. Then we set the parameters of track deviation and illegal steps to ensure all possible fractions were traced. Since most of the faults in the study area are high-angled faults, tracking paths with angle smaller than 30° were rejected.

3. RESULTS AND DISCUSSIONS

Figure 4 shows the comparison of the processed data using the Graphic Equalizer with different strengths of the frequency bands. By reducing the amplitude in frequency band ranging from 40 to 80 Hz, the structures are smoothed and the edges are highly detectable. The results show that the frequency band we chose has significantly improved the capability for identifying seismic discontinuity without jeopardizing any detailed information.

We compared the resulting ant tracking maps using different data processing workflows and various attributes (Figure 4). Running the ant tracking attribute on the combined Variance and Chaos shows a result that lack of information, especially when the attribute is derived upon the data set processed by AGC and structure smoothing. In addition, the ant tracking map using the Variance attribute calculated from the frequency modified data set contains too much noise, especially in the deeper part of the area (Figure 4c).

The best result comes from the map using the Chaos attribute (Figure 4d). For the shallow part of the study area, the map contains much comprehensive detail of fracture

components, which are invisible in other maps. For the deeper part, the disordered area is replaced by horizontally linearized tracks representing the strata.

The ant tracking map also shows promising results compared with previous study (Sykes, 2012). Most faults are fully presented in our map, and minor faults that were not covered in the previous interpretation are identified as well (Figure 5). Time slices of 600 ms and 1368 ms are extracted from the data volume that displayed with ant tracking results (Figure 6), which clearly suggest that the ant tracking results match with the geological structure well in both shallow and deep layers.

4. CONCLUSIONS

Our study using a complex 3D marine seismic data set indicates that the ant tracking technique is an outstanding tool in fault identification and interpretation. However, the reliability of the results is based on proper selection of signal processing methods and volume attributes. In the typical processing procedure, Automatic Gain Control and Structural Smoothing are sufficient to process the data and increase the signal to noise ratio. In our study area, the complex geological structure and various data quality require a more comprehensive signal processing technique to provide accurate fracture information. Graphic Equalizer by adjusting amplitudes of different frequencies appropriately can help us to achieve this goal. Our results show that in such geological conditions, the Chaos attribute performs well for edge detection, leading to clearer and detailed results than combining the Variance and Chaos attributes or the Variance attribute alone.

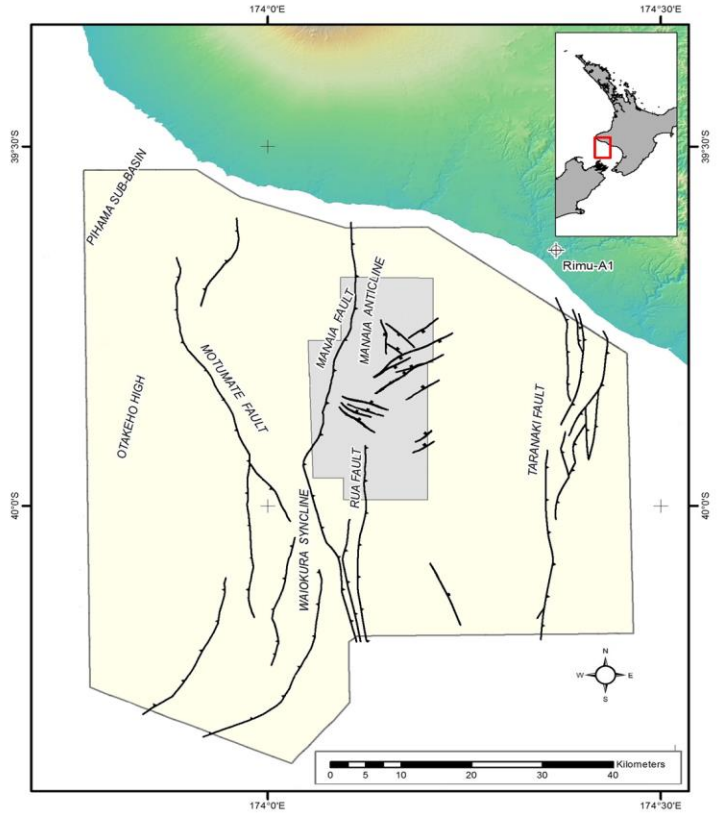

Figure 1. Main structure feature of the study area. The Kerry 3D is marked by the grey polygon. The Kupe area is outlined by the cannary polygon (Fohrman et al., 2012).

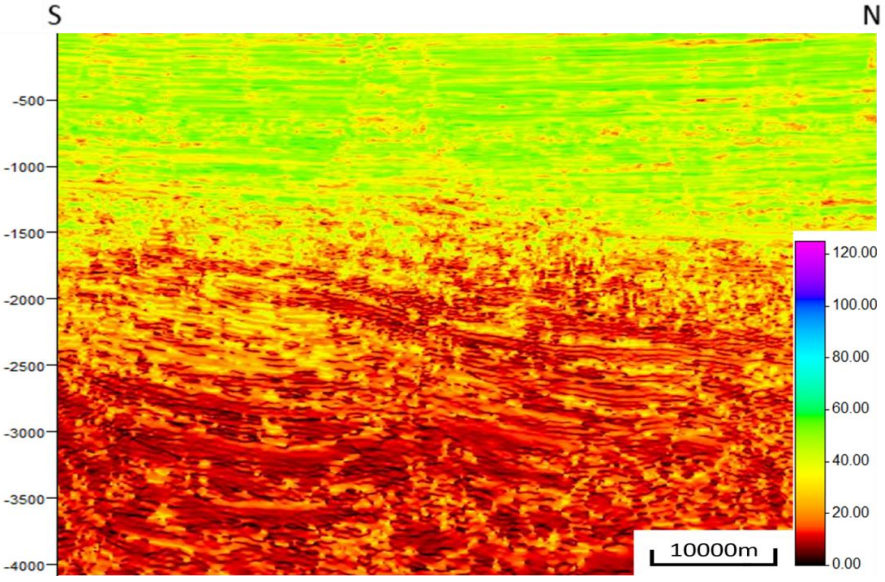

Figure 2. Instantaneous frequency attibute of inline 585.

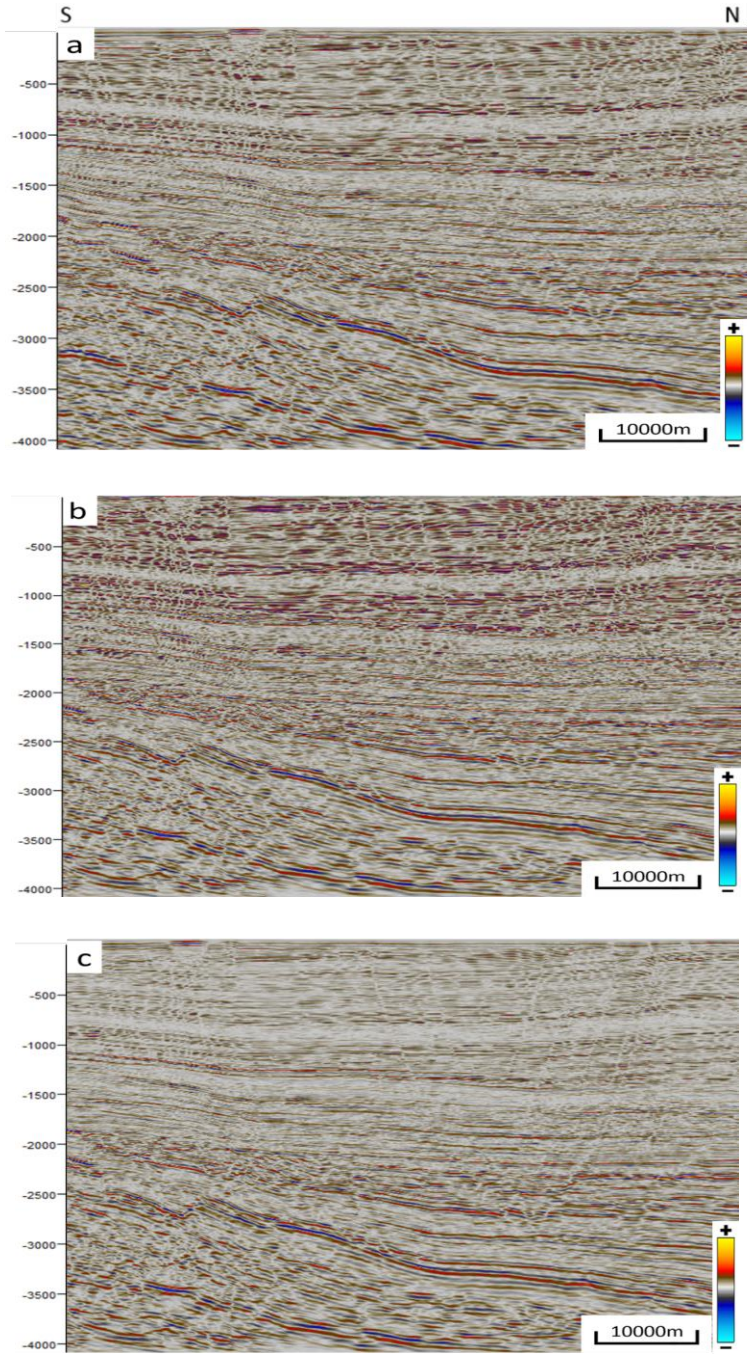

Figure 3. Comparison of the original and processed data of inline 585. (a) Original seismic section. (b) Resulting section after increasing the amplitude of frequency band between 40 and 80 Hz. (c) Resulting section after decreasing the amplitude of frequency band between 40 and 80 Hz.

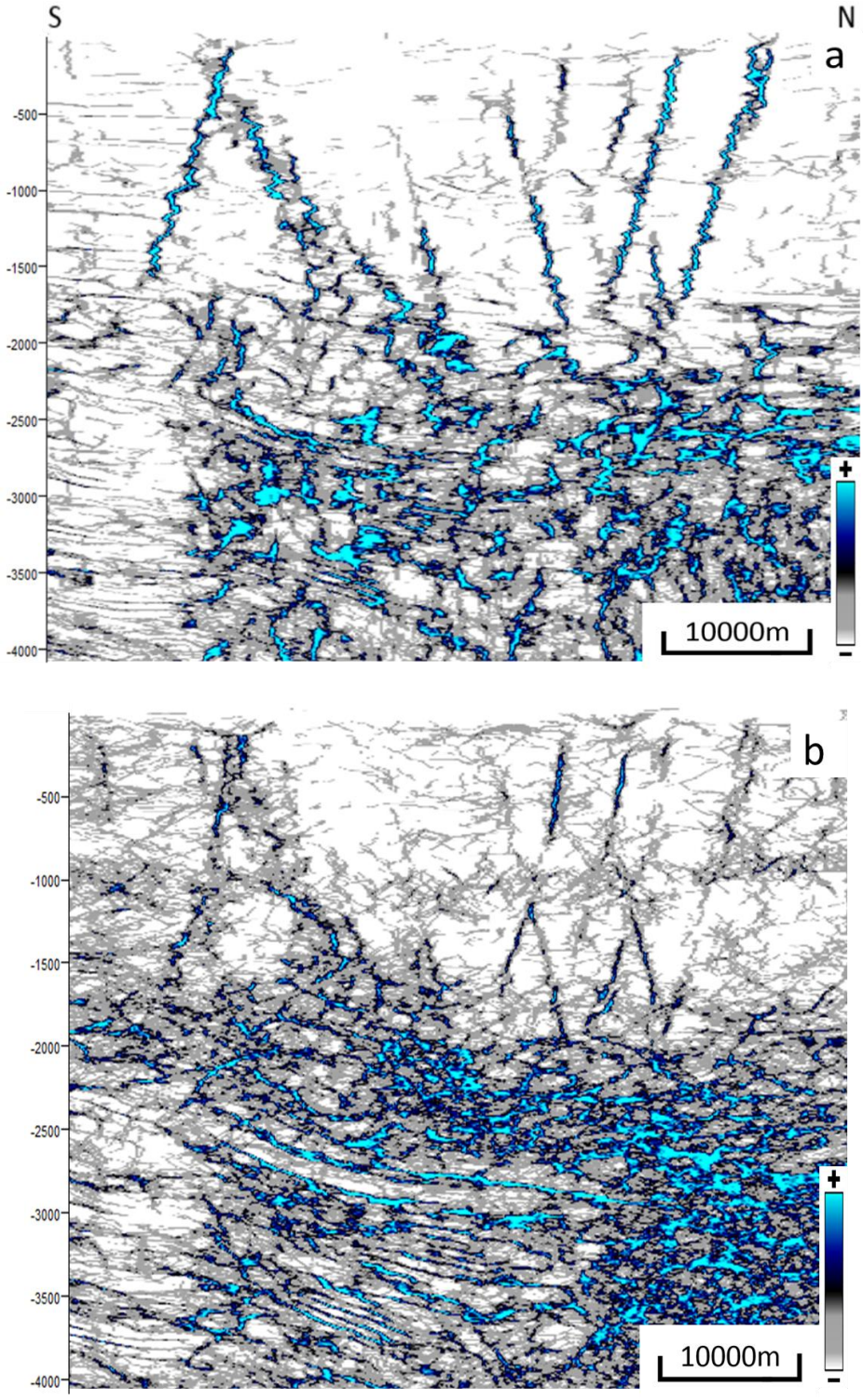

Figure 4. Inline 665 and resulting ant tracking maps using different attributes. (a) Chaos and Variance combined. (b) Combined attributes applied after Graphic Equalizer. (c) Same as (b) but after Variance attribute. (d) Same as (b) but after Chaos attribute. Red oval areas represent areas with highlighted enhancement on fault visualization.

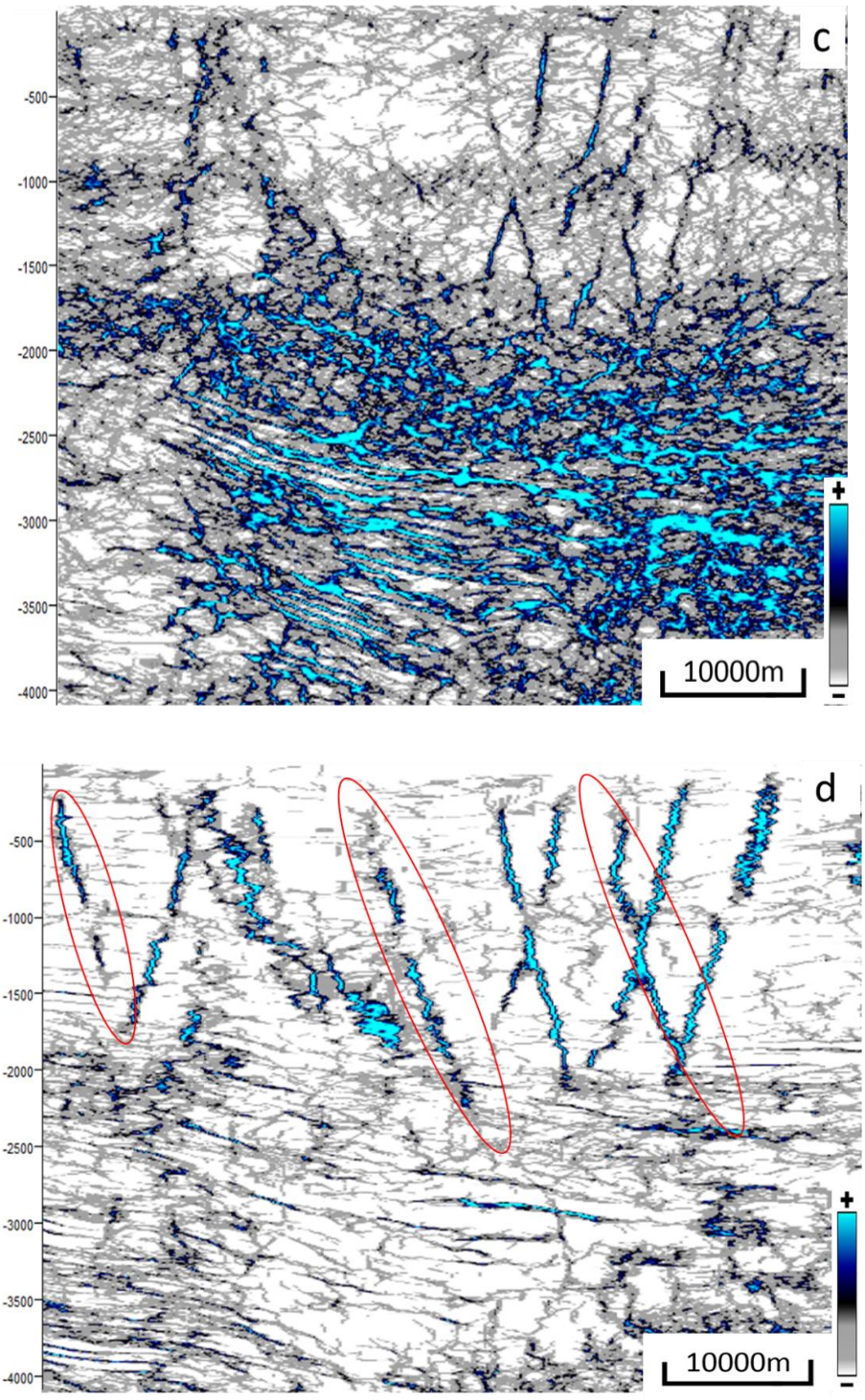

Figure 4. Inline 665 and resulting ant tracking maps using different attributes. (a) Chaos and Variance combined. (b) Combined attributes applied after Graphic Equalizer. (c) Same as (b) but after Variance attribute. (d) Same as (b) but after Chaos attribute. Red oval areas represent areas with highlighted enhancement on fault visualization. (Cont.)

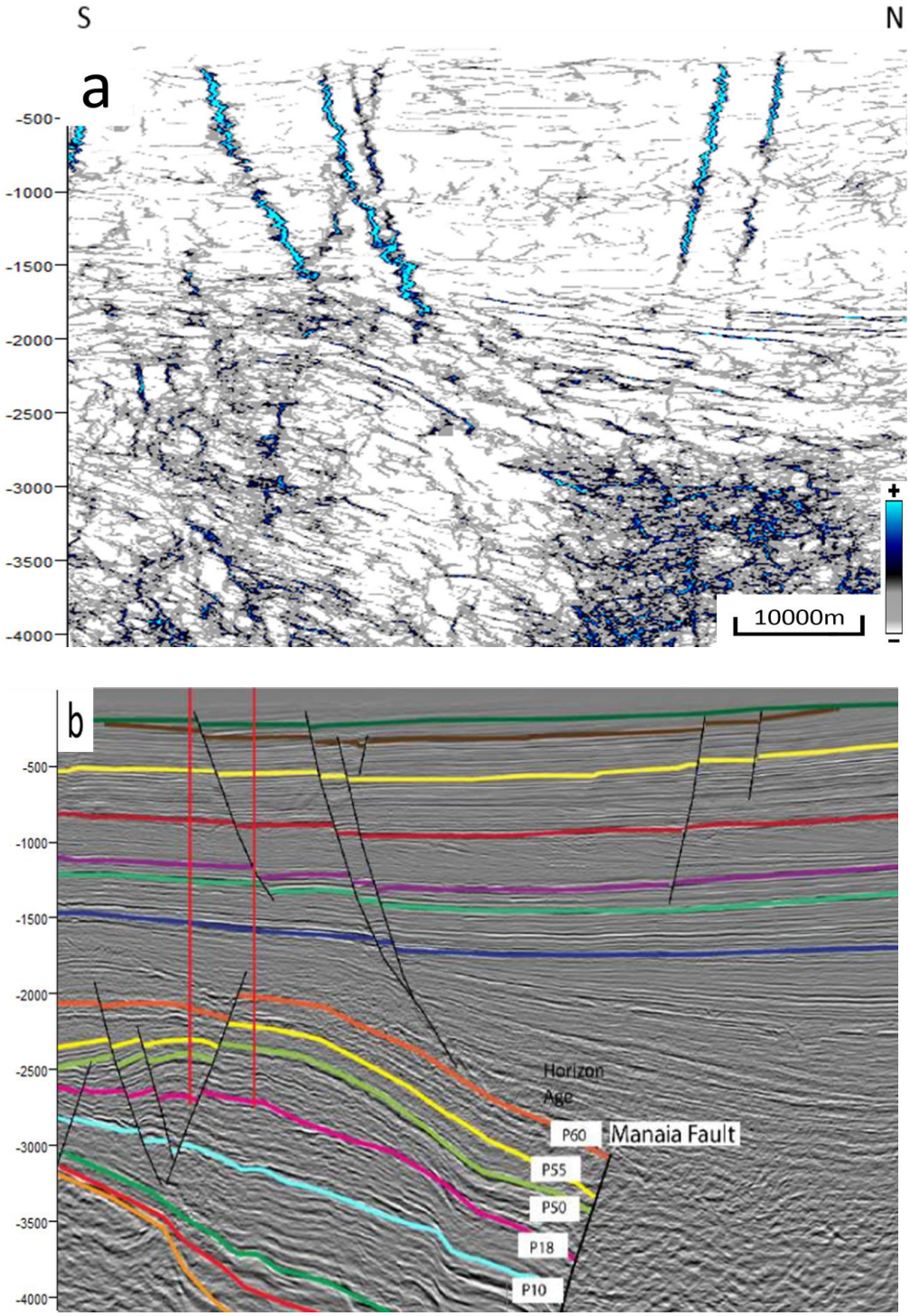

Figure 5. Comparison of the ant tracking result and the conventional fault interpretation. (a) Ant tracking map of inline 692. (b) Conventional fault interpretation of the same inline (Sykes, 2012).

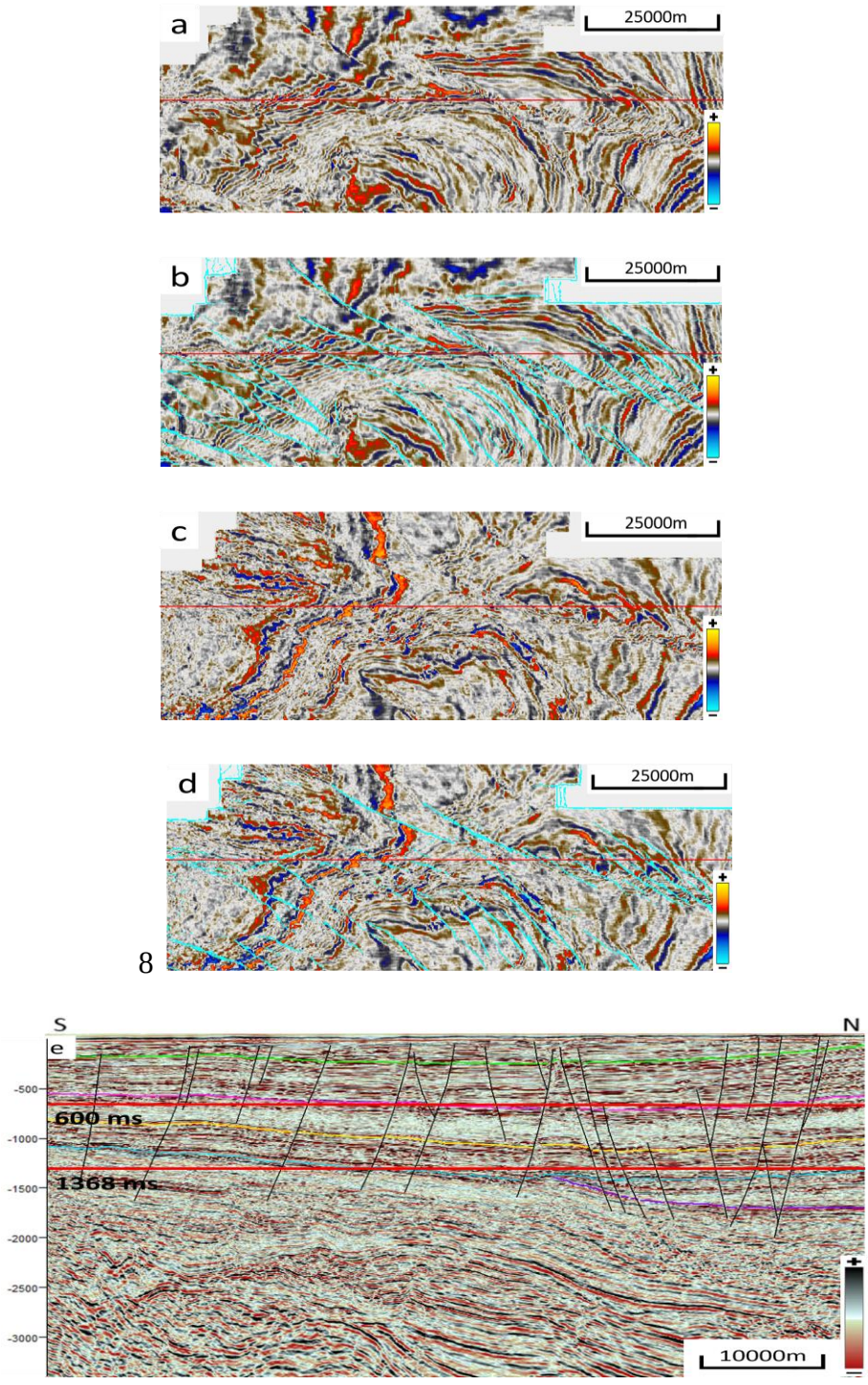

8

Figure 6. (a) Time slice at 600 ms. (b) Combined ant tracking with seismic volume. (c) Time slice at 1368 ms. (d) Combined ant tracking with seismic volume. (e) Vertical section of inline 665.

REFERENCES

Basir, H. M., A, Javaherian. and M.T Yaraki., 2013, Multi-attribute ant tracking and neural network for fault detection: A case study of an Iranian oilfield: *Journal of Geophysics and Engineering*, 10, no.1, 015009. http://dx.doi.org/10.1088/1742-2132/10/1/015009.

Fohrmann, M., E. Reid, M.G. Hill, P.R. King, H. Zhu., K.J. Bland, D.P. Strogen, L. Roncaglia and G.P.L. Scott, 2012, Seismic reflection character, mapping and tectono-stratigraphic history of the Kupe area (4D Taranaki Project), south-eastern Taranaki Basin.: *GNS Science report* 2012/36 62 p.

Hemmings-Sykes, S., 2012, The influence of faulting on hydrocarbon migration in the Kupe area, south Taranaki Basin, New Zealand: *M.S. thesis*, Victoria University of Wellington.

Henery. F., T. Trimbitasu and J. Johnson, 2011, An integrated workflow for reservoir sweet spot identification: *2011 Gussow Geoscience Conference*, Banff, Alberta.

Jansen, K., 2005, Seismic investigation of wrench faulting and fracturing at Rulison Field, Colorado: *Doctoral dissertation*, Colorado School of Mines.

Randen, T., E. Monsen, C. Signer, A. Abrahamsen, J.O. Hansen, T. Sæter and J. Schlaf, 2000, Threedimensional texture attributes for seismic data analysis: *70th SEG Technical Program Expanded Abstracts*, 668-671. http://dx.doi.org/10.1190/1.1816155

Roncaglia, L., 2006, Stratigraphy, well correlation and seismic-to-well tie in the Upper Cretaceous to Pliocene interval in the Kupe region, Taranaki Basin, New Zealand, Introduction to the stratigraphic database in PETREL, Vol. 2008: *GNS Science*.

Stagpoole, V. and A. Nicol, 2008, Regional structure and kinematic history of a large subduction back thrust, Taranaki Fault, New Zealand: Journal of Geophysical Research: *Solid Earth*, 113, B1. http://dx.doi.org/10.1029/2007JB000517

II. COMPACTION AND CEMENT VOLUME ANALYSES OF THE LOWER WILCOX SANDSTONE ALONG THE TEXAS GULF COAST

Tianze Zhang*, Yani Lin, Kelly H. Liu, and Stephen S. Gao,

Missouri University of Science and Technology

ABSTRACT

The Lower Wilcox strata are proven to be a good quality reservoir along the Central Gulf Coast of Texas. However, the complexity of its sedimentary environment makes it hard to accurately locate the isolated productive sand. In this study, rock physics analyses are carried out to provide a better understanding of the reservoir properties. Bulk density, P-wave velocity, and elastic moduli are extracted from four wells for analyzing the depth and temperature effects on compaction. A combination of three effective medium models is used for cement volume diagnostics.

1. INTRODUCTION

Rock physics plays an essential role in understanding sedimentary basins and reservoir characteristics. It has become a crucial part of quantitative interpretation, by linking reservoir properties such as density and porosity with seismic properties (Avseth, 2015). The effective physical properties of rocks extracted from wells can be used to infer lithological and mineralogical characteristics.

The primary process leading to temporal variations in sediment properties within the rock is compaction (Bjorlykke and Jahren, 2010). Mechanical compaction dominates

the process to 2-4 km depth, depending on the geothermal gradient. The magnitude of mechanical compaction is affected by the difference between lithostatic pressure and pore pressure. Porosity reduction during this process is due to the closure of fracture and cleavage of brittle grains and plastic deformation of ductile grains (Bjorlykke et al., 1989). In sandstone, chemical compaction takes over after the temperature reaches 70-80°C. It involves mineral dissolution and precipitation. Quartz is the most common cement type. At the initial stage of chemical cementation, a small amount of cement can cause significant stiffness increase (Dvorkin and Nur, 1996).

Our analyses focus on the early Eocene Lower Wilcox strata in southern Texas, which is mostly characterized by sandstone-rich deposits of fluvial and deltaic systems (Fisher and McGowen, 1967). Reservoir physical property variations and cement volume distributions are analyzed and modeled using data from four exploration wells. Density and acoustic logs are cross-plotted with depth to identify the transition zone from mechanical to chemical compaction. The temperature effect is investigated by using the shear modulus. A combination of friable-sand model, contact cement model, and constant cement model is utilized to investigate the physical properties of the Lower Wilcox strata and the cement volume distribution.

The transition zone location and the rock physical behavior of the reservoir rock are identified. The results build a solid foundation to carry on further rock physics diagnostics and amplitude versus offset study for better analyses of the reservoir strata.

2. DATA AND METHOD

Four exploration wells are used for the rock physics evaluation of the Lower Wilcox Sandstone Formation. Except for Well-1 which penetrates through the pay sand in the Lower Wilcox Formation, the rest are dry holes.

To evaluate the rock properties in a formation, it is crucial to locate the mechanical to chemical compaction transition zone. P-wave velocity is an ideal indicator to determine the transition zone as it increases dramatically with cement volume. Rock density can also change during this process, but it is not as prominent as the change of velocity.

A reference line representing the compaction process of 100% kaolinite is drawn to identify the transition point (Mondol, 2008). Relationships between the effective stress, velocity, and density are derived from the experimental equations. The effective stress is the difference between lithostatic stress and hydrostatic stress:

$$\sigma_{eff} = \sigma(z) - ph(z) \quad (1)$$

$$\sigma(z) = \rho_b g z \quad (2)$$

$$ph(z) = \rho_w g z \quad (3)$$

where σ(z) and ph(z) are lithostatic stress and hydrostatic pressure, respectively, g is gravity which is assumed to be 9.81 m/s2, ρb is the bulk density extracted from the density log, ρw is water density which is assumed to be a constant of 1.03 g/cm3, and Z is depth.

Temperature is an important factor in chemical compaction domain, as the precipitation of quartz cementation starts at a specific temperature range about 70°C-80°C. The thermal gradient is calculated by:

$$G_t = \frac{(BHT - AST)}{TVD} \quad (4)$$

where Gt is the thermal gradient in °C/m, BHT is the bottom hole temperature, and AST is the annual surface temperature which is set to be 15.56°C.

For modeling the elastic moduli and velocities, three cement models are introduced based on different sand models (Figure 1), including friable sand model (Dvorkin and Nur, 1996), contact sand model (Dvorkin et al., 1994), and constant sand model (Avseth et al., 2000).

The friable sand model represents a deteriorating process in which smaller grains deposit in the pore space between the well-sorted grains (Avseth et al., 2010). The dry elastic moduli at critical porosity are given by the Hertz-Mindlin theory. The moduli between zero and the critical porosity are interpolated by the modified lower Hanshin-Strikman bound.

The contact cement model represents the diagenesis process in which the rock stiffness is significantly increased because of cementation. It assumes that the varied sorting sand has the same contact cement volume (Avseth et al., 2010). The dry elastic moduli at critical porosity for a constant cement model are calculated from the contact cement model. The moduli at smaller porosity are interpolated by the lower Hashin-Strikman bound.

3. RESULTS AND DISCUSSIONS

We use four exploration wells located in southern Texas to extract data for the analyses. All wells have penetrated through the bottom of the Wilcox Formation. The shale volume is calculated using the Gamma Ray log. We use shale points (IGR>0.75) for compaction study, and sand points (IGR<0.25) for cement analysis. Because the acoustic log is not available for Well-3, the P-wave velocity for this well is calculated by the resistivity log using the Faust's equation. The bulk density in Well-4 is calculated by the neutron porosity.

The P-wave velocity and density are plotted against depth (Figure 2). The location of the transition zone is defined by the sudden velocity increase. One could easily misinterpret that the velocity change at the boundary between the Caliborne Group and the Upper Wilcox Formation is caused by mechanical to chemical transition. However, the Gamma Ray log indicates that such change is due to significant lithology variations at the boundary. The possible transition zone locates at about 2100 m depth for each well in the Lower Wilcox c Formation. In Well-1 and Well-4, the average velocity increases from 3300 m/s to 3500 m/s.

The bulk density and shear modulus color-coded by temperature are cross-plotted to determine the temperature range of the transition zone (Figure 3). By clustering the data with different gradient, a turning point indicating the temperature window of the transition zone is decided. The transition temperature range is from 60°C to 70°C for all the wells. The result corresponds to the initiation temperature point of the quartz cementation. When the temperature rises, the shear wave velocity increases dramatically,

while the density remains almost unchanged. This is different from lower temperature conditions where mechanical compaction dominates. Well-4 does not follow the pattern from other three wells mainly because the density in this well is not accurately measured but calculated instead.

We use Gassmann's fluid substitution to calculate the saturated elastic moduli to generate the cement models (Figure 4). The resulting cement volume for the constant cement model from the top to the bottom is 8%, 4%, and 2%, respectively.

Well-4 shows the expected pattern that the shallower formation contains less cement. The Lower Wilcox c Formation sits around the 2% cement volume line, the lower Wilcox b Formation occupies the space between 2% and 4%, and the Lower Wilcox a Formation lies around the 4% line. With decreasing porosity, the stiffness of the rock increases as the deterioration sorting process deposits the quartz among grain pores. Well-2 shows the opposite pattern. The Lower Wilcox c Formation has the most cement volume, whereas the deepest Lower Wilcox a Formation contains the least. However, the porosity still acts in a regular pattern that the lowest formation has the smallest porosity.

Although Well-1 and Well-3 are nearby, Well-1 has about 2% more contact cement volume than Well-3. Both wells show a wide range of porosity without any significant increase in S-wave velocity. The sand points located near or outside the friable sand model do not show any cement content. The porosity reduction of those sand points is possibly induced by mechanical compaction. As both wells located near to each other, they may share similar sedimentary environment.

4. CONCLUSIONS

Our analyses show that the transition zone from compaction to chemical cementation takes place around 2100 m depth for all wells, at temperatures ranging from 60°C-70°C, which is consistent with results from thermal gradient analyses. The porosity reduction in the Lower Wilcox Formation shows that poor sorting plays a more significant role than mineral precipitation. The irregular distribution pattern in Well-1 and Well-3 is possibly caused by the depositional environment that differs from the other wells.

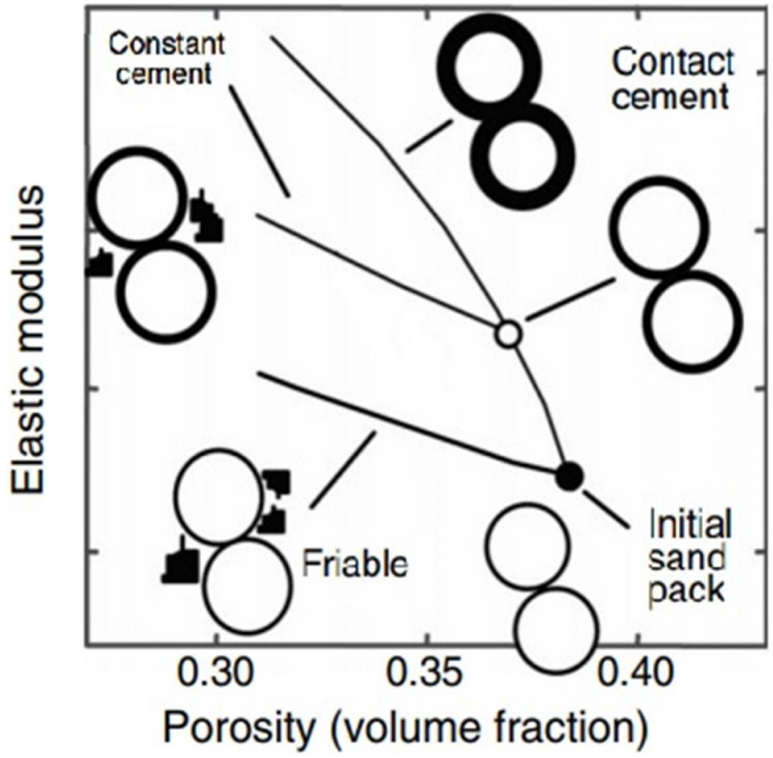

Figure 1. Illustration of three effective medium models for high porosity sand. The elastic modulus can be bulk or shear (Modified from Avseth et al., 2010).

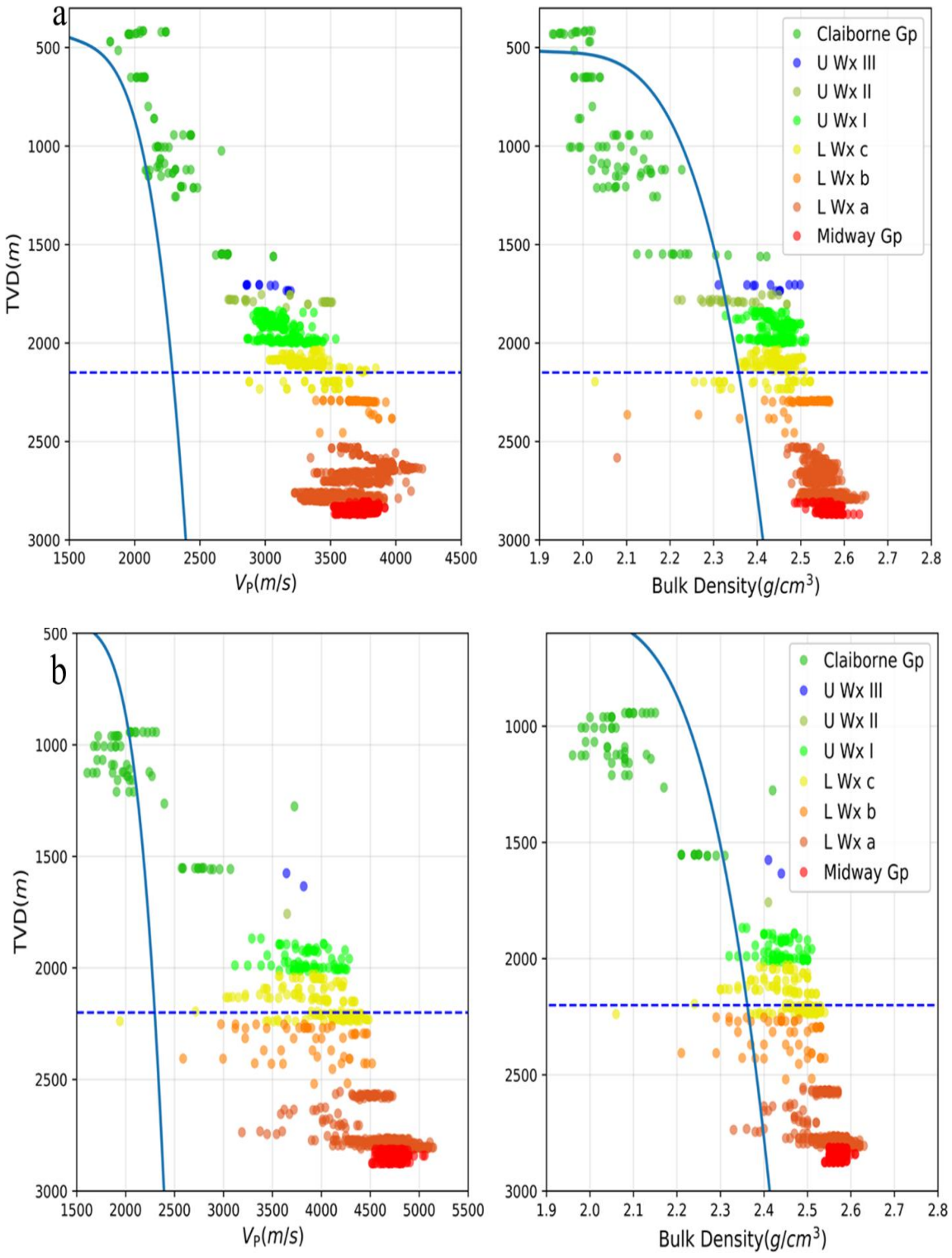

Figure 2. Depth versus Vp and bulk density plots of shale data points (IGR > 0.75) with 100% kaolinite experimental curve. (a) Well-1. (b) Well-2. (c) Well-3. (d) Well-4.

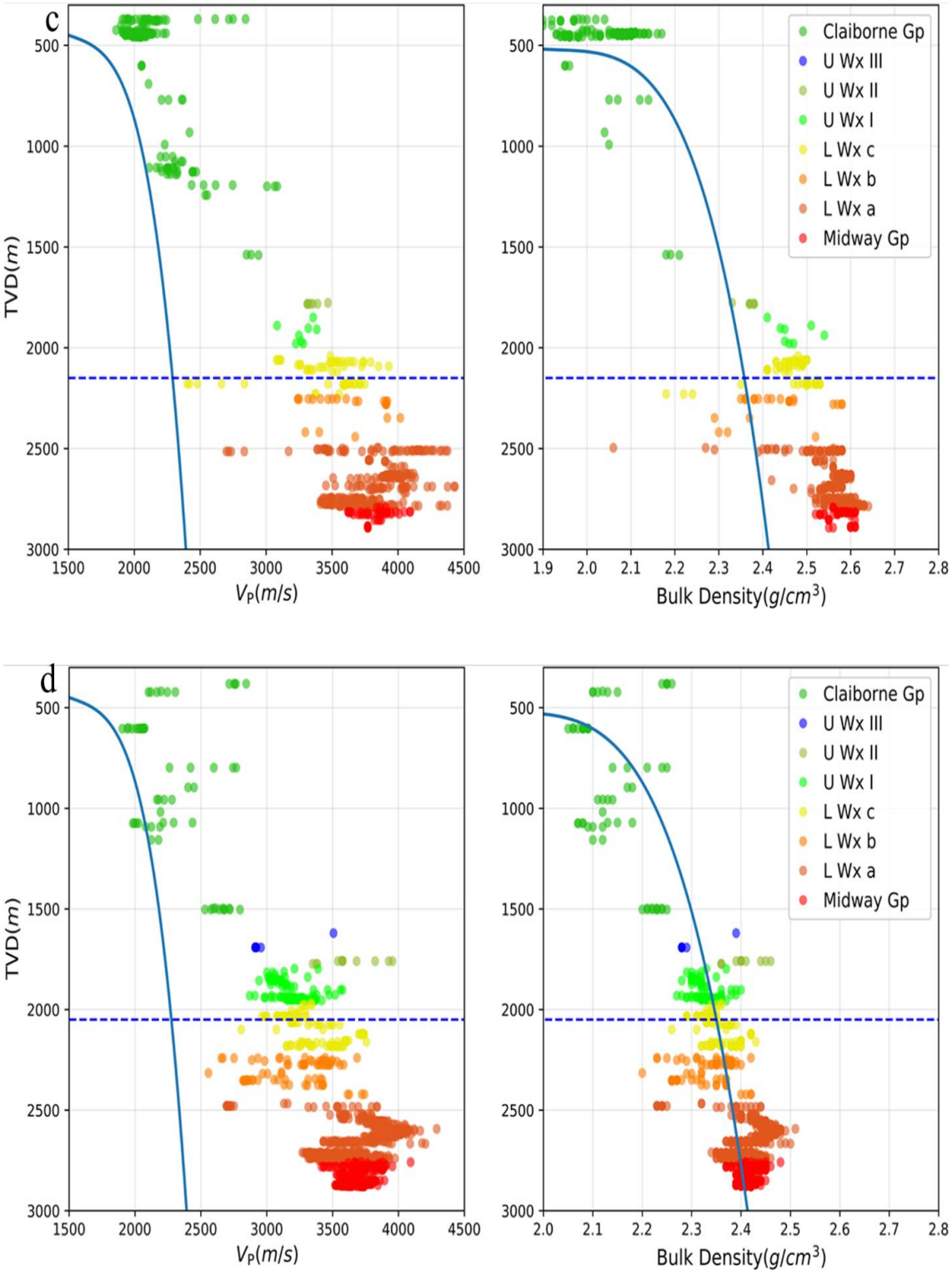

Figure 2. Depth versus Vp and bulk density plots of shale data points (IGR > 0.75) with 100% kaolinite experimental curve. (a) Well-1. (b) Well-2. (c) Well-3. (d) Well-4. (Cont.)

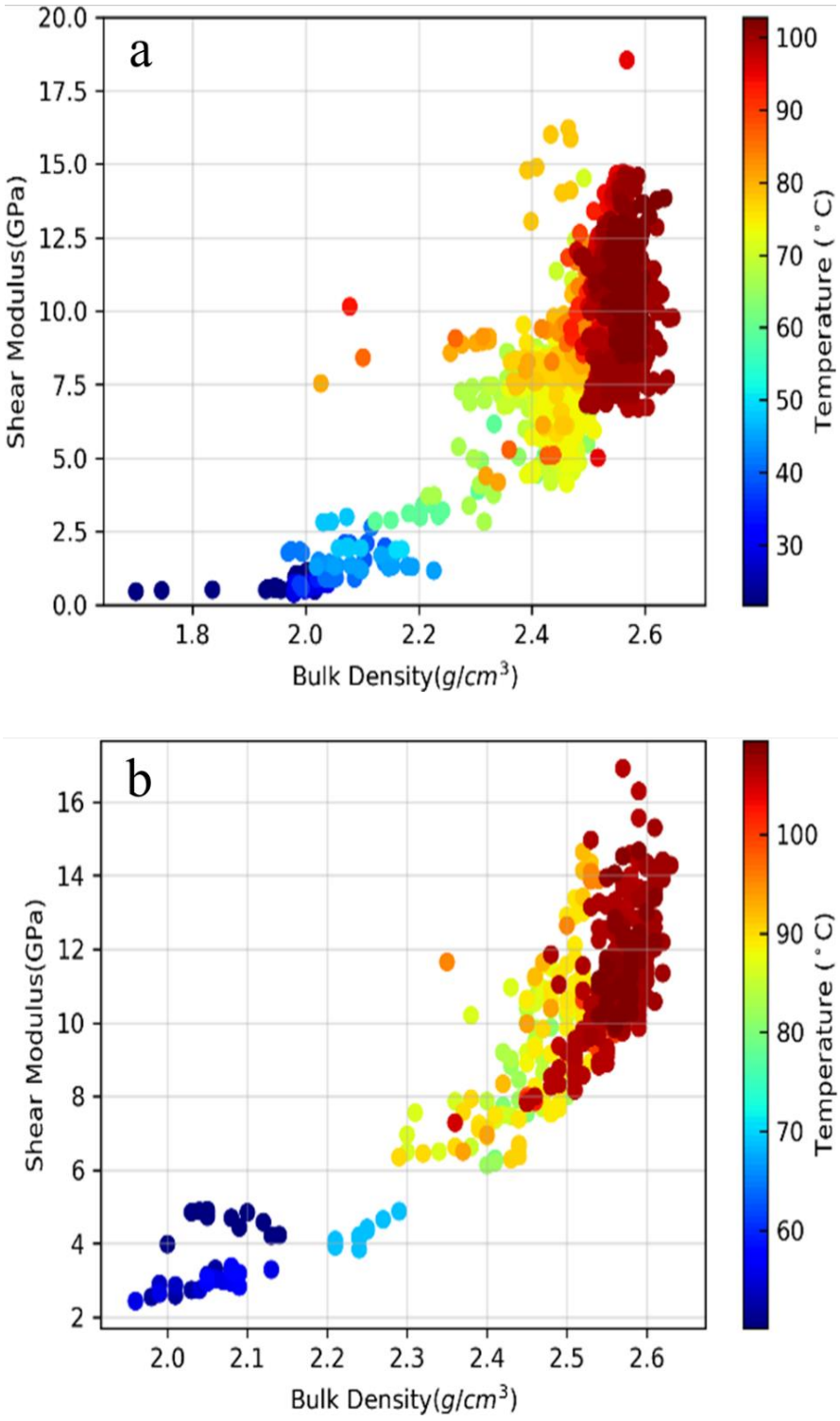

Figure 3. Bulk density versus shear modulus plots of shale data (IGR > 0.75), color-coded in temperature showing the temperature range of the mechanical to chemical compaction. (a) Well-1. (b) Well-2. (c) Well-3. (d) Well-4.

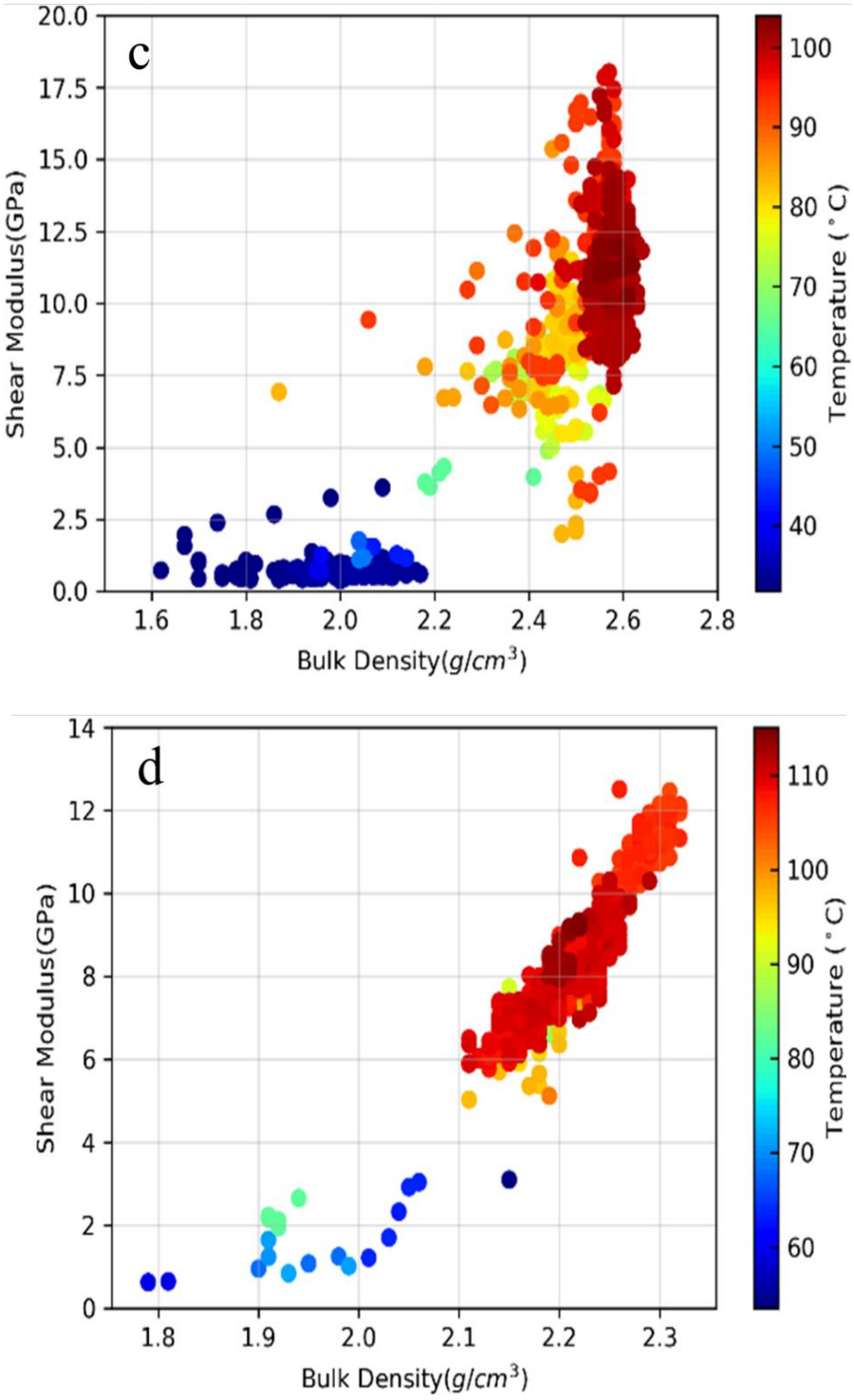

Figure 3. Bulk density versus shear modulus plots of shale data (IGR > 0.75), color-coded in temperature showing the temperature range of the mechanical to chemical compaction. (a) Well-1. (b) Well-2. (c) Well-3. (d) Well-4. (Cont.)

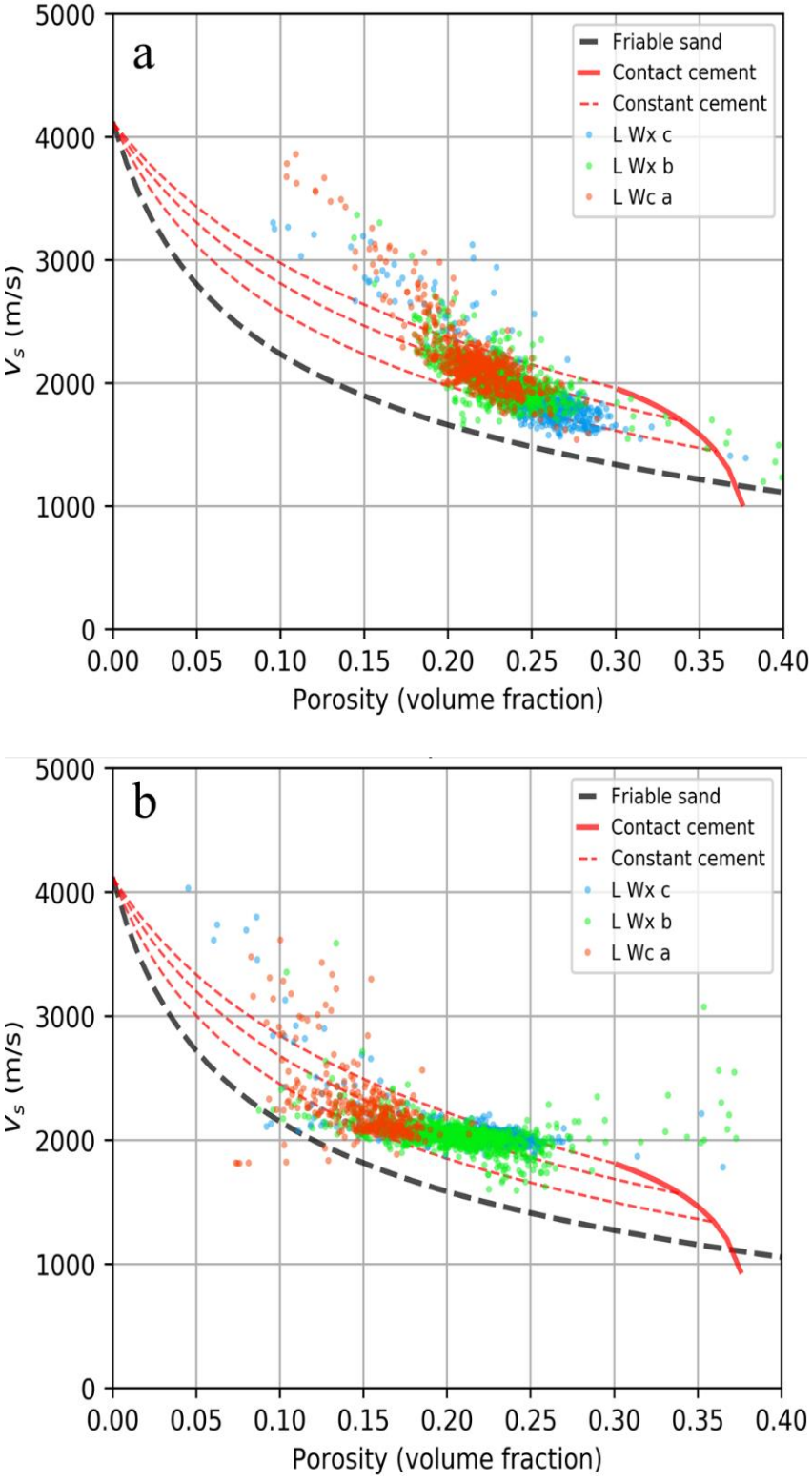

Figure 4. Porosity versus shear wave velocity plots. The constant cement volume (red dashed line) from high to low is 8%, 4%, and 2%, respectively. (a) Well-4. (b) Well-2. (c) Well-1. (d) Well-3.

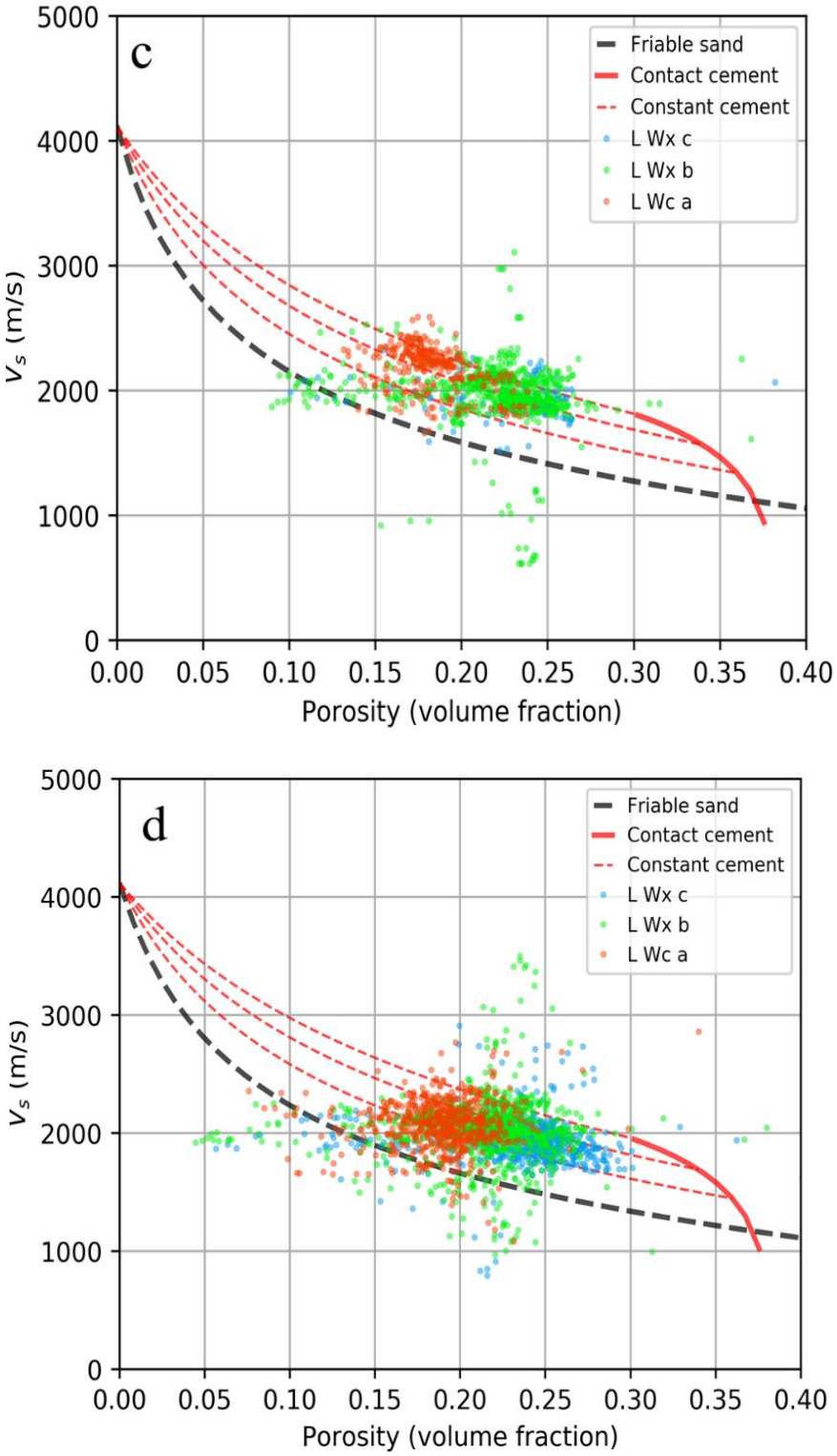

Figure 4. Porosity versus shear wave velocity plots. The constant cement volume (red dashed line) from high to low is 8%, 4%, and 2%, respectively. (a) Well-4. (b) Well-2. (c) Well-1. (d) Well-3. (Cont.)

REFERENCES

Avseth, P., J. Dvorkin, G. Mavko, and J. Rykkje, 2000, Rock physics diagnostic of North Sea sands: Link between microstructure and seismic properties: *Geophysical Research Letters*, 27(17), 2761-2764.

Avseth, P., T. Mukerji, G. Mavko, and J. Dvorkin, 2010, Rock-physics diagnostics of depositional texture, diagenetic alterations, and reservoir heterogeneity in high-porosity siliciclastic sediments and rocks—A review of selected models and suggested work flows: *Geophysics*, 75(5), 75A31-75A47.

Avseth, P., 2015, Explorational rock physics: The link between geological processes and geophysical observables: *Petroleum Geoscience*, 455-488.

Bjørlykke, K., M. Ramm, and G.C. Saigal, 1989, Sandstone diagenesis and porosity modification during basin evolution: *Geologische Rundschau*, 78(1), 243-268.

Bjørlykke, K., and J. Jahren, 2010, Sandstones and sandstone reservoirs: *Petroleum Geoscience*, 113-140.

Dvorkin, J., and A. Nur, 1996, Elasticity of high-porosity sandstones: Theory for two North Sea data sets: *Geophysics*, 61(5), 1363-1370.

Dvorkin, J., A. Nur, and H. Yin, 1994, Effective properties of cemented granular materials: *Mechanics of materials*, 18(4), 351-366.

Fisher, W.L., and J.H. McGowen, 1967, Depositional systems in the Wilcox Group of Texas and their relationship to occurrence of oil and gas (1): *Gulf Coast Association of Geological Societies Transactions*, 17, 105-125.

Mondol, N.H., K. Bjørlykke, and J. Jahren, 2008, Experimental compaction of clays: Relationship between permeability and petrophysical properties in mudstones: Petroleum Geoscience, 14(4), 319-337. Ødegaard, E.R.I.K. and P. Avseth, 2003, Interpretation of elastic inversion results using rock physics templates: *65th EAGE Conference & Exhibition*.

III. PRE-STACK SIMULTANEOUS INVERSION FOR PETROPHYSICAL PROPERTIES OF THE LOWER WILCOX EROSIONAL REMNANT SANDSTONE ALONG THE TEXAS GULF COASTAL PLAIN

Tianze Zhang*, Yani Lin, Kelly H. Liu, and Stephen S. Gao

Missouri University of Science and Technology, Rolla, MO 65409

ABSTRACT

The lower Wilcox sand deposits encased between two continuous erosional sequences are of good reservoir quality and usually gas productive. However, the distribution of sedimentation is laterally scattered and hard to interpret in seismic data. Simultaneous inversion of petrophysical parameters such as P-impedance, S-impedance, and density by the integration of pre-stack data and well logs allows us to quantitatively characterize the reservoirs, and to distinguish them from the surrounding rocks. In this study, we use pre-stack inversion of the petrophysical parameters for the gas reservoir in an analog field. For wells that are missing sonic and density logs, we estimate the parameters using the time average equation and Gardner's equation, respectively. The estimation results are verified using well log correlations. Rock physics analyses are conducted to find the optimal parameters to characterize the producing sand. Our inversion results show a successful delineation of the reservoir using the Vp/Vs value. In addition, the sandstone is mapped in the crossplot of the inverted results.

1. INTRODUCTION

The lower Wilcox Group is mainly characterized as fluvial and deltaic deposits with high sediment influx rate (Devine & Wheeler, 1989; Galloway et al., 2011). The lower Wilcox sandstones are encased in a thick layer of mud-dominated prodelta sediments (Berg, 1979; Hargis, 2009; Olariu & Zeng, 2017). Hydrocarbon is generated from the lower Tertiary terrestrial source rock (Warwick, 2017), and oil and gas occurrence is highly related to the depositional facies (Fisher & McGowen, 1967). Extensive studies have been conducted using well logs and seismic data to depict the depositional system (Chuber, 1979; Devine & Wheeler, 1989; Schenewerk et al., 1994; Zeng et al., 2016; Sharman et al., 2017).

Our study focuses on the reservoir associated with erosional remnant sand, which is covered by the transgressive mud deposits. The surround shale acts as a barrier in both vertical and lateral directions and prevents the hydrocarbon from escaping, and the trapped sand becomes ideal reservoir for the accumulation of gas and oil. The average permeability of the sandstone varies from 17 md to 55 md, depending on cement volume (Berg, 1979). Although numerous studies have demonstrated the production potential of the remnant sand, the distribution of this type of reservoir is still unpredictable (Devine & Wheeler, 1989), and individual sands have not been identified on seismic data (Allen & Howell, 1987).

In our study, we relate the reservoir properties with geophysical parameters using data from an analog field located along the Texas Gulf Coast (Figure 1). We use P-impedance versus V_p/V_s for rock physics analysis to describe the reservoir properties, and

utilize the optimal geophysical parameters to distinguish the reservoir from the surrounding rocks. Then we apply the pre-stack seismic inversion to delineate the hydrocarbon saturated sand body.

2. DATA AND METHOD

A 3D pre-stack seismic data set which contains 166 inlines and 261 crosslines was used for the inversion process. Offset ranges from 1000 ft to 19000 ft, and the main frequency ranges from 10 Hz to 40 Hz, with a dominant frequency about 28 Hz. For rock physics and inversion analyses of the entire Wilcox group, we used two producing wells that penetrate the same pay sand interval with over 80 ft thickness.

Velocity and density logs are crucial for the inversion process. Both wells contain deep induction and gamma ray logs, however density and sonic logs are missing. The time average equation was utilized to estimate the velocity from resistivity, and to calculate the density from the velocity result. The time average equation is more effective than the other empirical relations in the section deeper than 5000 ft in the Texas Gulf Coast area (Adcock, 1993). The time average equation for the two-lithology matrix form is given by

$$\Delta T = \Delta T_F f_R + [\Delta T_{sh} f_{sh} + \Delta T_{sd}(1 - f_{sh})](1 - f_R), \quad (1)$$

where ΔTF, ΔTsh, and ΔTsd are the sonic travel time for fluid, shale, and sand, respectively. The fractional shale volume, fsh, can be calculated by the gamma ray log. The fractional porosity, fR, was calculated by Archie's equation assuming 100 percent

water saturation, the equation under this circumstance which with 100 percent water saturation is given by

$$f_R = (aRw/{S_w}^n Rt)^{1/m}, \quad (2)$$

where the constants a, n, and mare 0.81, 2, and 1, respectively. The Rw values for two wells were estimated as 0.035 Ω-m for Well-1 and 0.03 Ω-m for Well-2.

A lithology specific Gardner's equation for sandstone and shale was used for bulk density estimation, given by

$$\text{Fsh}<0.25: \rho_b = -0.0115{V_P}^2 + 0.261V_P + 1.515 \quad (3)$$

$$\text{Fsh} >0.25: \rho_b = -0.0261{V_P}^2 + 0.373V_P + 1.458 \quad (4)$$

For shear wave estimation, we used water saturated Vp-Vs relation based on clay content (Han et al., 1986), given by

$$\text{Fsh}<0.25: V_S = 0.754V_P - 0.657 \quad (5)$$

$$\text{Fsh}>0.25: V_S = 0.842V_P - 1.099 \quad (6)$$

For the gas-saturated situation, we applied the Krief's equation (Krief et al., 1990), given by

$$V_S = \sqrt{\frac{{V_P}^2 - 0.902}{2.282}} \quad (7)$$

The simultaneous pre-stack inversion was conducted using the method proposed by Hampson et al. (2005), which was based on the Aki-Richards equation and the linear relation between the logarithm of P-impedance, S-impedance, and density. The pre-stack data were transferred into angle domain ranging from 0-45o. The angle dependent wavelets were extracted from the volume. An initial model of P-impedance, S-impedance, and density was built using both wells for the inversion iteration process. The

inversion results were used to calculate various elastic parameters to identify the hydrocarbon anomalies.

3. RESULTS AND DISCUSSIONS

The gamma ray and resistivity logs of the two wells were normalized into the same range before calculating the shale volume and porosity. Then we used the time average equation to calculate the sonic log. The sonic travel time parameters for fluid, shale, and sand are 165, 97, and 53 us/ft, respectively. The lithology specific Gardner's equation was applied to calculate the density log, and the shale volume threshold used for separating the shale and sandstone is 0.25.

We conducted seismic-to-well tie for both wells to match the well log information and seismic. The correlation coefficient is 0.419 for Well-1 and 0.436 for Well-2. The values represent a good estimation on density and velocity logs, considering the wells containing both logs only have correlation coefficients ranging from 0.5 to 0.6 in the nearby field.

The rock physics analysis was performed in order to find the optimal elastic parameter to characterize the reservoir. P-impedance versus Vp/Vs value crossplots were produced for both wells. A clear separation between the gas sand and the background trend was observed (Figure 4). The colored sections projected to the wells from the crossplots correspond with the pay sand sections in each well. The gas sand has Vp/Vs values from 1.54-1.62 and P-impedance values from 23000-34000. The crossplot showing Vp/Vs value can be the optimal indicator separating the gas reservoir from the

surrounding rocks, while solely inversing the P-impedance is insufficient to delineate the reservoir sand.

The pre-stack inversion analysis was then applied on a conditioned angle gather seismic section using both wells. The P-impedance, S-impedance, and density are inverted by the algorithm simultaneously. The analyses indicate that the synthetic traces correlate well with the seismic data, and the inverted logs are similar to the original logs (Figure 5).

Pre-stack inversion results across the arbitrary seismic line A-A' containing both wells indicate that the remnant sand reservoir between the two erosional sequences at about 2100 ms has low Vp/Vs (Figure 6).

The reservoir location was mapped through a crossplot of inverted P-impedance versus inverted Vp/Vs (Figure 7). We isolated the similar area to the rock physics analyses from wells, and projected it into the seismic section. A more explicit separation of the reservoir, which is represented by the red shaded area in Figure 8, can be observed.

4. CONCLUSIONS

Our analyses show that for depth that is larger than 5000 ft, the time average equation can provide robust estimation on velocity using the resistivity log. The rock physics analyses from wells indicate that the sand reservoir has low Vp/Vs values ranging from 1.54 to 1.62 and a wide range of P-impedance values ranging from 23000 to 34000. The pay sand has a clear separation from the surround shales. A Vp/Vs volume is generated through the pre-stack simultaneous inversion, and we observe a gas reservoir at

2100 ms with low Vp/Vs values encasing between the two erosional sequences. We crossplot the P-impedance and Vp/Vs from the inversion result and pick the similar area as the rock physics analyses from wells. The cross-section shows a better delineation of the reservoir, and reduces the ambiguity caused by the low Vp/Vs anomaly that observed in the shallow area from 1900 ms to 2000 ms.

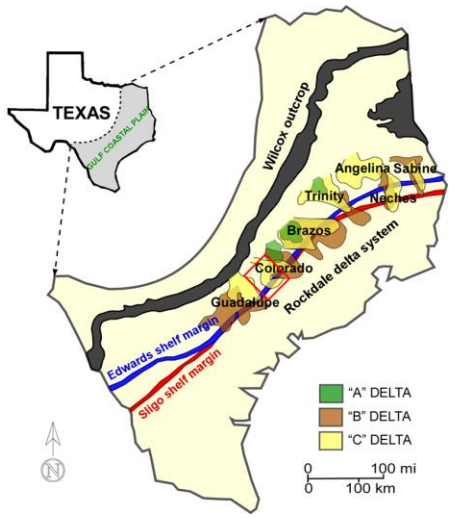

Figure 1. Location of the Texas Gulf Coast (Modified from Olariu & Zeng, 2017). The study area is indicated by the red rectangle.

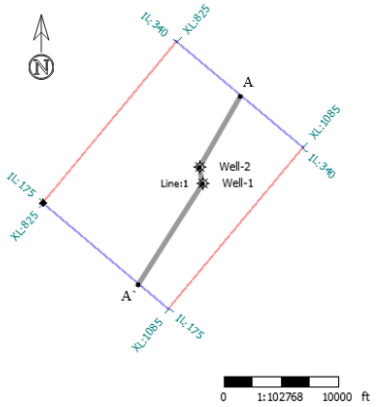

Figure 2. Basemap showing seismic and well locations. The grey line displays the location of the arbitrary line A-A'.

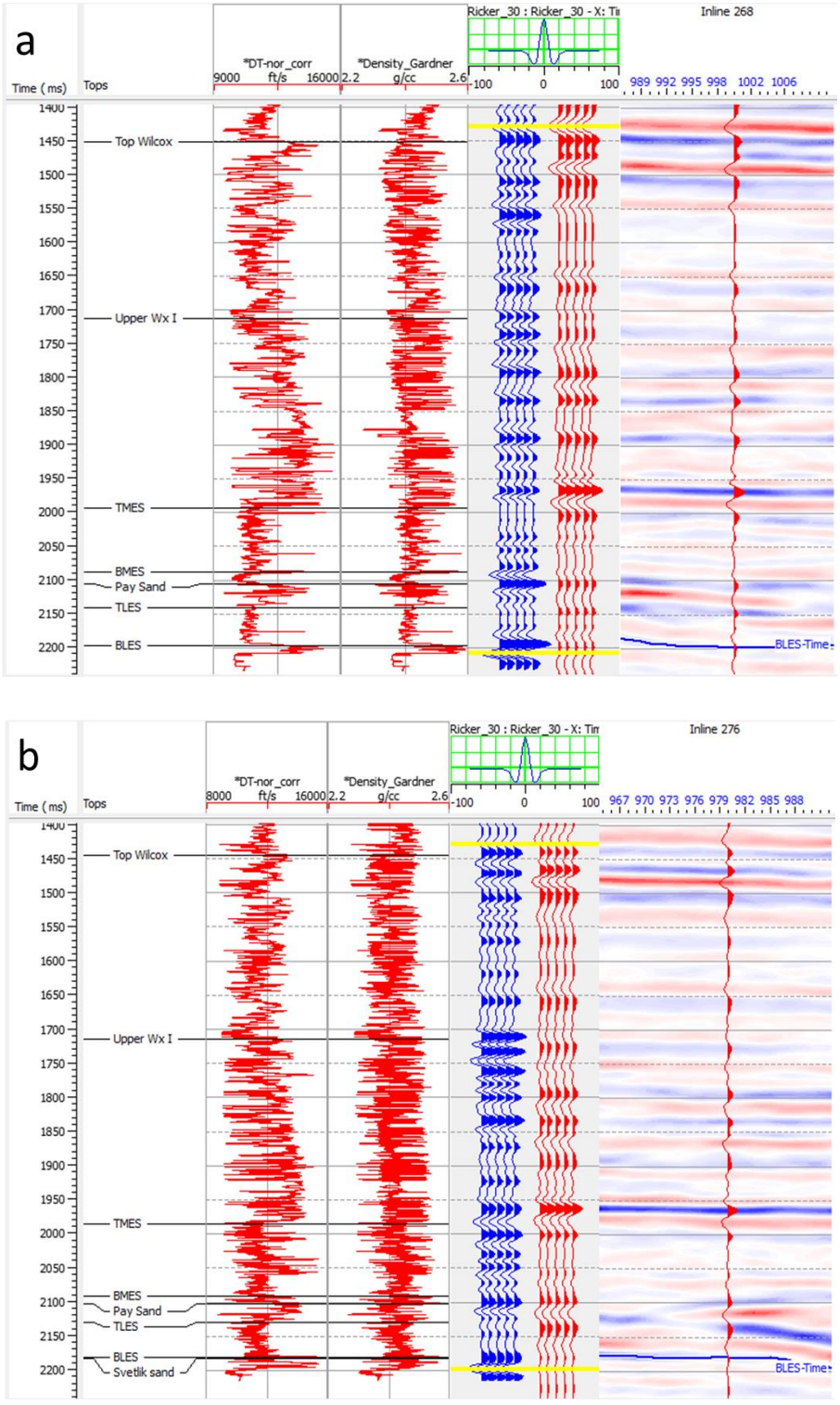

Figure 3. Log correlation using the estimated velocity and density. (a) Well-1. (b) Well-2.

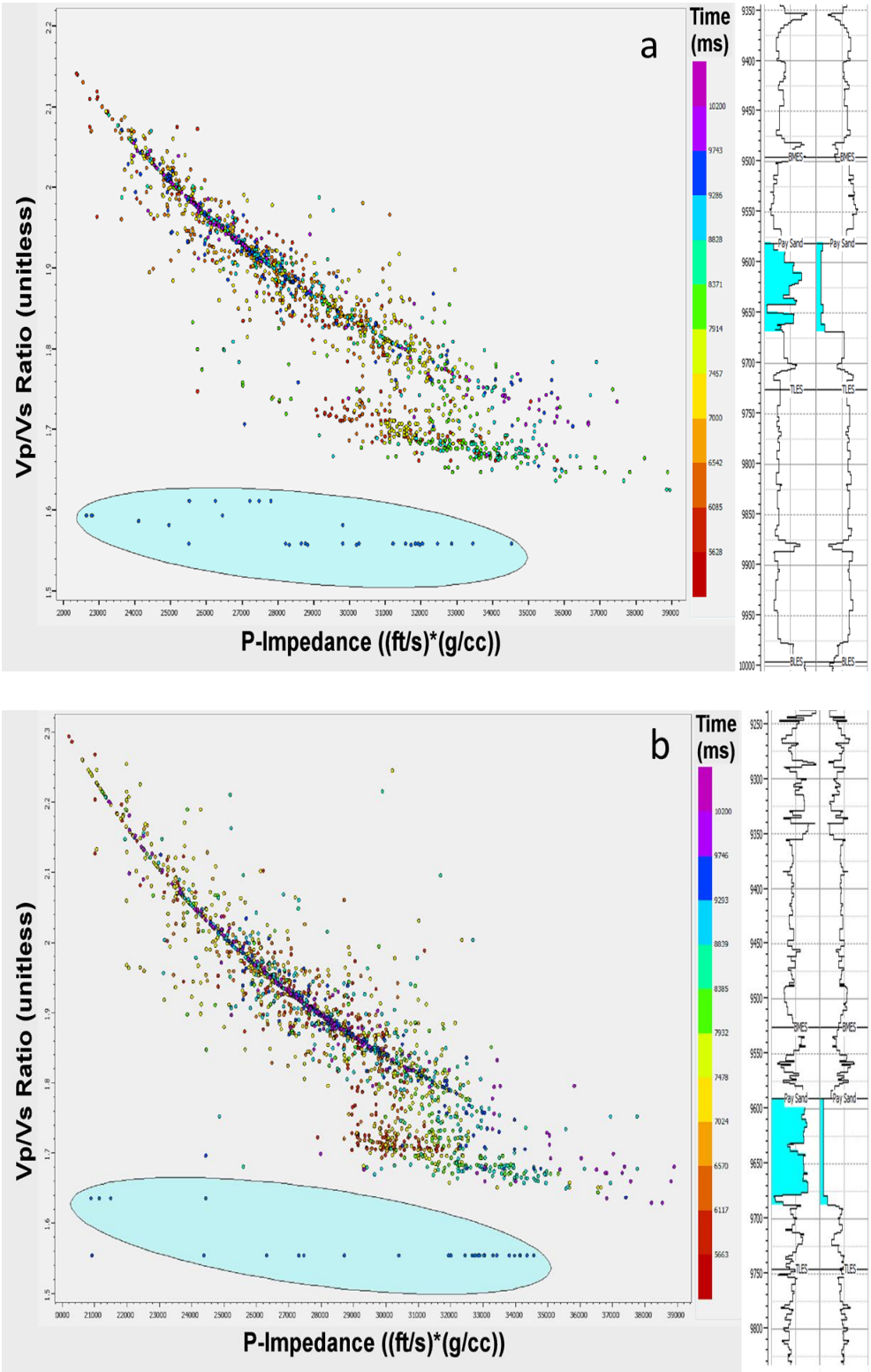

Figure 4. Rock physics analyses using acoustic impedance versus Vp/Vs. The blue circled area is equivalent to the blue section in the well, which represents the pay sand location. (a) Well-1. (b) Well-2.

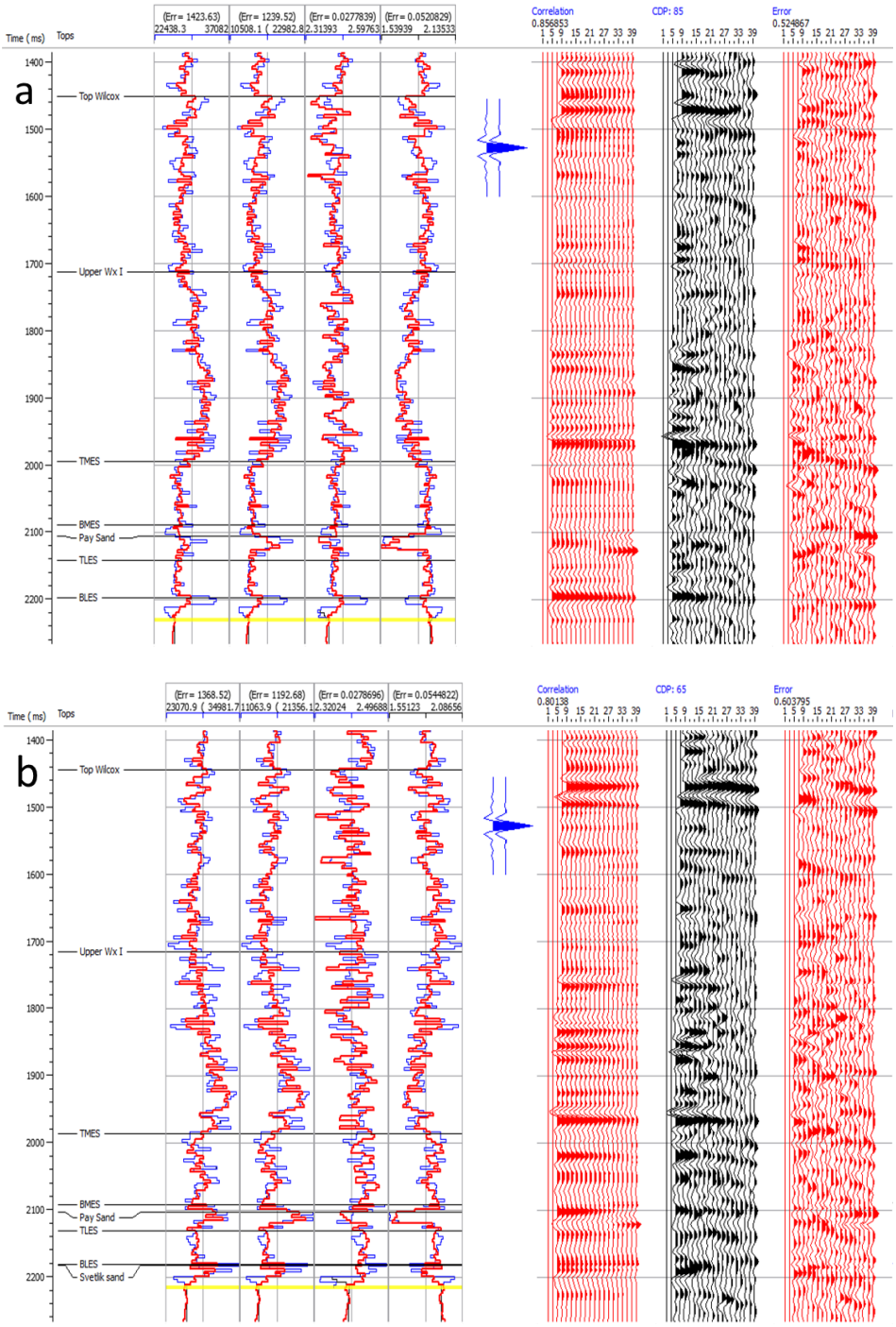

Figure 5. Inversion analyses for both wells. Log panels from left to right are P-impedance, S-impedance, density, and Vp/Vs. Original logs are in blue, and inverted logs are in red. (a) Well-1. (b) Well-2.

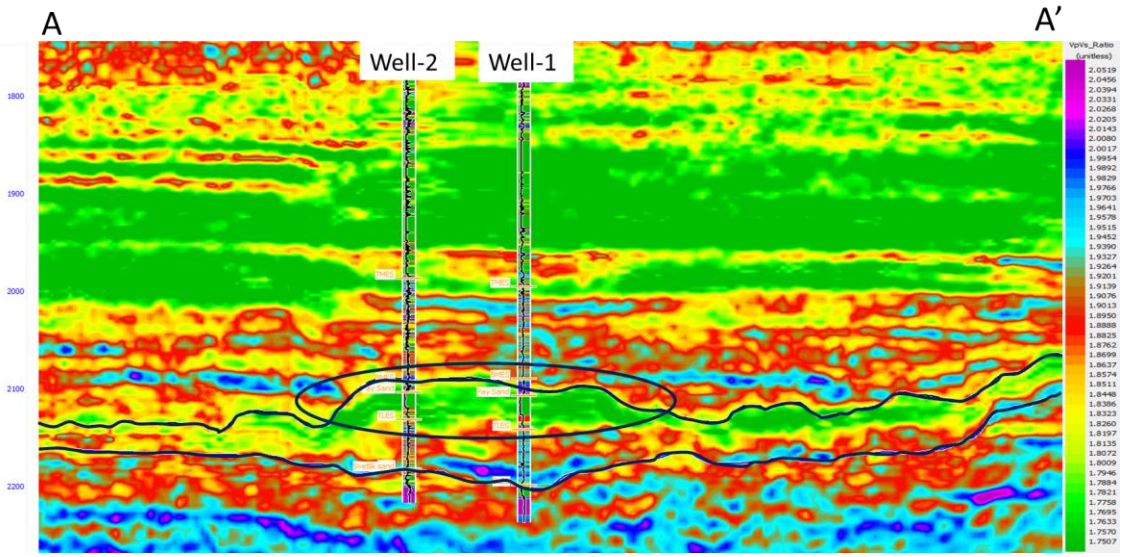

Figure 6. Vp/Vs for the arbitrary line A-A'. The oval at about 2100 ms outlines the gas reservoir interpreted by low Vp/Vs values. Wells from left to right are Well-2 and Well-1 with Vp/Vs log inserted. The upper horizon is the top of the middle erosional sequence, and the lower horizon is the base of the lower erosional sequence.

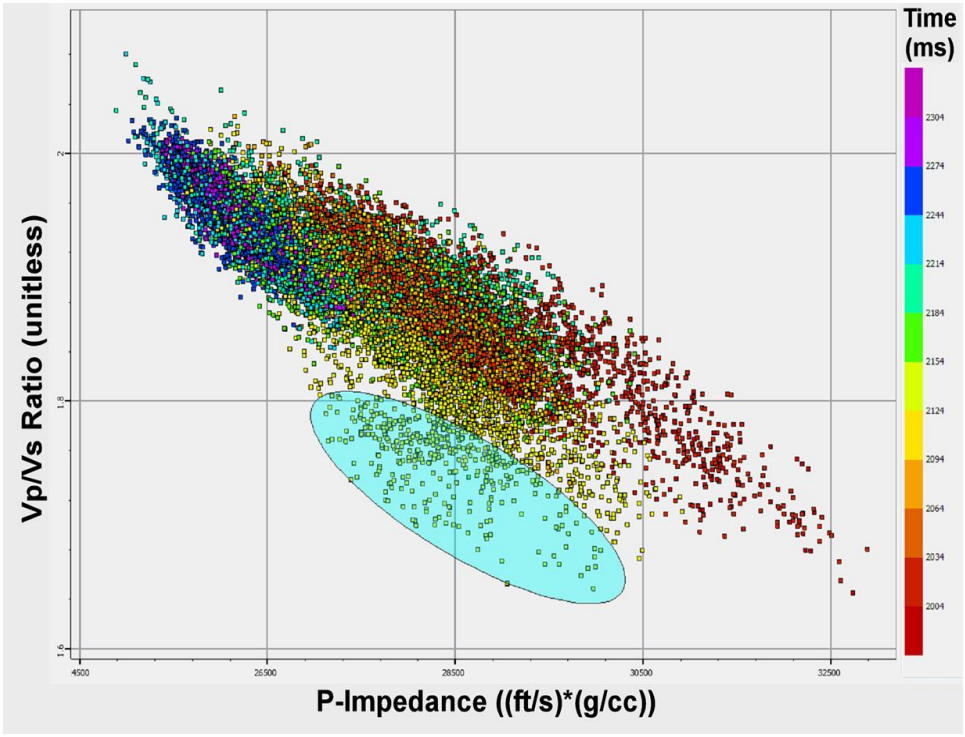

Figure 7. Inverted P-impedance versus inverted Vp/Vs.

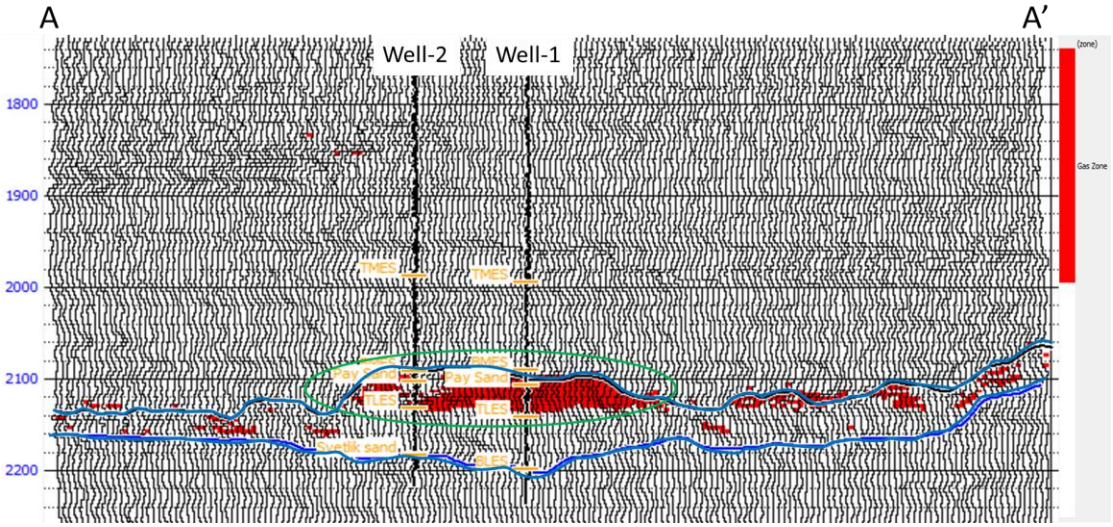

Figure 8. Cross-section A-A'. The green oval outlines the gas reservoir.

REFERENCES

Adcock, S., 1993, In search of the well tie: What if I don't have a sonic log?: *The Leading Edge*, 12(12), 1161-1164.

Allen, J., J. Howell Sr, 1987, Using "poor man's 3-D" to identify distributary channel sands in the Wilcox formation, Lavaca County, Texas: *The Leading Edge*, 6(10), 8-15.

Berg, R.R., 1979, Characteristics of lower Wilcox reservoirs. Valentine and South Hallettsville Fields, Lavaca County, Texas: *Gulf Coast Association of Geological Societies Transactions*, 29, 11-23.

Chuber, S., 1979, Exploration methods of discovery and development of lower Wilcox reservoirs in Valentine and Menking fields, Lavaca County, Texas: *Gulf Coast Association of Geological Societies Transactions*, 29, 42-51.

Devine, P.E., and D.M. Wheeler, 1989, Correlation, interpretation, and exploration potential of lower Wilcox valley-fill sequences, Colorado and Lavaca Counties, Texas: *Gulf Coast Association of Geological Societies Transactions*, 39, 57-74.

Fisher, W.L., and J.H. McGowen, 1967, Depositional systems in the Wilcox Group of Texas and their relationship to occurrence of oil and gas (1): *Gulf Coast Association of Geological Societies Transactions*, 17, 105-125.

Galloway, W.E., T.L. Whiteaker, and P. Ganey-Curry, 2011, History of Cenozoic North American drainage basin evolution, sediment yield, and accumulation in the Gulf of Mexico basin: *Geosphere*, 7(4), 938-973.

Hampson, D.P., B.H. Russell, and B. Bankhead, 2005, Simultaneous inversion of pre-stack seismic data: *SEG Technical Program Expanded Abstracts*, 1633-1637.

Han, D.H., A. Nur, and D. Morgan, 1986, Effects of porosity and clay content on wave velocities in sandstones: *Geophysics*, 51(11), 2093-2107.

Hargis, R.N., 2009, Major transgressive shales of the Wilcox, northern portion of south Texas: *South Texas Geological Society Bulletin*, 49(8), 19-47.

Krief, M., J. Garat, J. Stellingwerff, and J. Ventre, 1990, A petrophysical interpretation using the velocities of P and S waves (full-waveform sonic): *The Log Analyst*, 31(06).

Olariu, M.I., and H. Zeng, 2017, Prograding muddy shelves in the Paleogene Wilcox deltas, south Texas Gulf Coast: *Marine and Petroleum Geology*, 91, 71-88.

Schenewerk, P., D. Goddard, and J. Echols, 1994, Reservoir characterization and preliminary modeling of deltaic facies, lower Wilcox, Concordia Parish, Louisiana: *Gulf Coast Association of Geological Societies Transactions*, 44, 663-674.

Sharman, G.R., J.A. Covault, D.F. Stockli, A.F.J. Wroblewski, and M.A. Bush, 2017, Early Cenozoic drainage reorganization of the United States Western Interior–Gulf of Mexico sediment routing system: *Geology*, 45(2), 187-190.

Warwick, P.D., 2017, Geologic assessment of undiscovered conventional oil and gas resources in the lower Paleogene Midway and Wilcox groups, and the Carrizo sand of the Claiborne group, of the northern Gulf Coast region: *U.S. Geological Survey Open-File Report*, 2017-1111, 67p.

Zeng, H., W.A. Ambrose, and Wu. Xu, 2016, Sediment dispersal patterns of the outer shelf to upper slope Paleocene-Eocene Wilcox Group, South-Central Texas coast: *Gulf Coast Association of Geological Societies Transactions*, 5, 215-237.

IV. PRE-STACK SIMULTANEOUS INVERSION FOR DELINEATION OF THE LOWER WILCOX EROSIONAL REMNANT SANDSTONE BENEATH THE TEXAS GULF COASTAL PLAIN

Tianze Zhang*, Yani Lin, Kelly H. Liu, and Stephen S. Gao,

Geology and Geophysics Program, Missouri University of Science and Technology

ABSTRACT

The Lower Wilcox lowstand sand deposits encased between two sequence boundaries are of good reservoir quality and usually gas productive. However, the sedimentation is sparsely scattered within such depositional environment and it is hard to predict by qualitative interpretation methods. Simultaneous inversion of elastic parameters such as P-impedance, S-impedance, and density by the integration of pre-stack data and well logs allows us to quantitatively characterize the reservoirs, and to distinguish them from the surrounding rocks. In this study, we use pre-stack simultaneous inversion of the elastic parameters for delineation of the gas reservoir in an active field with limited log availabilities. For wells that are missing sonic and density logs, we estimate the parameters using the time average equation and Gardner's equation, respectively. The shear wave velocity estimation methods are tested and compared using measured log value. The estimation results are verified using well log correlations in adjacent wells. Rock physics analyses on wells are conducted to find the optimal elastic parameters for characterizing the gas bearing sand. We successfully delineate the reservoir using the crossplot of Vp/Vs versus S-Impedance values. The inversion results

are quality controlled by a producing well in the reservoir zone, and probability maps of each lithology are calculated by the probability density function. Our results from the Lower Wilcox Formation indicate that simultaneous inversion based on the estimated parameters using the time average equation is feasible, and the gas bearing reservoirs can be recommended in high confidence.

1. INTRODUCTION

The late Paleocene Lower Wilcox group is part of the thick sandstone/shale Wilcox sequence along the Texas Gulf Coast (Debout et al., 1982). It is mainly characterized as fluvial and deltaic deposits prograde over the mid-Cretaceous carbonate shelf margin with a high sedimentation rate (Winker, 1982; Galloway et al., 2011; Olariu and Zeng, 2017). The prograding Rockdale depositional system and abundant source supply provide favorable environments for hydrocarbon generation and preservation (Fisher and McGowen, 1969; Mackey et al., 2012; Zeng et al., 2016) (Figure 1).

The submarine canyon associated with the continental margin failure initiated with retrogressive slumping of delta front deposits and ended with backfilling (Galloway et al., 1991). During the evolution of the canyon, sidewall slumps and sediments brought by the hyperpycnal process formed the diverse depositional facies in the canyon fill. Among all, the lower canyon sandstone facies associated with slumps and turbidites covered with backfilling mudstone are usually productive, but hard to predict without high-resolution 3D seismic data (Galloway and McGilvery, 1995).

Various seismic interpretation techniques have been extensively used in the Texas Gulf Coast area for stratigraphy and depositional system studies (Fisher and McGowen, 1969; Debout et al., 1982; Hargis, 1986; Galloway et al., 2000; Hargis, 2009; Olariu and Ambrose, 2016; Zeng et al., 2016; Olariu and Zeng, 2017) and structural and seismic facies analyses (McDonnell et al., 2008; Allen and Howell, 1987; Egedahl et al., 2012; Enomoto, 2014). Most of the results are based on post-stack seismic attribute analyses, and the low confidence level of the results can hardly make them accurately tracing the target with high confidence. Only a few studies seeking to apply quantitative interpretation methods based on rock physics analysis and seismic inversion (Wagner et al., 2012). Possible reasons for the limited application of quantitative interpretation methods include: 1) pre-stack data acquisition is not profitable, 2) facies and structure are usually estimated through well log analysis, and 3) insufficient log availability impedes the use of a more accurate quantitative method such as pre-stack seismic inversion.

The simultaneous inversion process applied in this study inverts the pre-stack seismic data into different elastic volumes and reduce the interpretation ambiguity caused by solely inverting for the P-Impedance volume (Hampson et al., 2005; Russell and Hampson, 2006). By quantifying the properties of the reservoir using well log analysis, we can delineate and quantify the risk of the gas bearing sandstone area with high confidence. A successful inversion process requires a comprehensive set of log types, especially the density and velocity information for accurate seismic-to-well correlation and elastic parameter calculation. However, those logs are not always available, hence wisely choosing and verifying the log estimation method is crucial for the inversion results.

This study focuses on the inter-channel erosional remnant sand reservoir within the canyon fill. The objective is to test the log estimation method in the Lower Wilcox Formation, and to explore the feasibility of accurately performing the pre-stack inversion method in the reservoir field that lacks essential velocity and density information. We use a dataset acquired from an active field that contains a 3D seismic survey and well logs. For wells missing P-wave velocity and density, we estimate these values using the time average equation and lithology specific Gardner's equation, respectively. The estimation results are tested and verified on two testing wells before applying the method to other wells for the inversion. A clear separation of pay sand section from the background trend is observed in the well log analysis, and the result is used to quantify the properties of the reservoir and later describe the reservoir extent using the inverted results. The accuracy of the results is examined by a producing well drilled in the field. Besides, the probability density function allows us to calculate the probability for each lithology and quantify the risk of the predicted area. The promising results from this study suggest that the same workflow and method can be applied to the similar regions in the Lower Wilcox Formation.

2. DATA AND METHOD

Seismic and well data: A 3D pre-stack seismic data set that covers an area of 9.3 square miles and logs from eight wells are used in the inversion process (Figure 2). The seismic survey contains 166 inlines and 261 crosslines with offset ranging from 1000 ft to 19000 ft. The main frequency ranges from 10 Hz to 40 Hz, with a dominant frequency of

about 28 Hz. Pre-conditioning of the pre-stack seismic data is essential to obtain reliable inversion results (Zhang et al., 2015), thus the dataset is processed by normal moveout procedure, and muted to increase the signal-to-noise ratio by reducing the noise from distant CDP gathers.

Six of the eight wells are located within the survey area. Two producing wells (Well-3 and Well-4) that penetrate the same pay sand interval with over 80 ft thickness are used for the rock physics and inversion analyses of the sandstone reservoir. Three dry wells (Well-1, Well-2, and Well-6) provide constraints on the inversion process, and the other producing well (Well-5) is used to test the accuracy of the results. The log type for wells within the seismic survey is limited, only gamma ray, spontaneous, resistivity, and conductivity logs are available (Figure 3). The essential logs for the inversion process are density, sonic, and shear wave velocity logs. Although there are numerous empirical equations that describe the relations between resistivity, velocity, and density, choosing inappropriate relations can significantly affect the credibility of the inversion results. In this study, the performance of the density and velocity estimation method is tested using two wells (T-1 and T-2) that are located adjacent to the seismic survey.

Key log estimation: Sonic and density logs are the most crucial data for seismic-to-well tie and pre-stack inversion. Since both logs are missing from the wells within the seismic area, the study estimates the P-wave velocity from resistivity logs first, then calculates the density log from the velocity estimation.

Empirical equation such as Faust's equation describes the relationship between the P-wave velocity and resistivity, but the estimation results are usually unstable and cannot be applied in areas with different lithology conditions such as the Lower Wilcox

Formation which is dominantly composed of sandstone and mudstone. This study uses the time average equation (TAE) to estimate the sonic log from resistivity log. The TAE takes the lithology difference and formation porosity into account, and quantifies its effectiveness in comparison with other empirical equations (Adcock, 1993). The TAE for the two-lithology matrix form is given by

$$\Delta T = \Delta T_F f_R + [\Delta T_{sh} f_{sh} + \Delta T_{sd}(1 - f_{sh})](1 - f_R), \quad (1)$$

where ΔT_F, ΔT_{sh}, and ΔT_{sd} are the sonic travel time for fluid, shale, and sand, respectively. The fractional shale volume (f_{sh}) is calculated by the gamma ray log. The fractional porosity (f_R) is calculated by Archie's equation which assumes that the sand is fully saturated with water, using

$$f_R = (aRw/{S_w}^n Rt)^{1/m}, \quad (2)$$

where the constants a, n, and m are 0.81, 2, and 1, respectively. The R_w values are estimated from the mud filtrate and drill mud resistivity that acquired from log heading. The R_w for the two producing wells is 0.035 Ω-m for Well-3 and 0.03 Ω-m for Well-4. The water saturation values for the gas bearing zone need to be adjusted separately. The gamma ray and resistivity logs are normalized before calculating the shale volume and porosity to reduce the error caused by the logging devices or measurements.

Lithology specific Gardner's equations for both sandstone and shale are then used for the bulk density estimation, which are given by

$f_{sh}<0.25$: $\rho_b = -0.0115{V_P}^2 + 0.261V_P + 1.515$ (3)

$f_{sh}>0.25$: $\rho_b = -0.0261{V_P}^2 + 0.373V_P + 1.458$ (4)

The P-wave velocity and density estimation methods are tested in Well T-1 before being applied to the other wells for inversion. The velocity and density values calculated

by the TAE and Gardner's equation are compared with the measured values, and the P-wave estimation results by Faust's equation are also compared with results from the TAE (Figure 4a). The results suggest that both missing parameters are accurately estimated, and the performance of the TAE is better than Faust's equation with significantly fewer errors. The equations with identical parameters are applied to another testing Well T-2 for quality control (Figure 4b). The results demonstrate the errors in P-wave estimation by Faust's equation are greatly reduced by the TAE, and the errors in density estimation by Gardner's equation are also in a tolerable range. The seismic-to-well tie process is one of the key steps in the interpretation workflow, and it cannot be achieved without knowing the time-depth correlation that is provided by either check shot data or P-wave velocity. The tying process for the testing wells are conducted by both original logs and estimated logs, and the correlation quality can be visually checked by matching the synthetic seismogram with the extracted seismic trace. The computed seismogram using the estimated logs matches majority part of the seismic trace with similar amplitude and peak/trough waveform pattern (Figure 5). The slight reduction in correlation coefficients is caused by the dissimilarity of amplitude in a few locations. The overall good correlations in test wells indicate high accuracy in the estimation, and the methods are qualified to apply in the wells for inversion.

After calculating the sonic and density logs, seismic-to-well tie is conducted for all the wells to match the well log information to the seismic, guided by the interpreted horizons (Figure 6). The correlation coefficient is 0.419 for Well-3 and 0.436 for Well-4. The values are acceptable considering that the wells containing both logs only have correlation coefficients ranging from 0.5 to 0.6 in the field. The good match in waveform

patterns and amplitude between synthetic seismogram and seismic trace represents a good estimation on density and velocity logs for the Lower Wilcox Formation.

The shear wave velocity (V_S) is another key component in seismic inversion. We test and compare various Vs estimation methods in Well T-2, which is the only well that contains shear wave measurements. The water saturated Vp-Vs relation based on clay content (Han et al., 1986) is given by

$$f_{sh}<0.25: V_S = 0.754V_P - 0.657 \quad (5)$$

$$f_{sh}>0.25: V_S = 0.842V_P - 1.099 \quad (6)$$

For the gas saturated zone, we applied Krief's equation (Krief et al., 1990), which is given by

$$V_S = \sqrt{\frac{{V_P}^2 - 0.902}{2.282}} \quad (7)$$

Rock physics analysis: Rock physics analysis is performed on wells to find the optimal elastic parameters to characterize the reservoir. For this purpose, we crossplot the S-Impedance with Vp/Vs ratio in the Lower Wilcox Formation to characterize the reservoir (Figure 7a). The analysis from data points from five wells shows a distinct separation between two clusters of data, a cluster on the left side with low Vp/Vs ratio and slightly higher S-impedance value, and a cluster showing the background trend of the rest data. The left cluster is equivalent to the pay sand sections in Well-3 and Well-4 (Figure 7b). The pay sand has Vp/Vs values from 1.55-1.65 and S-impedance values from 12500-21500. The crossplot shows that both parameters should be used to characterize the reservoir, while using a single parameter can cause ambiguity in the inversion results.

Pre-stack simultaneous inversion: The pre-stack simultaneous inversion method proposed by Hampson and Russell (2005) derives the elastic parameters from the pre-stack PP angle gathers. The method is based on Fatti's reformulation of the Zoeppritz's equation (Fatti et al., 1994), which is given by

$$T(\theta) = A_1 W(\theta) D L_P + A_2 W(\theta) D \Delta L_S + c_3 W(\theta) D \Delta L_D, \quad (8)$$

where

$$A_1 = \frac{1}{2}(1 + tan^2\theta) + \frac{1}{2}k(-8\left(\frac{V_S}{V_P}\right)^2 sin^2\theta) + m(2\left(\frac{V_S}{V_P}\right)^2 sin^2\theta - \frac{1}{2}tan^2\theta), \quad (9)$$

$$A_2 = \frac{1}{2}(-8\left(\frac{V_S}{V_P}\right)^2 sin^2\theta), \quad (10)$$

$$W(\theta) = wavelets\ dependent\ on\ incident\ angle\ \theta, \quad (11)$$

$$L_P = \ln(Z_P) \quad (12)$$

$$Z_P = P - Impedance \quad (13)$$

The variables k, m, ΔL_S, and ΔL_D can be calculated from the linear relation, given by

$$\ln(Z_P) = k \ln(Z_P) + k_c + \Delta L_S \quad (14)$$

$$\ln(Z_S) = m \ln(Z_S) + m_c + \Delta L_D \quad (15)$$

The inversion process needs a set of angle gathered trace, and a group of wavelets varied in incident angles as inputs. We convert the conditioned pre-stack data to angle gather that ranges from 1 to 40°. Two angle-dependent wavelets are statistically extracted from the angle gather volume, one has an angle ranging from 1-20°, and the other from 21-40° (Figure 8).

Another essential input for the inversion process is the low-frequency geological model, which compensates the low-frequency component that is absent in the bandlimited seismic data. The model is built with density and computed impedance of log data, and acts as an initial input to constrain the inversion process. The sections between wells are interpolated laterally and guided by the interpreted horizons. In this study, the model consists of computed Zp, Zs, and density logs of five wells, and eight horizons traced along the layers (Figure 9).

3. RESULTS AND INTERPRETATION

Inversion and analyses**:** To ensure quality, it is critical to conduct analyses for the inversion results from real data before applying the inversion method to the whole volume. The inverted elastic parameters match well with the computed log values (Figure 10). Both Well-3 and Well-4 show a good correlation between the inverted and original logs, especially for the pay sand zone, where Vp/Vs and S-Impedance show distinct values from the surrounding layers.

The simultaneous inversion algorithm is applied to the entire data volume, as shown along the arbitrary profile A-A’ crossing all six wells (Figure 11). The reservoir area is bounded by Well-2 in the north and Well-6 in the south. Both S-Impedance and Vp/Vs attributes show significant anomalies, while the P-Impedance attribute shows normal values. The significantly high S-Impedance and low Vp/Vs represent a possible gas saturated zone, but the exact extent of the area cannot be determined with confidence

because similar anomalies can also be observed in both up and down dipping regions as marked by arrows (Figures 11b and 11c).

To map the reservoir area, we crossplot the inverted Vp/Vs volume versus the inverted S-Impedance volume (Figure 12), similar to the rock physics analysis conducted on wells. The volume data show no distinctive cluster of gas sand and background trend. An area is selected using the range obtained from the analysis near wells (Figure 7), where Vp/Vs ranges from 1.5 to 1.65 and S-Impedance ranges from 16000 to 21500 (Figure 12). The cross-section provides better isolation for the sand body than individual parameters. Among all five wells used for the inversion, the production wells, Well-3 and Well-4, are drilled at the predicted reservoir location from the inversion, and the rest are outside of the area (Figure 13). The base of the lowest sequence boundary (BLES) is traced along the incised canyon beneath the gas bearing sand body (Figure 13). The structure of the canyon shows a general dipping direction from NW to SE, and the mass transported by the distributary channels feeds the lower section with sandy turbidites. The sandstone reservoir was transported from the updip region through the steep canyon wall, and then trapped at the canyon floor (Figure 13).

The main reservoir body and an elongated area in the northeast are analyzed in details (Figure 14). Thickness of the pay sand decreases from Well-3 to Well-5, which is consistent with their production rates (Figure 14a). The possible reservoir area dipping from northwest to southeast as shown in the time structure map, following the same direction of the mass wasting inside the canyon system (Figure 14b).

Producing well, Well-5, is used for testing the accuracy of the inversion result (Figure 15). The traces from each inverted attribute volume are extracted from the well

location and overlapped with the computed logs. The error is calculated by subtracting the inverted values from the computed ones. The error analysis results suggest that the parameters of the simultaneous inversion are reliable and can be used for reservoir characterization with confidence. The reservoir area which is represented by high S-Impedance and low Vp/Vs correlates well with the pay sand zone in Well-5, confirming the reliability of the inversion results (Figure 15).

Lithology classification: As shown in Figure 12, no distinction of the gas sand cluster is observed in the crossplot of the inverted attributes, which indicates that errors may exist when picking the cross section using the parameter from the well analysis. The bayesian kernel density estimation is utilized to calculate the probability density for each lithology class to reduce such error. We classify the lithology into gas sand, wet sand, and shale based on the criteria of resistivity and shale volume, and calculate the density distribution of each class in Vp/Vs and S-Impedance for the five wells (Figure 16). The contours in different colors stand for the probability distribution of each class. The probability gradually decreases towards the outside of the circle.

The density function is then applied to the entire data volume, and each class with a probability higher than 50% is displayed (Figure 17). The possible gas saturated area is highlighted with the probability higher than 90% (Figure 17a). The water saturated zones around Well-1 and adjacent to Well-6 correspond to the zone observed from the inverted elastic attributes volume (Figure 11), which shows the similar anomalous values caused by the reservoir.

The extracted the gas sand volume is compared with the cross section picked from well analysis (Figures 13 and 18). The majority of the area are overlapped with a

probability higher than 90%. This demonstrates the high accuracy of the inversion results, and the other potential gas prospective can be identified with high confidence. The elongated region on the northeast of the main body would be a highly recommended area for future exploration, which has moderate thickness and the same dipping direction as the main body.

Importance of simultaneous inversion: The major characteristic of the inter-channel sandstone reservoir in the study area is isolation. As a result, the extent of the reservoir is limited even a tight well placement can miss the prospect (e.g., Well-2 and Well-6). Accurate quantitative seismic analysis using multiple elastic parameters is necessary to predict the distribution and geometry of the reservoir. As indicated in this study, both Well-1 and Well-6 were drilled at areas with similar P-Impedance, S-Impedance, and Vp/Vs values to the reservoir in both updip and downdip regions (Figure 11), which are correlated to the water saturated sandstones from the inversion parameters (Figure 17b). Determination of the location of a prospective reservoir can be misled in traditional acoustic inversion, while the pre-stack simultaneous inversion of various elastic attributes can provide additional constraints to the results in hydrocarbon exploration and lithology classification.

4. CONCLUSIONS

This study applies pre-stack seismic inversion using estimated velocity and density logs to an active field beneath the Texas Gulf Coastal Plain which focuses on the Lower Wilcox gas bearing sand formation. The analyses indicate that the time average

equation can provide a better estimation on velocity than empirical Faust's equation in the Lower Wilcox Formation. The calculated velocity is used to estimate the density by Gardner's equation, and to accurately conduct seismic-to-well tie process. The simultaneous inversion results using estimated values are accurate and the quality is tested by a producing well. Based on the probability density function, the probability of each lithology is calculated with high confidence. The reservoir area is delineated and the morphology is indicated by the inverted volumes. The study suggests that the estimated velocity and density using time average equation and Gardener's equation are accurate for the Lower Wilcox Formation, and the seismic inversion results based on the estimated parameters are reliable. The same workflow and approach can be applied to the field similar to the Lower Wilcox Formation for hydrocarbon exploration and depositional facies recognition and delineation.

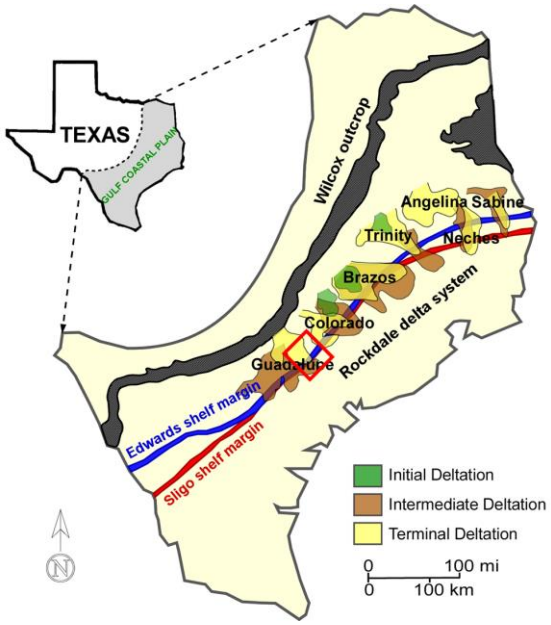

Figure 1. Location of the Texas Gulf Coast (Modified from Olariu & Zeng, 2017). The study area is indicated by the red rectangle.

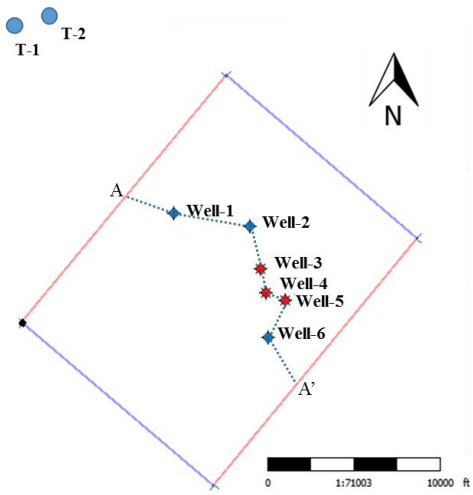

Figure 2. Basemap showing seismic and well locations. The dashed blue line displays the location of the arbitrary line A-A'.

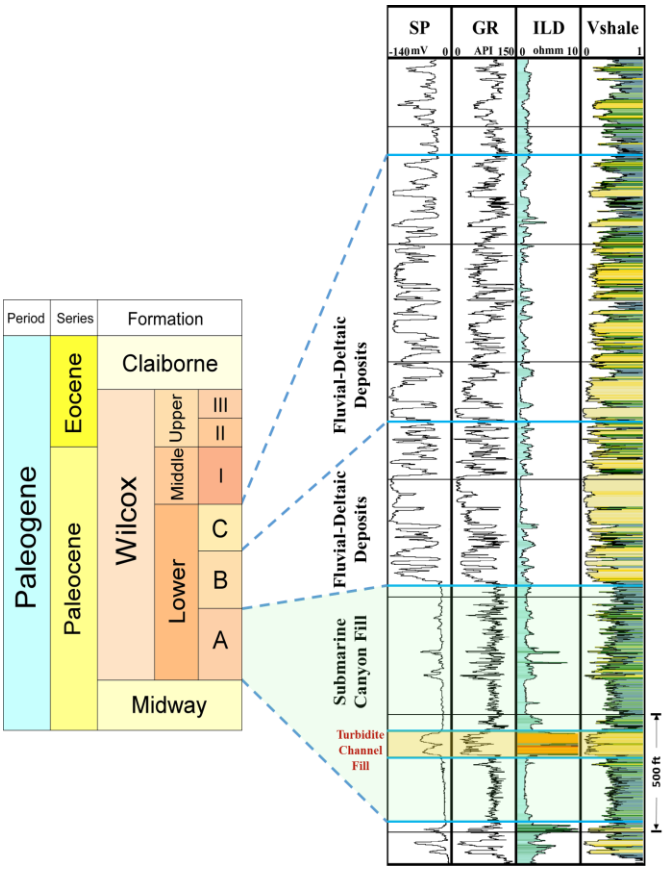

Figure 3. The stratigraphy of the Lower Wilcox Formation and well logs of Well-3.

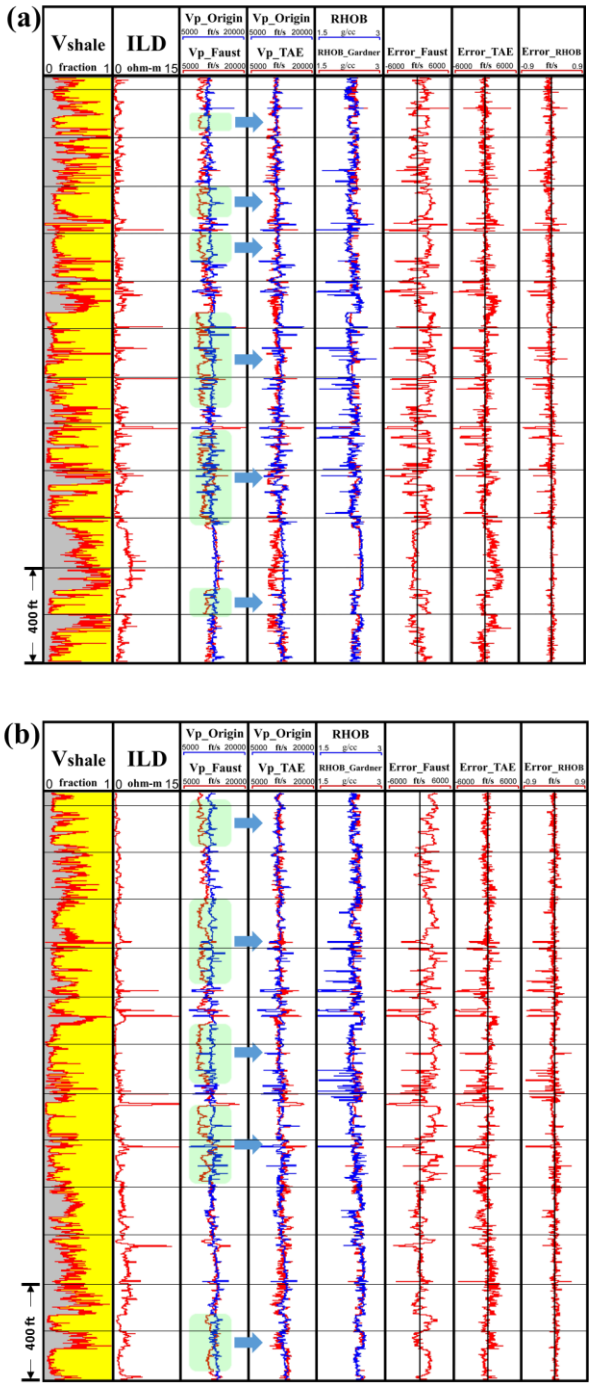

Figure 4. Example logs used in the velocity and density estimation, and the comparison between the estimated (blue) and calculated logs (red). Cyan areas show significant errors caused by Faust's estimation, arrows point at better results. The errors are calculated by subtracting the calculated logs from the original logs. (a) Well T-1. (b) Well T-2. (Cont.)

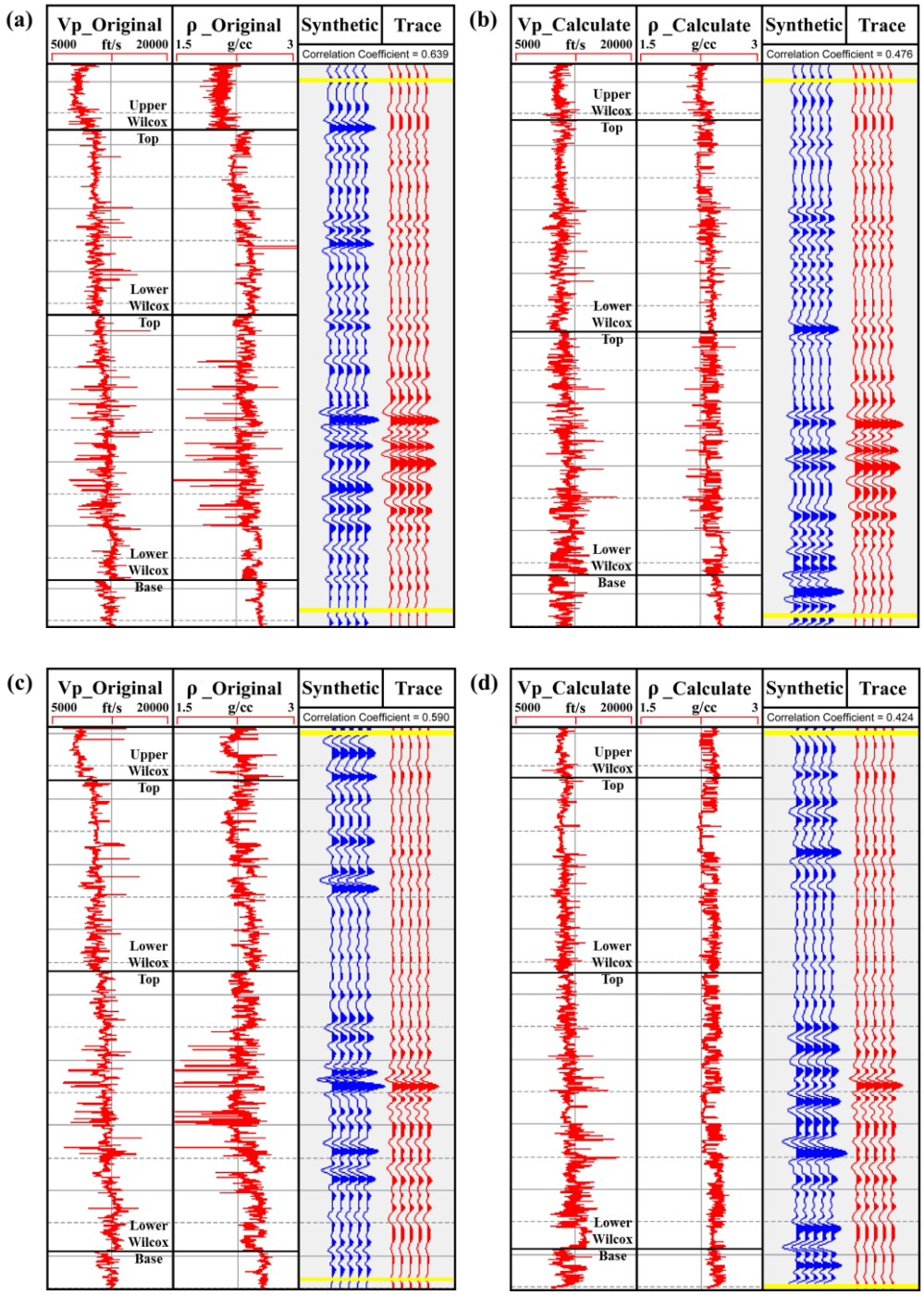

Figure 5. A comparison of seismic-to-well tie in Well T-1 and Well T-2. Yellow lines represent boundaries used to calculate the correlation coefficients. (a) Well T-1 with original velocity and density. (b) Well T-1 with estimated velocity and density. (c) Well T-2 with original velocity and density. (d) Well T-2 with estimated velocity and density.

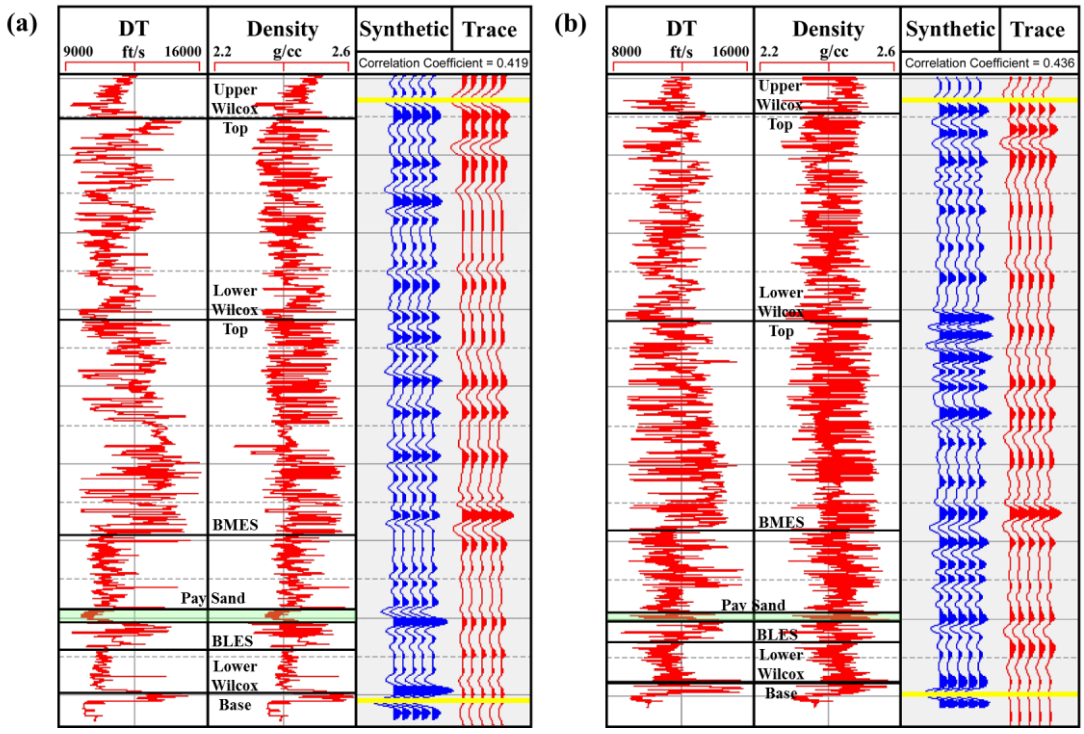

Figure 6. Log correlation results of Well-3 and Well-4 using estimated velocity and density logs. BMES: base of the middle erosional sequence. BLES: base of the lower erosional sequence. (a) Well-3. (b) Well-4.

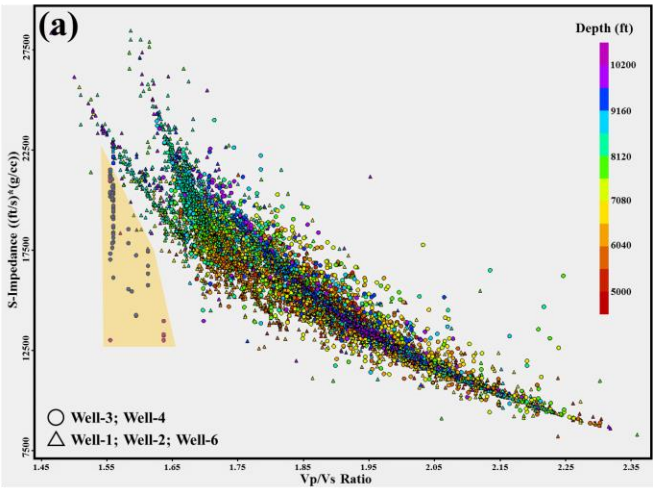

Figure 7. (a) Results of rock physics analysis. The area colored with yellow is equivalent to the colored sections in (b), which represents the pay sand location. (b) Cross section for each of the five wells.

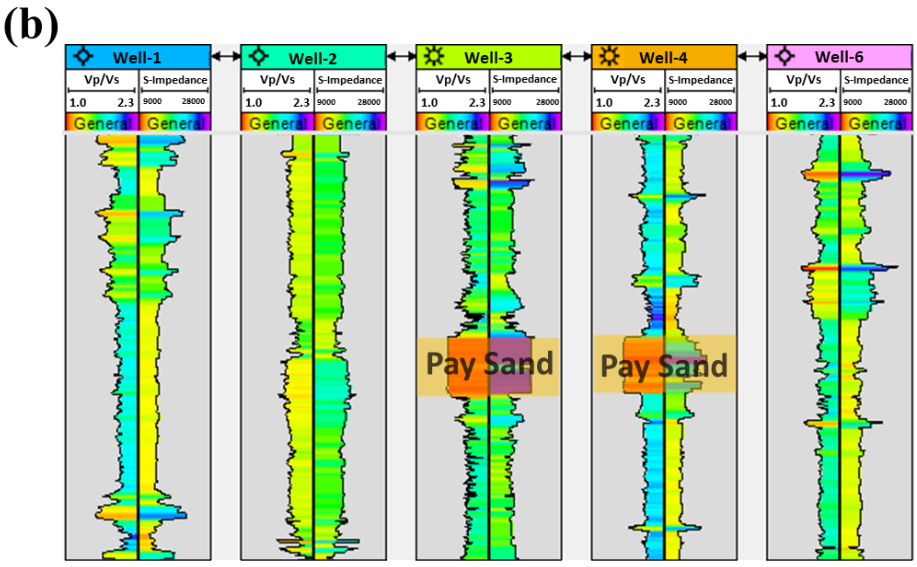

Figure 7. (a) Results of rock physics analysis. The area colored with yellow is equivalent to the colored sections in (b), which represents the pay sand location. (b) Cross section for each of the five wells. (Cont.)

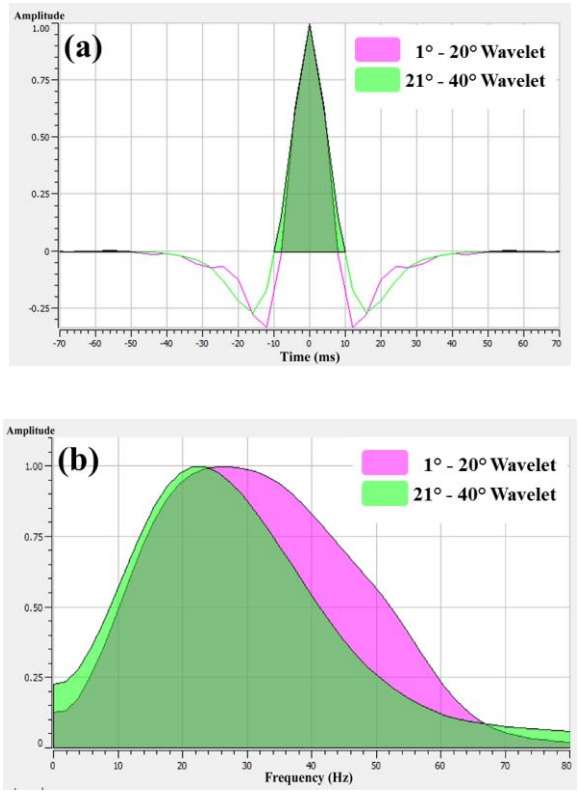

Figure 8. Wavelets extracted from the pre-stack angle-gather volume. Angle ranges from 1 to 20° (pink), and 21 to 40° (green) in both time domain and frequency domain.

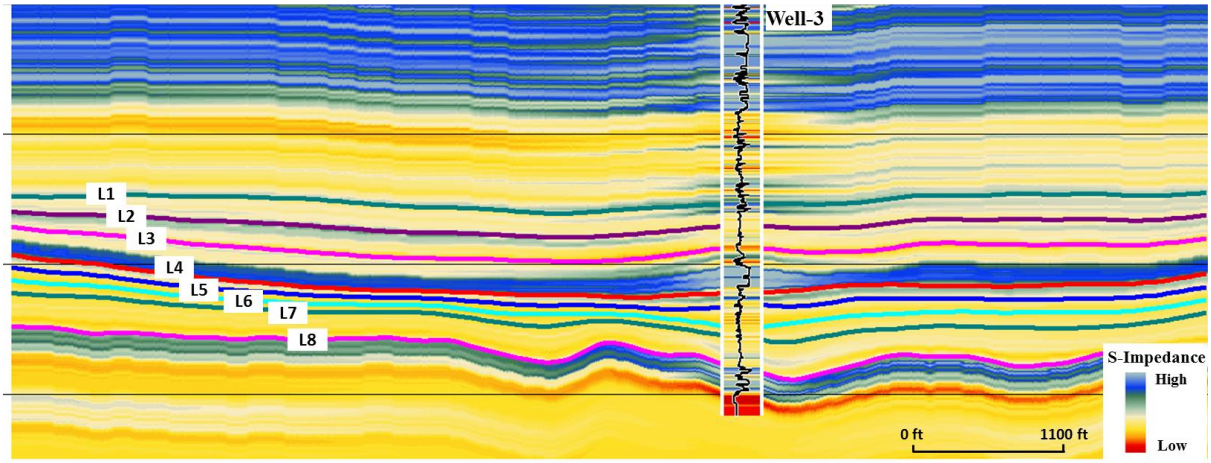

Figure 9. The S-Impedance model of a crossline intersecting Well-3. A high value of S-Impedance is observed at the pay sand layer between L3 and L4.

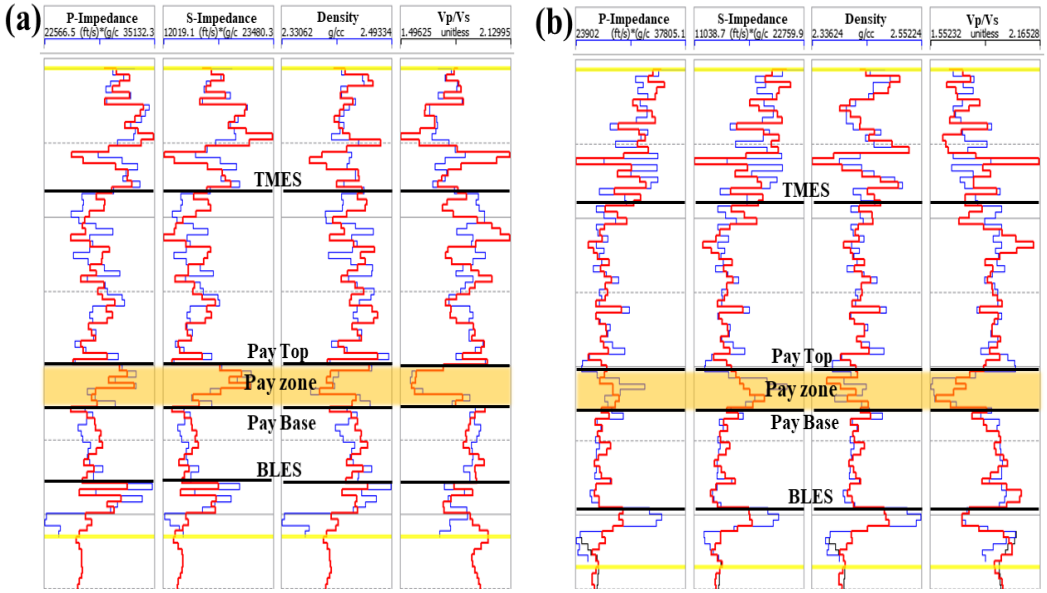

Figure 10. Inversion analyses for Well-3 and Well-4. Log panels from left to right are P-impedance, S-impedance, density, and Vp/Vs. Original logs are in blue, and inverted logs are in red. TMES : top of the middle erosional sequence. BLES: base of the lower erosional sequence. (a) Well-3. (b) Well-4.

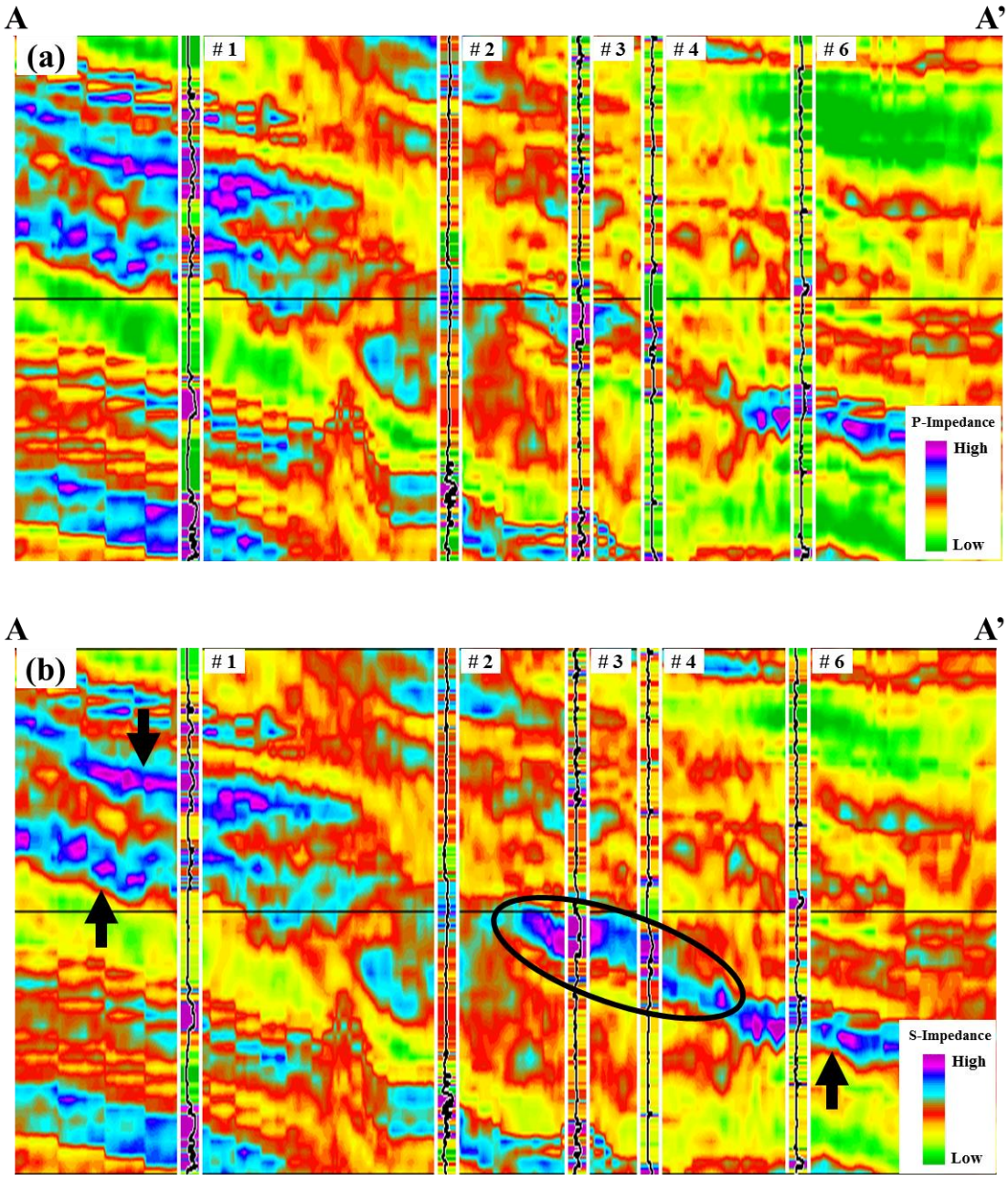

Figure 11. Inverted elastic attributes along profile A-A'. Circles indicate reservoir zone represented by low Vp/Vs and high S-Impedance value. Arrows mark the zone with similar anomalous values as the reservoir. (a) P-Impedance. (b) S-Impedance. (c) Vp/Vs.

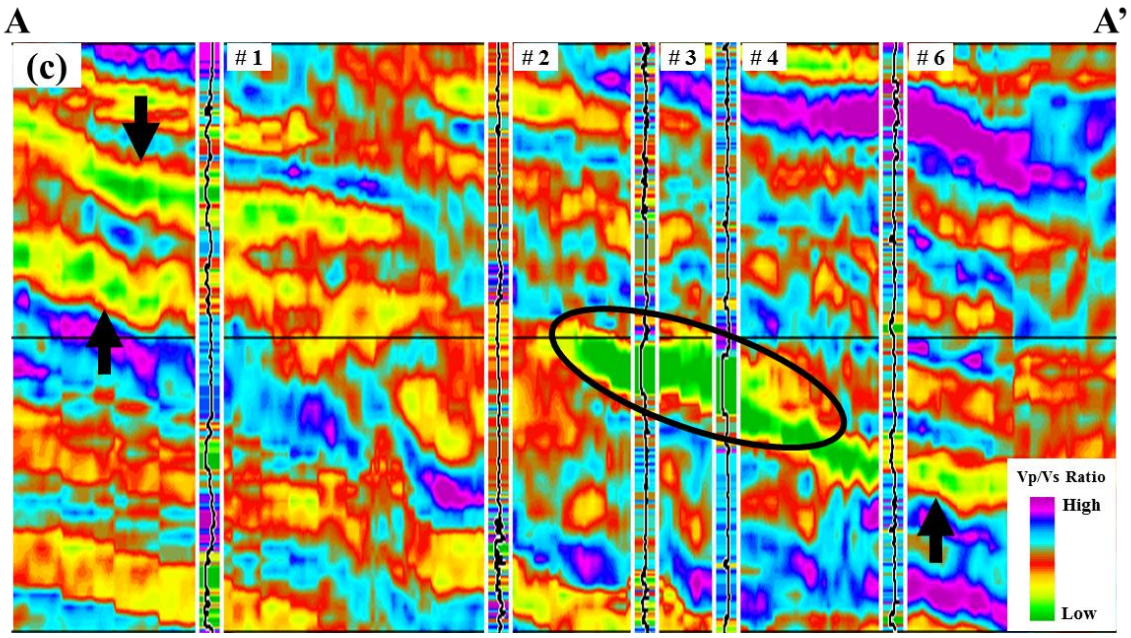

Figure 11. Inverted elastic attributes along profile A-A'. Circles indicate reservoir zone represented by low Vp/Vs and high S-Impedance value. Arrows mark the zone with similar anomalous values as the reservoir. (a) P-Impedance. (b) S-Impedance. (c) Vp/Vs. (Cont.)

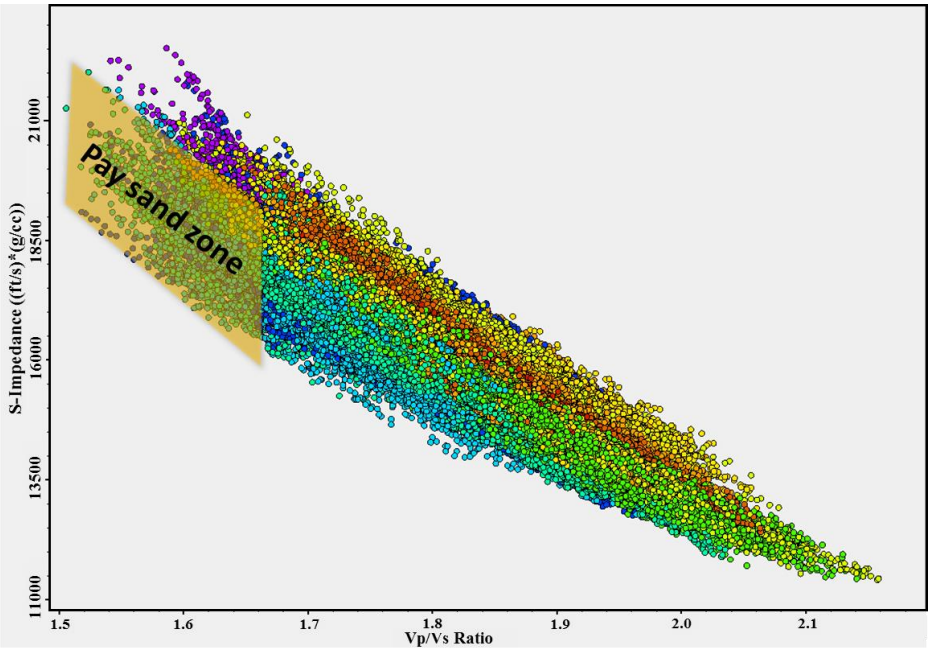

Figure 12. Inverted Vp/Vs versus inverted S-Impedance.

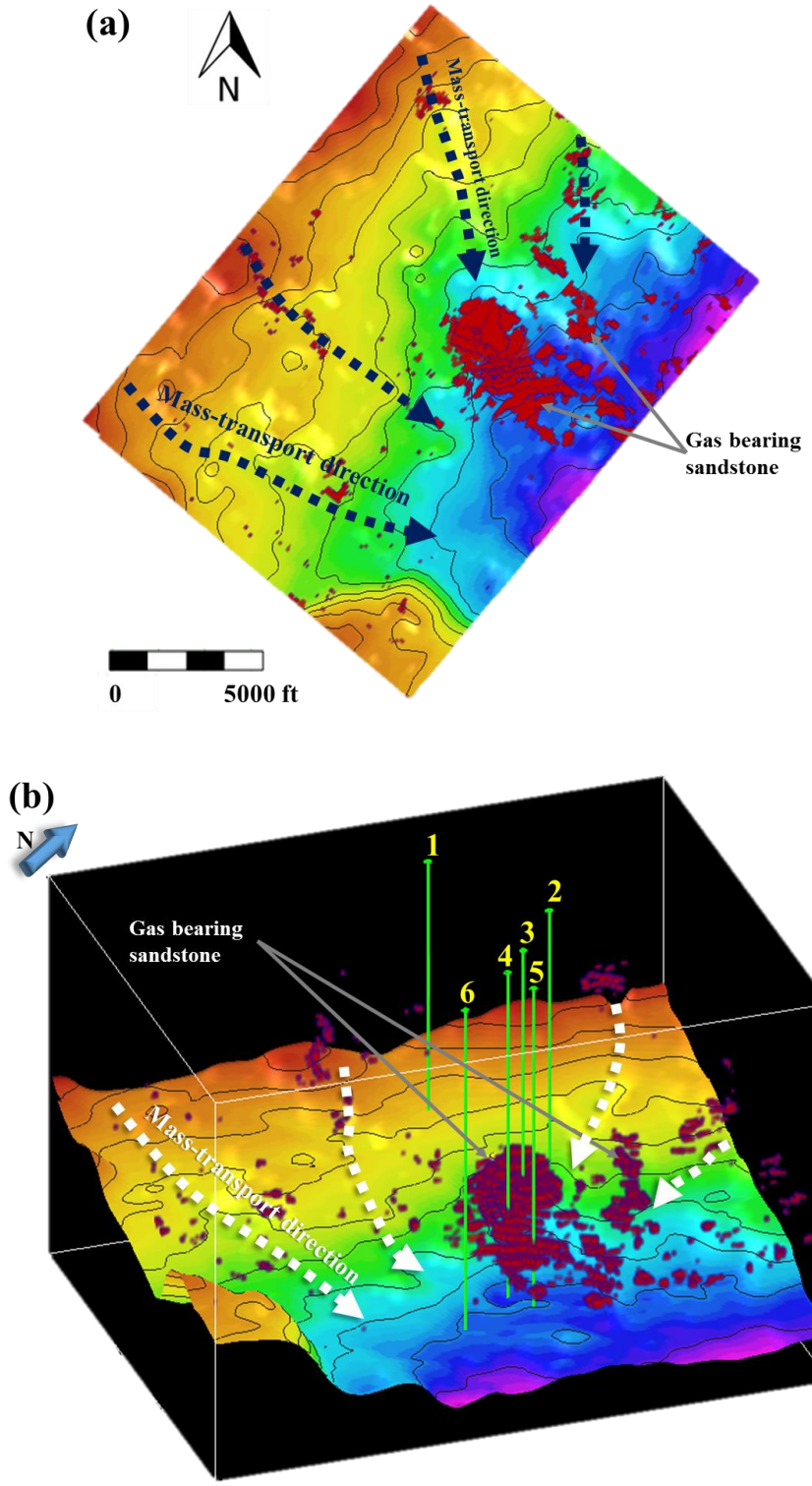

Figure 13. Inverted gas bearing sand and the incised canyon boundary. The dashed arrows represent the location of submarine distributary channels that transport the mass into the middle canyon area. (a) Plane view. (b) 3D view.

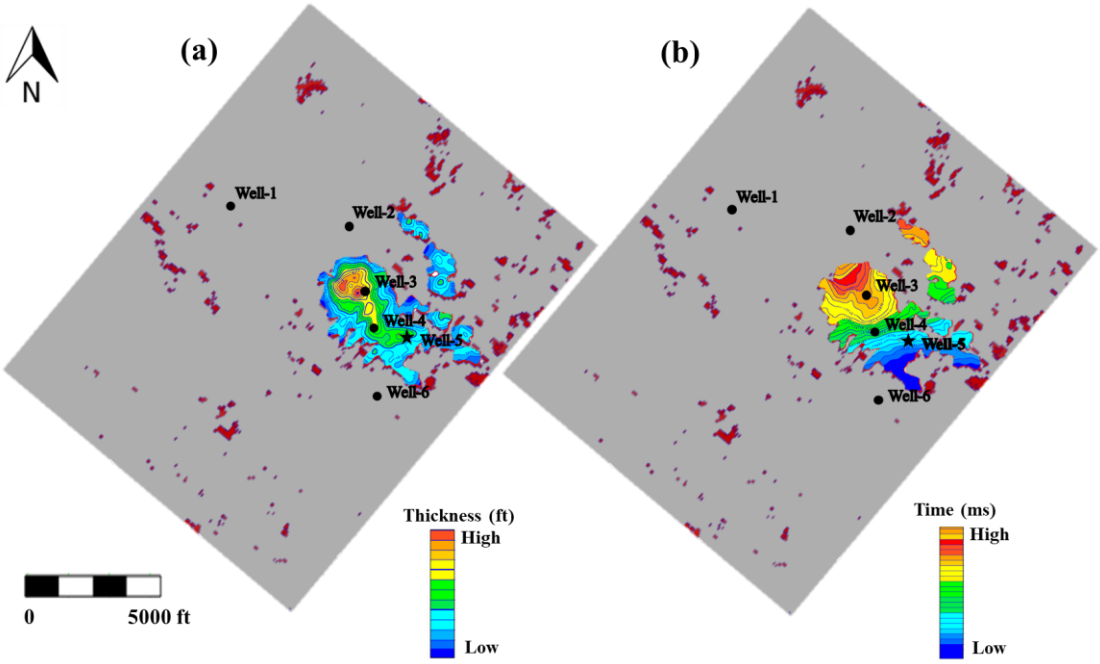

Figure 14. Plane view of the isolated pay sand area. (a) Isopach map. (b) Structure map.

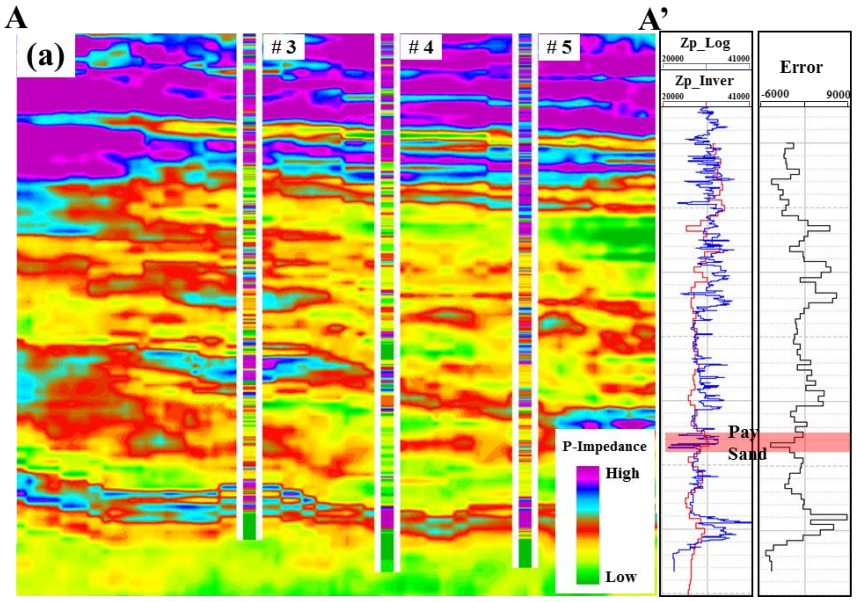

Figure 15. Inversion quality control with Well-5 along A-A', by overlapping the computed logs (blue) with the inverted values (red). (a) P-Impedance. (b) S-Impedance. (c) Vp/Vs ratio.

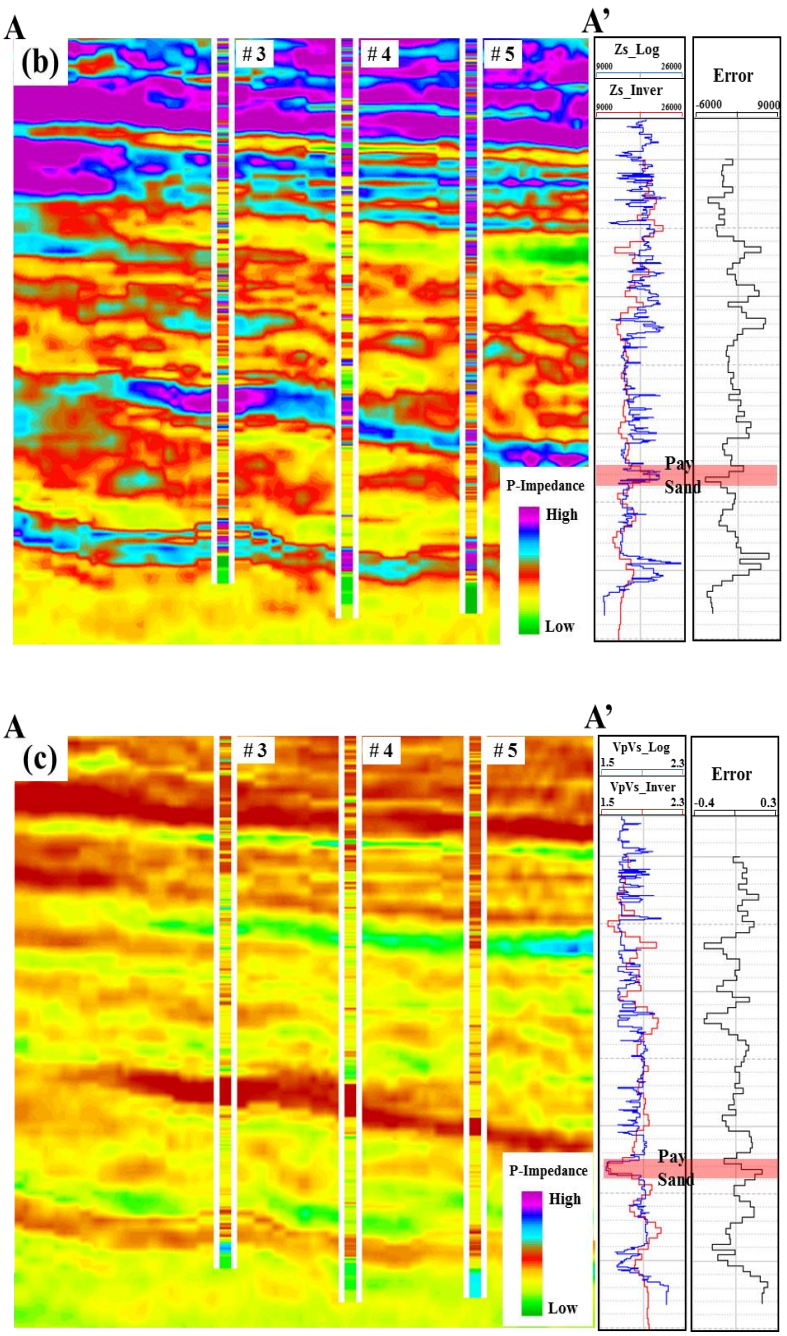

Figure 15. Inversion quality control with Well-5 along A-A', by overlapping the computed logs (blue) with the inverted values (red). (a) P-Impedance. (b) S-Impedance. (c) Vp/Vs ratio. (Cont.)

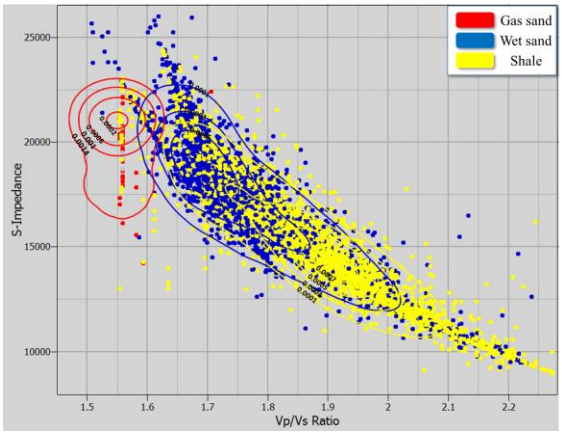

Figure 16. Density map of each lithology class calculated by kernel density estimation.

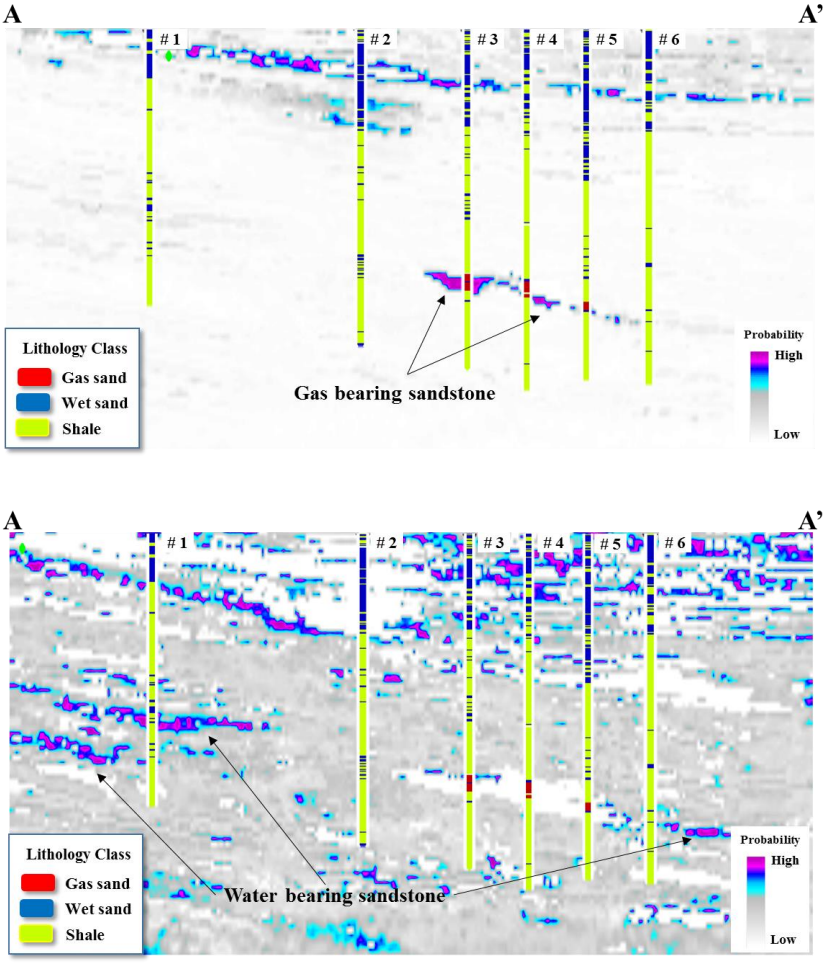

Figure 17. Probability map of each lithology class. (a) Gas sand. (b) Wet sand. (c) Shale.

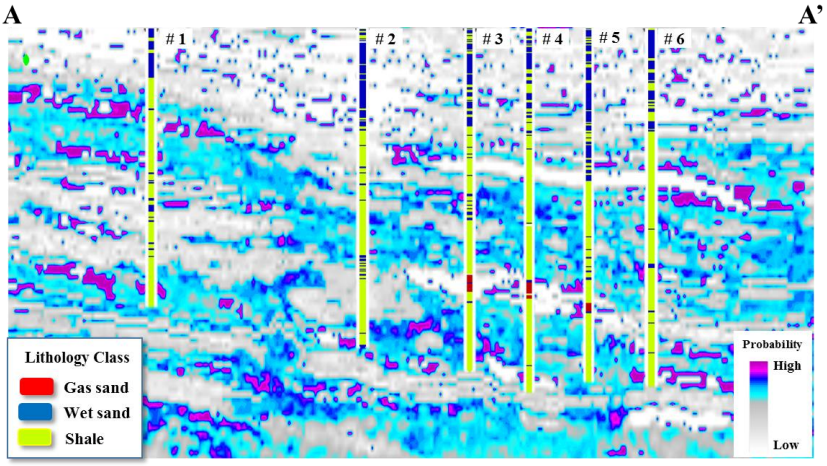

Figure 17. Probability map of each lithology class. (a) Gas sand. (b) Wet sand. (c) Shale. (Cont.)

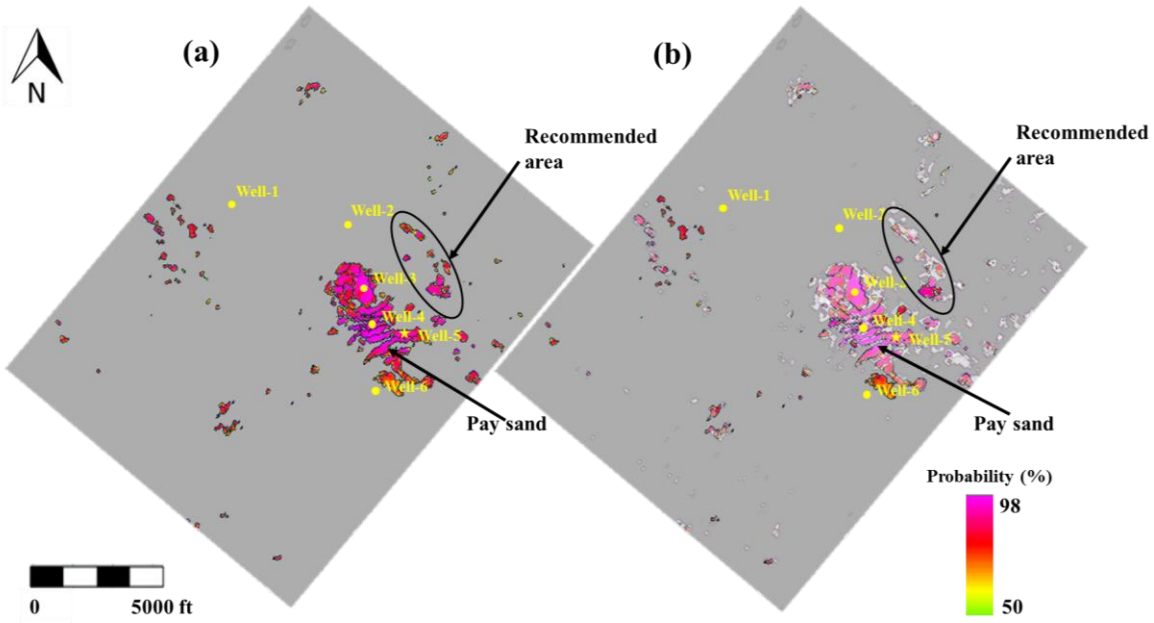

Figure 18. Top view of the gas sand probability map and comparison with the estimated result from Figure 12. (a) Gas sand probability. (b) Estimated sand body overlapped with probability.

ACKNOWLEDGMENTS

We are thankful to a generous company for donating the comprehensive dataset used in this study. We would also like to thank both CGG and IHS Markit for the generous donations of Hampson Russell and Kingdom software packages.

REFERENCES

Adcock, S., 1993, In search of the well tie: What if I don't have a sonic log?: *The Leading Edge*, 12(12), 1161-1164, doi: 10.1190/1.1436929.

Allen, J., and J. Howell Sr., 1987, Using "poor man's 3-D" to identify distributary channel sands in the Wilcox formation, Lavaca County, Texas: *The Leading Edge*, 6(10), 8-15, doi: 10.1190/1.1439339.

Debout, D.G., B.R. Weise, A.R. Gregory, and M.B. Edwards, 1982, Wilcox sandstone reservoirs in the deep subsurface along the Texas Gulf Coast: Their potential for production of geopressured geothermal energy: *Report of Investigations* No. 117 (No. DOE/ET/28461-T2), Texas Univ., Austin (USA), Bureau of Economic Geology, doi: 10.2172/6140725.

Egedahl, K., G.L. Kinsland, and D. Han, 2012, Seismic facies study of 3D seismic data, northern Louisiana, Wilcox Formation: *Gulf Coast Association of Geological Societies Transactions*, 62, 73-91.

Enomoto, C.B., 2014, Well log and 2D seismic data character of the Wilcox Group in South-Central Louisiana: *Gulf Coast Association of Geological Societies Transactions*, 64, 105-118.

Fatti, J.L., G.C. Smith, P.J. Vail, P.J. Strauss, and P.R. Levitt, 1994, Detection of gas in sandstone reservoirs using AVO analysis: A 3-D seismic case history using the Geostack technique: *Geophysics*, 59(9), 1362-1376, doi: 10.1190/1.1443695.

Fisher, W.L., and J.H. McGowen, 1969, Depositional systems in Wilcox Group (Eocene) of Texas and their relation to occurrence of oil and gas: *AAPG Bulletin*, 53(1), 30-54.

Galloway, W.E., W.F. Dingus, and R.E. Paige, 1991, Seismic and depositional facies of Paleocene-Eocene Wilcox Group submarine canyon fills, northwest Gulf Coast, USA: *Seismic Facies and Sedimentary Processes of Submarine Fans and Turbidite Systems*, 247-271, Springer, New York, NY.

Galloway, W.E., and T.A. Mcgilvery, 1995, Facies of a submarine canyon fill reservoir complex, lower Wilcox Group (Paleocene), central Texas coastal plain: *Turbidites and Associated Deep-Water Facies*, 20, 1-23.

Galloway, W.E., P.E. Ganey-Curry, X. Li, and R.T. Buffler, 2000, Cenozoic depositional history of the Gulf of Mexico basin: *AAPG Bulletin*, 84(11), 1743-1774, doi: 10.1306/8626C37F-173B-11D7-8645000102C1865D.

Galloway, W.E., T.L. Whiteaker, and P. Ganey-Curry, 2011, History of Cenozoic North American drainage basin evolution, sediment yield, and accumulation in the Gulf of Mexico basin: *Geosphere*, 7(4), 938-973, doi: 10.1130/GES00647.1.

Hampson, D.P., B.H. Russell, and B. Bankhead, 2005, Simultaneous inversion of pre-stack seismic data: *SEG Technical Program Expanded Abstracts*, 1633-1637, doi: 10.1190/1.2148008.

Han, D.H., A. Nur, and D. Morgan, 1986, Effects of porosity and clay content on wave velocities in sandstones: *Geophysics*, 51(11), 2093-2107, doi: 10.1190/1.1442062.

Hargis, R.N., 1986, Proposed stratigraphic classification of the Wilcox of South Texas: *Contributions to the Geology of South Texas*, 135-159.

Hargis, R.N., 2009, Major transgressive shales of the Wilcox, northern portion of south Texas: *South Texas Geological Society Bulletin*, 49(8), 19-47.

Krief, M., J. Garat, J. Stellingwerff, and J. Ventre, 1990, A petrophysical interpretation using the velocities of P and S waves (full-waveform sonic): *The Log Analyst*, 31(06).

Mackey, G.N., B.K. Horton, and K.L. Milliken, 2012, Provenance of the Paleocene–Eocene Wilcox Group, western Gulf of Mexico basin: Evidence for integrated drainage of the southern Laramide Rocky Mountains and Cordilleran arc: *GSA Bulletin*, 124(5-6), 1007-1024, doi: 10.1130/B30458.1.

McDonnell, A., R.G. Loucks, and W.E. Galloway, 2008, Paleocene to Eocene deep-water slope canyons, western Gulf of Mexico: Further insights for the provenance of deep-water offshore Wilcox Group plays: *AAPG Bulletin*, 92(9), 1169-1189, doi: 10.1306/05150808014.

Olariu, M.I., and W.A. Ambrose, 2016, Process regime variability across growth faults in the Paleogene Lower Wilcox Guadalupe Delta, South Texas Gulf Coast: *Sedimentary Geology*, 341, 27-49, doi: 10.1016/j.sedgeo.2016.05.013.

Olariu, M.I., and H. Zeng, 2017, Prograding muddy shelves in the Paleogene Wilcox deltas, south Texas Gulf Coast: *Marine and Petroleum Geology*, 91, 71-88, doi: 10.1016/j.marpetgeo.2017.12.027.

Russell, B., and D. Hampson, 2006, The old and the new in seismic inversion: *CSEG Recorder*, 31(10), 5-11.

Wagner, C., A. Gonzalez, V. Agarwal, A. Koesoemadinata, D. Ng, S. Trares, N. Biles, and K. Fisher, 2012, Quantitative application of poststack acoustic impedance inversion to subsalt reservoir development: *The Leading Edge*, 31(5), 528-537, doi: 10.1190/tle31050528.1.

Winker, C.D., 1982, Cenozoic shelf margins, Northwestern Gulf of Mexico: *Gulf Coast Association of Geological Societies Transactions*, 32, 427-448.

Zeng, H., W.A. Ambrose, and W. Xu, 2016, Sediment dispersal patterns of the outer shelf to upper slope Paleocene-Eocene Wilcox Group, South-Central Texas coast: *Gulf Coast Association of Geological Societies Transactions*, 5, 215-237.

Zhang, B., D. Chang, T. Lin, and K.J. Marfurt, 2014, Improving the quality of prestack inversion by prestack data conditioning: *Interpretation*, 3(1), T5-T12, doi: 10.1190/INT-2014-0124.1.

SECTION

2. CONCLUSIONS

In the Fault Image Enhancement project, our study using a complex 3D marine seismic data set indicates that the ant tracking technique is an outstanding tool in fault identification and interpretation. However, the reliability of the results is based on proper selection of signal processing methods and volume attributes. In the typical processing procedure, Automatic Gain Control and Structural Smoothing are sufficient to process the data and increase the signal to noise ratio. In our study area, the complex geological structure and various data quality require a more comprehensive signal processing technique to provide accurate fracture information. Graphic Equalizer by adjusting amplitudes of different frequencies appropriately can help us to achieve this goal. Our results show that in such geological conditions, the Chaos attribute performs well for edge detection, leading to clearer and detailed results than combining the Variance and Chaos attributes or the Variance attribute alone.

In the reservoir characterization project, the rock physics analyses results show that the transition zone from compaction to chemical cementation takes place around 2100 m depth for all wells, at temperatures ranging from 60°C-70°C, which is consistent with results from thermal gradient analyses. The porosity reduction in the Lower Wilcox Formation shows that poor sorting plays a more significant role than mineral precipitation. The irregular distribution pattern in Well-1 and Well-3 is possibly caused by the depositional environment that differs from the other wells.

The seismic inversion results show that for depth that is larger than 5000 ft, the time average equation can provide a robust estimation on velocity using the resistivity and Gamma-Ray log. The rock physics analyses from wells indicate that the sand reservoir has low Vp/Vs values ranging from 1.54 to 1.62 and a wide range of P-impedance values ranging from 23000 to 34000. The pay sand has a clear separation from the surround shales. P-impedance, S-impedance and Vp/Vs volume are generated through the pre-stack simultaneous inversion, and we observe a gas reservoir at 2100 ms with low Vp/Vs values encasing between the two erosional sequences. We crossplot the S-impedance and Vp/Vs from the inversion result and pick the similar area as the rock physics analyses from wells. The cross-section shows a better delineation of the reservoir, and reduces the ambiguity caused by the low Vp/Vs anomaly that observed in the shallow area from 1900 ms to 2000 ms. We use a blind well for the quality control of the results. The blind well locates inside the reservoir area, and the elastic logs correlate with the inverted volume accurately. The morphology of the inverted reservoir volume accords with the pattern of a low-stand deposit. Also, the gross production output of each producing well correlates with the reservoir thickness at each well location.

BIBLIOGRAPHY

Adcock, S., 1993, In search of the well tie: What if I don't have a sonic log?: *The Leading Edge*, 12(12), 1161-1164, doi: 10.1190/1.1436929.

Aki, K., and Richards, P.G., 1980, Quantitative seismology: *Theory and methods*, W.H. Freeman and Co.

Allen, J., and J. Howell Sr., 1987, Using "poor man's 3-D" to identify distributary channel sands in the Wilcox formation, Lavaca County, Texas: *The Leading Edge*, 6(10), 8-15, doi: 10.1190/1.1439339.

Avseth, P., 2015, Explorational rock physics: The link between geological processes and geophysical observables: *Petroleum Geoscience*, 455-488.

Avseth, P., J. Dvorkin, G. Mavko, and J. Rykkje, 2000, Rock physics diagnostic of North Sea sands: Link between microstructure and seismic properties: *Geophysical Research Letters*, 27(17), 2761-2764.

Avseth, P., T. Mukerji, G. Mavko, and J. Dvorkin, 2010, Rock-physics diagnostics of depositional texture, diagenetic alterations, and reservoir heterogeneity in high-porosity siliciclastic sediments and rocks—A review of selected models and suggested work flows: *Geophysics*, 75(5), 75A31-75A47.

Basir, H. M., A, Javaherian. and M.T Yaraki., 2013, Multi-attribute ant tracking and neural network for fault detection: A case study of an Iranian oilfield: *Journal of Geophysics and Engineering*, 10, no.1, 015009. http://dx.doi.org/10.1088/1742-2132/10/1/015009

Berg, R. R., 1979, Characteristics of lower Wilcox reservoirs, Valentine and South Hallettsville Fields, Lavaca County, Texas: *Gulf Coast Association of Geological Societies Transactions*, 29, 11-23.

Bjørlykke, K., and J. Jahren, 2010, Sandstones and sandstone reservoirs: *Petroleum Geoscience*, 113-140.

Bjørlykke, K., M. Ramm, and G.C. Saigal, 1989, Sandstone diagenesis and porosity modification during basin evolution: *Geologische Rundschau*, 78(1), 243-268.

Castagna J.P., H.W. Swan, and D.J. Foster, 1998, Framework for AVO gradient and intercept interpretation: *Geophysics*, 63(3), 948-956.

Castagna, J.P., and H.W. Swan, 1997, Principles of AVO crossplotting: *The Leading Edge*, 16, no.04, 337-342

Castagna, J.P., M.L. Batzle, and R.L. Eastwood, 1985, Relationship between compressional and shear-wave velocities in clastic silicate rocks: *Geophysics*, 50, 551-570

Chuber, S., 1979, Exploration methods of discovery and development of lower Wilcox reservoirs in Valentine and Manking fields, Lavaca County, Texas: *Gulf Coast Association of Geological Societies Transactions*, 29, 42-51

Chuber, S., and R.L. Begeman, 1982, Productive lower Wilcox stratigraphic traps from an entrenched valley in Kinkler field, Lavaca County, Texas: *Gulf Coast Association of Geological Societies Transactions*, 32, 255-261

Debout, D.G., B.R. Weise, A.R. Gregory, and M.B. Edwards, 1982, Wilcox sandstone reservoirs in the deep subsurface along the Texas Gulf Coast: Their potential for production of geopressured geothermal energy: *Report of Investigations* No. 117 (No. DOE/ET/28461-T2), Texas Univ., Austin (USA), Bureau of Economic Geology, doi: 10.2172/6140725.

Devine, P.E., and D.M. Wheeler, 1989, Correlation, interpretation, and exploration potential of lower Wilcox valley-fill sequences, Colorado and Lavaca Counties, Texas: *Gulf Coast Association of Geological Societies Transactions*, 39, 57-74.

Dvorkin, J., A. Nur, and H. Yin, 1994, Effective properties of cemented granular materials: *Mechanics of materials*, 18(4), 351-366.

Dvorkin, J., and A. Nur, 1996, Elasticity of high-porosity sandstones: Theory for two North Sea data sets: *Geophysics*, 61(5), 1363-1370.

Egedahl, K., G.L. Kinsland, and D. Han, 2012, Seismic facies study of 3D seismic data, northern Louisiana, Wilcox Formation: *Gulf Coast Association of Geological Societies Transactions*, 62, 73-91.

Enomoto, C.B., 2014, Well log and 2D seismic data character of the Wilcox Group in South-Central Louisiana: *Gulf Coast Association of Geological Societies Transactions*, 64, 105-118.

Fatti, J.L., G.C. Smith, P.J. Vail, P.J. Strauss, and P.R. Levitt, 1994, Detection of gas in sandstone reservoirs using AVO analysis: A 3-D seismic case history using the Geostack technique: *Geophysics*, 59(9), 1362-1376, doi: 10.1190/1.1443695.

Fisher, W.L., and J.H. McGowen, 1967, Depositional systems in the Wilcox Group of Texas and their relationship to occurrence of oil and gas (1): *Gulf Coast Association of Geological Societies Transactions*, 17, 105-125.

Fisher, W.L., and J.H. McGowen, 1969, Depositional systems in Wilcox Group (Eocene) of Texas and their relation to occurrence of oil and gas: *AAPG Bulletin*, 53(1), 30-54.

Fohrmann, M., E. Reid, M.G. Hill, P.R. King, H. Zhu., K.J. Bland, D.P. Strogen, L. Roncaglia and G.P.L. Scott, 2012, Seismic reflection character, mapping and tectono-stratigraphic history of the Kupe area (4D Taranaki Project), south-eastern Taranaki Basin.: *GNS Science report* 2012/36 62 p.

Galloway, W.E., and T.A. Mcgilvery, 1995, Facies of a submarine canyon fill reservoir complex, lower Wilcox Group (Paleocene), central Texas coastal plain: *Turbidites and Associated Deep-Water Facies*, 20, 1-23.

Galloway, W.E., P.E. Ganey-Curry, X. Li, and R.T. Buffler, 2000, Cenozoic depositional history of the Gulf of Mexico basin: *AAPG Bulletin*, 84(11), 1743-1774, doi: 10.1306/8626C37F-173B-11D7-8645000102C1865D.

Galloway, W.E., T.L. Whiteaker, and P. Ganey-Curry, 2011, History of Cenozoic North American drainage basin evolution, sediment yield, and accumulation in the Gulf of Mexico basin: *Geosphere*, 7(4), 938-973, doi: 10.1130/GES00647.1.

Galloway, W.E., W.F. Dingus, and R.E. Paige, 1991, Seismic and depositional facies of Paleocene-Eocene Wilcox Group submarine canyon fills, northwest Gulf Coast, USA: *Seismic Facies and Sedimentary Processes of Submarine Fans and Turbidite Systems*, 247-271, Springer, New York, NY.

Greenberg, M.L., and J.P. Castagna, 1992, Shear-wave velocity estimation in porous rocks: Theoretical formulation, preliminary verification and applications: *Geophysical Prospecting*, 40, no.2, 195-210.

Hampson, D.P., B.H. Russell, and B. Bankhead, 2005, Simultaneous inversion of pre-stack seismic data: *SEG Technical Program Expanded Abstracts*, 1633-1637, doi: 10.1190/1.2148008.

Han, D.H., A. Nur, and D. Morgan, 1986, Effects of porosity and clay content on wave velocities in sandstones: *Geophysics*, 51(11), 2093-2107, doi: 10.1190/1.1442062.

Haq, B.U., J.Hardenbol, and P. R. Vail, 1987, Chronology of fluctuating sea levels since the Triassic (250 million years ago to present), Huston, Exxon Production Research Company, 24p

Hargis, R.N., 1986, Proposed stratigraphic classification of the Wilcox of South Texas: *Contributions to the Geology of South Texas*, 135-159.

Hargis, R.N., 2009, Major transgressive shales of the Wilcox, northern portion of south Texas: *South Texas Geological Society Bulletin*, 49(8), 19-47.

Hemmings-Sykes, S., 2012, The influence of faulting on hydrocarbon migration in the Kupe area, south Taranaki Basin, New Zealand: *M.S. thesis*, Victoria University of Wellington.

Henery. F., T. Trimbitasu and J. Johnson, 2011, An integrated workflow for reservoir sweet spot identification: *2011 Gussow Geoscience Conference*, Banff, Alberta.

Higgs, K. E., M. J. Arnot, G. H. Browne, and E. M. Kennedy, 2010, Reservoir potential of Late Cretaceous terrestrial to shallow marine sandstones, Taranaki Basin: *New Zealand, Marine and petroleum geology*, 27(9), 1849-1871.

Jansen, K., 2005, Seismic investigation of wrench faulting and fracturing at Rulison Field, Colorado: *Doctoral dissertation*, Colorado School of Mines.

King, P. R., G. P. Thrasher, K. J. Bland, P. Carthew, D. D'Cruz, A. G. Griffin, C. M. Jones, and D. P. Strogen (2010), Cretaceous-Cenozoic geology and petroleum systems of the Taranaki Basin, New Zealand. Digitally remastered version. GNS Science, Lower Hutt, *Institute of Geological & Nuclear Sciences monograph*, 13.

Krief, M., J. Garat, J. Stellingwerff, and J. Ventre, 1990, A petrophysical interpretation using the velocities of P and S waves (full-waveform sonic): *The Log Analyst*, 31(06).

Lu J., Z. Yang, Y. Wang, and Y. Shi, 2015, Joint PP and PS AVA seismic inversion using exact Zoeppritz equations: *Geophysics*, 80, no.5, 239-250, doi:10.1190/GEO2014-0490.1.

Mackey, G.N., B.K. Horton, and K.L. Milliken, 2012, Provenance of the Paleocene–Eocene Wilcox Group, western Gulf of Mexico basin: Evidence for integrated drainage of the southern Laramide Rocky Mountains and Cordilleran arc: *GSA Bulletin*, 124(5-6), 1007-1024, doi: 10.1130/B30458.1.

McDonnell, A., R.G. Loucks, and W.E. Galloway, 2008, Paleocene to Eocene deep-water slope canyons, western Gulf of Mexico: Further insights for the provenance of deep-water offshore Wilcox Group plays: *AAPG Bulletin*, 92(9), 1169-1189, doi: 10.1306/05150808014.

Mondol, N.H., K. Bjørlykke, and J. Jahren, 2008, Experimental compaction of clays: Relationship between permeability and petrophysical properties in mudstones: Petroleum Geoscience, 14(4), 319-337. Ødegaard, E.R.I.K. and P. Avseth, 2003, Interpretation of elastic inversion results using rock physics templates: *65th EAGE Conference & Exhibition*.

Odegaard E., and P. Aveseth, 2003, Interpretation of Elastic Inversion Results Using Rock Physics Templates: *65th EAGE Conference & Exhibition*.

Olariu, M.I., and H. Zeng, 2017, Prograding muddy shelves in the Paleogene Wilcox deltas, south Texas Gulf Coast: *Marine and Petroleum Geology*, 91, 71-88, doi: 10.1016/j.marpetgeo.2017.12.027.

Olariu, M.I., and W.A. Ambrose, 2016, Process regime variability across growth faults in the Paleogene Lower Wilcox Guadalupe Delta, South Texas Gulf Coast: *Sedimentary Geology*, 341, 27-49, doi: 10.1016/j.sedgeo.2016.05.013.

Pindell, J.L., 1994, Evolution of the Gulf of Mexico and the Caribbean, Caribbean geology: *an introduction*, 13-39.

Randen, T., E. Monsen, C. Signer, A. Abrahamsen, J.O. Hansen, T. Sæter and J. Schlaf, 2000, Threedimensional texture attributes for seismic data analysis: *70th SEG Technical Program Expanded Abstracts*, 668-671. http://dx.doi.org/10.1190/1.1816155

Randen, T., E. Monsen, C. Signer, A. Abrahamsen, J.O. Hansen, T. Sæter and J. Schlaf, 2000, Threedimensional texture attributes for seismic data analysis: *70th SEG Technical Program Expanded Abstracts*, 668-671. http://dx.doi.org/10.1190/1.1816155

Roncaglia, L., 2006, Stratigraphy, well correlation and seismic-to-well tie in the Upper Cretaceous to Pliocene interval in the Kupe region, Taranaki Basin, New Zealand, Introduction to the stratigraphic database in PETREL, Vol. 2008: *GNS Science*.

Ross, C.P., and D.L. Kinman, 1995, Non-bright-spot AVO: Two examples: *Geophysics*, 60, 1398-1408

Russell, B., and D. Hampson, 2006, The old and the new in seismic inversion: *CSEG Recorder*, 31(10), 5-11.

Rutherford, S.R., and R.H. Williams, 1989, Amplitude-versus-offset variation in gas sands: *Geophysics*, 54, 680-688

Schenewerk, P., D. Goddard, and J. Echols, 1994, Reservoir characterization and preliminary modeling of deltaic facies, lower Wilcox, Concordia Parish, Louisiana: *Gulf Coast Association of Geological Societies Transactions*, 44, 663-674.

Sharman, G.R., J.A. Covault, D.F. Stockli, A.F.J. Wroblewski, and M.A. Bush, 2017, Early Cenozoic drainage reorganization of the United States Western Interior–Gulf of Mexico sediment routing system: *Geology*, 45(2), 187-190.

Stagpoole, V. and A. Nicol, 2008, Regional structure and kinematic history of a large subduction back thrust, Taranaki Fault, New Zealand: *Journal of Geophysical Research: Solid Earth*, 113, B1. http://dx.doi.org/10.1029/2007JB00517

Wagner, C., A. Gonzalez, V. Agarwal, A. Koesoemadinata, D. Ng, S. Trares, N. Biles, and K. Fisher, 2012, Quantitative application of poststack acoustic impedance inversion to subsalt reservoir development: *The Leading Edge*, 31(5), 528-537, doi: 10.1190/tle31050528.1.

Warwick, P.D., 2017, Geologic assessment of undiscovered conventional oil and gas resources in the lower Paleogene Midway and Wilcox groups, and the Carrizo sand of the Claiborne group, of the northern Gulf Coast region: *U.S. Geological Survey Open-File Report* 2017-1111, 67p.

Wiggins, R., G.G. Kenny, and C.D. McClure, 1983, A method for determining and displaying the shear-velocity reflectivities of a geologic formation, *European patent Application*, 0113944.

Winker, C.D., 1982, Cenozoic shelf margins, Northwestern Gulf of Mexico: *Gulf Coast Association of Geological Societies Transactions*, 32, 427-448.

Zeng, H., W.A. Ambrose, and W. Xu, 2016, Sediment dispersal patterns of the outer shelf to upper slope Paleocene-Eocene Wilcox Group, South-Central Texas coast: *Gulf Coast Association of Geological Societies Transactions*, 5, 215-237.

Zhang, B., D. Chang, T. Lin, and K.J. Marfurt, 2014, Improving the quality of prestack inversion by prestack data conditioning: *Interpretation*, 3(1), T5-T12, doi: 10.1190/INT-2014-0124.1.

Zoeppritz, K., 1919, On the reflection and propagation of seismic waves, *Gottinger Nachrichten*, 66-84.

VITA

Tianze Zhang was born in Heilongjiang, China. In 2014, he received his B.E in Resources Prospecting Engineering from China University of Geosciences, Beijing. He was an intern at the Oil Production Company in Daqing for two months, and did research in Petroleum Geology at Northeast Petroleum University for three month after he graduated. He joined Missouri University of Science and Technology to continue his academic career. In December 2019, he received his PhD in Geology and Geophysics from Missouri University of Science & Technology.

His research interests involved multiple areas. His first research was the mantle motion analysis using shear wave splitting in Caribbean Plate. Then he did research of the Desert Eye structure formation mechanism analysis with seismic refraction survey. He then focused on the exploration geophysics that using rock physics and seismic inversion to characterize the reservoir. Because of his research expertise, he joined the competition group for AAPG-IBA Competition in 2017 as the seismic interpreter, and gained praise for his excellent contribution to the group. He was a member of the Society of Exploration Geophysicists (SEG). He also served as student representative and secretary of the SEG student chapter of Missouri S&T. He published conference and journal papers, one of the conference paper submitted to the 2017 SEG Annual Meeting listed as top of 39 papers presented at the Houston meeting.